Patient-Specific Computational Modeling of Cardiac Mechanics

Henrik Finsberg

December 20, 2017

Thesis submitted for the degree of Philosophiæ Doctor

© Henrik Finsberg, 2017

Series of dissertations submitted to the
Faculty of Mathematics and Natural Sciences, University of Oslo
No. 1938

ISSN 1501-7710

All rights reserved. No part of this publication may be
reproduced or transmitted, in any form or by any means, without permission.

Cover: Hanne Baadsgaard Utigard.
Print production: Reprosentralen, University of Oslo.

Acknowledgements

This is my thesis submitted for the degree Doctor Scientiarum, submitted to the Department of Informatics, University of Oslo. The work conducted in this thesis took place in the period from October 2014 to September 2017.

First of all, I wish to deeply acknowledge the Center for Cardiological Innovation (CCI) for providing the financial support for my PhD.

I would especially like thank my main supervisors Joakim and Sam, which both have been excellent in providing useful feedback, and directions for my thesis. Joakim, thank you for allways taking time to answer any question I may have, whether it is related to work or private. Sam, thank you for setting up all the collaborations and for guiding my work in the right direction.

I would also like to thank Simula Research Laboratory for providing an outstanding working environment. In my opinion, the including management and the nice people at Simula, makes Simula the perfect place to pursue a PhD. A special thank to the people from the Cardiac Modeling group, in particular to Siri which I shared office with for most of my PhD, and to Gabriel who I worked very close with during my first year.

I am also grateful to the CCI for giving me the opportunity to work with, and learn from such exceptional medical researchers and for providing an environment for interdisciplinary collaborations. In particular I would like to thank, Hans Henrik, John and Espen for many interesting and fruitful discussions.

Finally, I would like to thank my family for always reminding me what truly matters in life. Elisabeth, I am deeply grateful for all the support you have given me during these years.

Henrik Nicolay Topnes Finsberg
Oslo, September, 2017

List of papers

Paper 1
Gabriel Balban, Henrik Finsberg, Hans Henrik Odland, Marie E. Rognes, Stian Ross, Joakim Sundnes, and Samuel Wall. *High-resolution data assimilation of cardiac mechanics applied to a dyssynchronous ventricle.* International journal for numerical methods in biomedical engineering (2017). doi:10.1002/cnm.2863
Status: published

Paper 2
Henrik Finsberg, Gabriel Balaban, Stian Ross, Trine F. Håland, Hans Henrik Odland, Joakim Sundnes, and Samuel Wall. *Estimating cardiac contraction through high resolution data assimilation of a personalized mechanical model.* Journal of Computational Science (2017). doi:10.1016/j.jocs.2017.07.013
Status: published

Paper 3
Henrik Finsberg, Ce Xi, Ju Le Tan, Liang Zhong, Martin Genet, Joakim Sundnes, Lik Chuan Lee, and Samuel T. Wall. *Efficient estimation of personalized biventricular mechanical function employing gradient-based optimization.* International journal for numerical methods in biomedical engineering
Status: submitted

Paper 4
Henrik Finsberg, John Aalen,Camilla K. Larsen, Espen Remme, Joakim Sundnes, Otto A. Smiseth, and Samuel T. Wall. *Assessment of regional myocardial work from a patient-specific cardiac mechanics model.*
Status: to be submitted

Contents

1 Introduction 1

1.1 Aim of thesis . . . 1
1.2 Cardiac Anatomy and Physiology . . . 5
  1.2.1 Myocardial structure and morphology . . . 5
  1.2.2 The cardiac cycle . . . 6
  1.2.3 Ventricular pumping function . . . 7
  1.2.4 Cardiac Pathophysiology . . . 10
  1.2.5 Summary of Cardiac Physiology . . . 11
1.3 Mechanical modeling . . . 12
  1.3.1 Kinematics . . . 12
  1.3.2 Balance laws and transformations . . . 13
  1.3.3 Hyperelasticity . . . 15
  1.3.4 Incompressibility . . . 18
  1.3.5 Boundary Conditions . . . 19
  1.3.6 Force-balance equation . . . 21
  1.3.7 Constitutive relations . . . 24
  1.3.8 Implementation details . . . 29
1.4 Personalization of Cardiac Biomechanics . . . 32
  1.4.1 Medical Imaging . . . 32
  1.4.2 Geometry and microstructure . . . 33
  1.4.3 Choosing the reference geometry . . . 38
  1.4.4 Data Assimilation . . . 41
  1.4.5 PDE-constrained optimization . . . 45
  1.4.6 Identifiability of parameters . . . 48
  1.4.7 Extraction of biomarkers . . . 49
1.5 Summary of papers . . . 51

1.5.1 Paper 1: High-resolution data assimilation of cardiac mechanics applied to a dyssynchronous ventricle 51
1.5.2 Paper 2: Estimating cardiac contraction through high resolution data assimilation of a personalized mechanical model 52
1.5.3 Paper 3: Efficient estimation of personalized biventricular mechanical function employing gradient-based optimizatio 53
1.5.4 Paper 4: Assessment of regional myocardial work from a patient-specific cardiac mechanics model 54
1.6 Other contributions 57
1.6.1 Talks 57
1.6.2 Posters 57
1.6.3 Software 58
1.7 Closing remarks and future directions 59

2 Paper 1 69
2.1 Introduction 71
2.2 Materials and Methods 73
2.2.1 Wall motion modelling 73
2.2.2 Clinical measurements 75
2.2.3 Ventricular geometry generation 76
2.2.4 Parameter Estimation 77
2.2.5 Definition of functionals 79
2.2.6 Parameter estimation as an optimization problem 81
2.2.7 Implementation of mechanics and optimization solvers . . 82
2.2.8 Error Estimation 84
2.3 Numerical Experiments 85
2.3.1 Estimation of elastic parameter a 86
2.3.2 Synthetic dataset creation 86
2.3.3 Choice of functional weights α and λ 86
2.3.4 Contraction estimation with synthetic data 87
2.3.5 Contraction estimation with in-vivo data 89
2.3.6 Effect of contraction parameter resolution 89
2.4 Discussion 94
2.4.1 Limitations 97
2.5 Conclusion and Future Outlook 98
2.6 Author Declaration 99
2.7 Appendix 99

2.7.1 Sensitivity of elastic a parameter to error in atrial systolic volume measurements . . . 99
2.7.2 Sensitivity of estimated parameters to spring constant k. . . 99
2.7.3 Effect of mesh resolution on estimated contraction γ at P1 resolution . . . 101
2.7.4 Sensitivity of Contraction Size to choices of α and λ . . . 101
2.7.5 Estimation of noise in echo speckle tracking strain measurements . . . 102

3 Paper 2 111
3.1 Introduction . . . 113
3.2 Materials and methods . . . 113
3.2.1 Data acquisition . . . 113
3.2.2 Automated geometry and microstructure creation . . . 114
3.2.3 Mechanical Model . . . 114
3.2.4 Data Assimilation . . . 115
3.2.5 Implementation details . . . 117
3.2.6 Contraction analysis . . . 117
3.3 Results and discussion . . . 118
3.3.1 Matching of strain and volume . . . 118
3.3.2 Estimation of global contractility and elastance . . . 119
3.4 Discussion . . . 120
3.5 Conclusions . . . 121

4 Paper 3 127
4.1 Introduction . . . 129
4.2 Methods . . . 130
4.2.1 Data acquisition and pre-processing . . . 130
4.2.2 Mechanical modeling . . . 132
4.2.3 PDE-constrained optimization . . . 135
4.2.4 Parameter estimation . . . 136
4.2.5 Mechanical Analysis . . . 139
4.2.6 Implementation details . . . 139
4.3 Results . . . 140
4.3.1 Data assimilation, validation and solver performance . . . 140
4.3.2 Mechanical analysis . . . 143
4.4 Discussion . . . 147

4.4.1 Data compatibility and multi-objective optimization . . . 148
4.4.2 Fiber angle sensitivity 148
4.4.3 Fiber stress 149
4.4.4 Contractility 150
4.4.5 Elastance 150
4.4.6 Limitations and future directions 151
4.5 Conclusion 152
4.6 Appendix 153
4.6.1 Sensitivity to unloaded configuration 153

5 Paper 4 163
5.1 Introduction 165
5.2 Methods 167
5.2.1 Mechanical modeling 167
5.2.2 Calculation of work 169
5.2.3 Pre-processing of in vivo data sets 171
5.2.4 Data assimilation and parameter estimation 172
5.3 Results 174
5.3.1 Data assimilation 174
5.3.2 Estimation of regional myocardial work 174
5.4 Discussion 179
5.4.1 Pressure-strain versus fiber stress-strain 179
5.4.2 Limitations 181
5.5 Conclusion 182
5.6 Appendix 184
5.6.1 Joint estimation of unloaded configuration and passive material parameters 184

Introduction

Aim of thesis

Cardiovascular diseases are the leading cause of death in the world, responsible for more than 17.3 million deaths annually, a number that is expected to reach 23.6 million by 2030 [82]. Advancements in detection and treatment have reduced morbidity and mortality, but knowledge of the underlying mechanisms for the development of the disease, is still very poor. Consequently, while some patients respond very well to a therapy, others suffering from the same symptoms might not respond at all. Our understanding of these mechanisms has improved through development of advance imaging techniques and through computational modeling. While imaging plays a central role in assessment of cardiac structure and kinematics, biophysical models can help us to understand causality in this multiscale environment.

One of the earliest examples of modelling applied to cardiac physiology dates back to 1892 when Robert Wood approximated the ventricle as a thinned-wall spherical shell [81], and formulated the well known *Law of Laplace*. Since 1892 more realistic and sophisticated models have been developed in order to better describe the anatomical as well as the biophysical nature of the ventricle. The first extension came in 1927 to thick-walled spheres [53]. In the 1960s the spheres were substituted by ellipsoids, with thin-walled models in 1963 [70], and with thick-walled models in 1968 [80]. A thorough comparison of the different early models is presented in [37]. The first reported usage of image-based geometries dates back to 1972 [28], were X-ray was used to image the left ventricle and the finite element method was used to estimate wall stress. The relatively poor computational power, together with the low image quality really challenged the biomedical bioengineers at that time. The following phrase, taken form [33] illustrates this fact: *"Programming for the solution of the large number of simultaneous linear equations generated by the finite element method on computers with* *capacity not exceeding 32K words of memory required special attention to very compact storage of the stiffness matrix and the retrieval of its coefficients"*.

A paradigm shift in the field of cardiac mechanics modeling came in the late 1980s at the University of Auckland. Here the first models based on a continuum description of the heart were developed [39], which are still used today.

Today, advanced imaging techniques allow us to acquire detailed mechanical information about the heart of an individual. In addition, advanced numerical algorithms combined with high performance computing power enable us to get more and more detailed simulation of a patients heart.

The need for building adequate patient-specific models that captures the geometrical information observed in the images, as well as the underlying biophysical processes, is recognized as one of the key challenges in modern bioengineering [38]. This is also reflected in the exponential increase in the yearly number of publications on the topic [68]. In the future, models could be used to as a diagnostic tool to extract features of a patient's heart that are otherwise impossible to extract from images. Eventually, models could potentially predict the outcome of different treatment strategies and guide clinicians in the decision making.

In other parts of physical sciences and engineering, such as the space industry or meteorology, the role of the computational science has been crucial for its development. Without the increasing computational power predicted by Moore's law [10] and better numerical methods, such as the finite element method, scientist would not have been able to predict complex physical phenomena such as a Tsunami, or being able to send humans out in space.

Despite our ability to simulate complex physical systems such as the weather, we still have a way to go before we are able to simulate a human organ, such as the heart, with the same precision. The multiscale nature of biophysical processes has challenged engineers for decades. Even though we understand processes at each level, such as the flow of ions in and out of the cell, or the electrical transduction through the heart, the question of how to couple these levels together is still open [59].

Another question is how to fuse data observed in medical images with computational models, in order to make models specific to the individual. These questions have to be addressed before we can take the next step into personalized simulations for *in silico* medicine, and use computer simulations to guide treatment, and predict outcome.

Some of these unanswered questions serve as motivation for the work conducted in this thesis. We focus purely on the mechanical modeling of the heart and the aim has been to develop a framework for building mechanical models that are personalized at the level of the individual.

The mechanics of the heart can be described via equations of nonlinear elasticity which are traditionally formulated using a continuum mechanics approach. This approach has been extensively used in other parts of engineering, and in this work the numerical solutions to these partial differential equations (PDE) are solved using the finite element method (FEM) with the open source software package FEniCS [50].

These mechanical models contain model parameters which may vary from individual to individual, and patient specificity can be obtained by fitting these model parameters to additional clinical data. This process is often referred to as data assimilation, a field that has its root in meteorology where one wants to make a weather forecast based on observations from strategically placed weather stations. The idea is to construct a functional which represent the mismatch between the model and the observations, and by changing the model parameters we also change the value of this mismatch functional. Now, what we want to do is to minimize this functional using these model parameters as controls. At the same time, the governing PDE, which depend upon these model parameters, has to remain true. We therefore often refer to such problems as PDE-constrained optimization problems. Solving such problems is challenging because evaluation of the mismatch functional requires the solution of a nonlinear PDE, which is computationally expensive, and we therefore want to keep the number of functional evaluations at a minimum. A good way of doing this is traverse the parameter space along the gradient descent, which is guaranteed to bring us towards a local minimum. However, this requires calculation of the functional gradient, or the derivative of the mismatch functional with respect to the model parameters. As we will see, the functional gradient can be computed efficiently by considering the adjoint equation, and recent development in numerical software tools [22] allow us to exploit this also numerically.

The developed framework in this thesis could be applied directly to estimate high dimensional model parameters without any manual tuning of parameters. The aim has been to develop a framework for automatic generation of patient-specific simulations of the heart, by fitting model-parameters to potentially “any” type of clinical data. In particular, incorporating regional motion data to estimate spatially resolved parameters has been an essential contribution in this thesis. This type of automated simulation pipeline could potentially be integrated as a part of a clinical diagnostic toolbox and be used to guide clinicians in the decision-making and treatment planning. In particular, such models can be used to assess information that is difficult or even impossible to measure in the human heart, such as indices of contractility, myocardial work and myofiber stress. While the first part of the thesis (Paper 1) is concerned with developing a framework for constraining a mechanics model to clinical data, the second part (Paper 2, 3 and 4) evaluates potentially useful biomarkers extracted from the personalized mechanics model. Future work should be geared towards validation of such models, in order to unleash its potential in the clinic.

The remaining introduction in this thesis is organized as follows. In Section 1.2 we briefly explain some concepts in cardiac anatomy and physiology which are used throughout the thesis. This section ends with a description of the different cardiac diseases encountered in this thesis. In Section 1.3 we give an introduction to continuum mechanics and mechanical modeling of the heart. The basic equations of elasticity as well as the constitutive relations for the cardiac tissue, and some numerical considerations are covered. In Section 1.4 we explain how to personalize a mechanical model using clinical data. We start by explaining the different imaging modalities used in this thesis, and how finite element meshes are created from images. We also explain how to find a more realistic reference geometry than the one obtained from medical images. At the end we introduce data assimilation, and how to compute the functional gradient using the adjoint method. Finally in Section 1.5 we summarize the research papers that make up this thesis, and make some closing remarks and suggestions for future directions.

Cardiac Anatomy and Physiology

In this section we will give a very short introduction to cardiac physiology, and explain some of the basic terms used in this thesis. The reader is referred to the book of Arnold M. Katz for more details [42].

Myocardial structure and morphology

The heart is the muscular organ responsible for circulating blood throughout the body. Figure 1.1 shows a schematic representation of the heart.

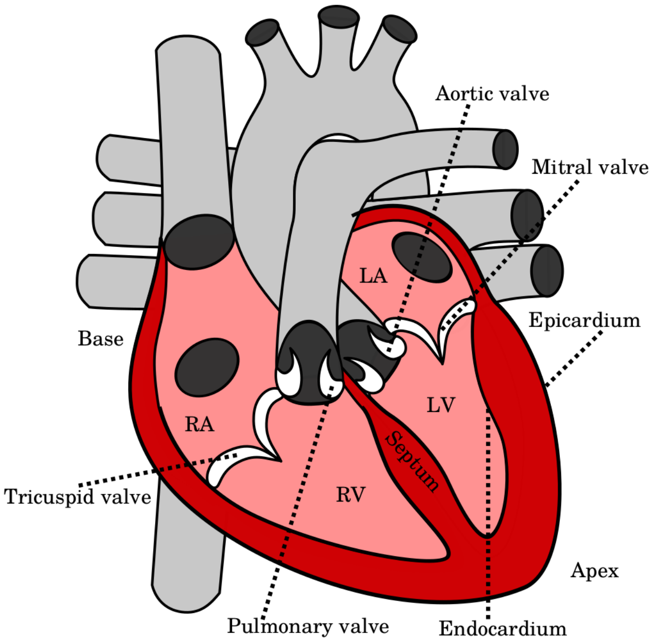

Figure 1.1: Schematic representation of the heart's anatomy. (Adapted and modified from Wapcaplet in Sodipodi).

Deoxgenated blood is transported from the body through the veins and to the right atrium (RA). From the RA, blood flows to the right ventricle (RV), before it is sent through the the pulmonary arteries(PA) and to the lungs, where the bloods gets oxygenated. From the lungs, the blood travels through the pulmonary veins to the left atrium (LA), and finally to the left ventricle (LV), before is is sent out to the body again through the aorta.

The heart itself is located approximately in the center of the chest with the *apex* of heart angled down towards the left of the body, and the *base* located just behind the breastbone.

Starting from the outside of the heart we have the *pericardium*, the *epicardium*, the *myocardium* and the *endocardium*. The pericardium is a fibroserous sac that surrounds that heart, and the endo- and epicardium are respectively the inner and outer layers of the myocardium. The myocardium is made up by individual muscle cells, or myocytes, which branch and join neighboring cells, and form a complicated fibrous network which is often referred to as a *functional syncytium* (meaning that the number of active muscle fibers cannot be varied from beat to beat).

The ventricular muscle fibers orientations varies smoothly through the wall, and rotates from the endocardium to the epicardium forming a helical structure [72]. These muscle fiber are further organized in laminar sheets, which is separated by gaps called cleavage planes [47].

Each myocyte is composed of bundles of myofibriles, which again contains *myofilaments*. The myofilaments consist of a repeated pattern of lines and bands which can be seen as a collection of individual contractile units called *sarcomeres*. A simple sketch of a sarcomere is shown in Figure 1.2.

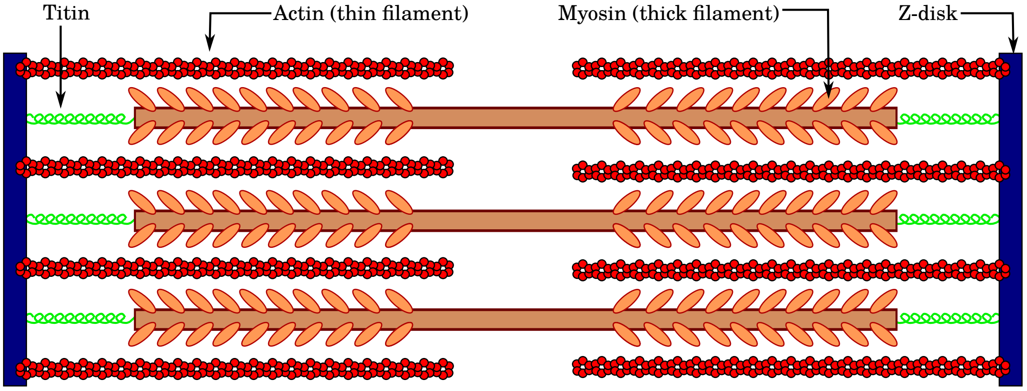

Figure 1.2: Illustration of the sarcomere structure.

The sarcomeres are composed of thick and thin filaments that slides back and forth when the muscle contracts or relaxes. The thin filaments are made up by a protein called *actin* while the thick filaments are made up by a protein called *myosin*.

The cardiac cycle

The heart beats in a cyclic manner, about one beat every second. The contraction of the heart is triggered by an action potential originating from specialized cells in the right atrium. When an action potential is triggered, calcium is released into the cells. These calcium ions binds to a complex called troponin C located at the thin filaments, which then exposes the actin to the myosin head. When myosin binds to actin we say that a *cross-bridge* is formed between the thin and thick filaments. A *power stroke* is triggered after ATP hydrolysis, and the sarcomere shortens. The signal propagates through the myocardium and along specialized electrical highways with high conducting cells.

One way to describe the cardiac cycle is by means of the pressure and volume inside the individual chambers. For example, plotting the left ventricular (LV) volume on the $x-$axis and the LV pressure on the $y-$axis provides an intuitive representation of the cardiac cycle known as the *PV-loop*. In Figure 1.3 we show an illustration of a typical PV-loop. At end-diastole (ED), the mitral valve closes, and the ventricle contracts against a rising pressure. During this phase, no blood goes in or out of the ventricle and we call it the *isovolumic contraction* phase. When the ventricular pressure exceeds the aortic pressure, the aortic valve opens and the heart *ejects* blood into the body. When the ventricular pressure drops below the aortic pressure, the aortic valve closes and pressure drops as the ventricle relaxes, and we enter the *isovolumic relaxation* phase. The phase when the ventricle contracts, from end diastole until the end of ejection is called *systole*, hence this point in the cycle is also know as end-systole (ES). Similarly, the phase for which the ventricle relaxes from the beginning isovolumic relaxation to end diastole, is called *diastole*. When the pressure drops below the atrial pressure the mitral valve opens and blood is sucked into the ventricle. In the final stage of the filling of the ventricle, the atria contracts and fills the ventricle before we arrive at end-diastole, and the cycle repeats.

Ventricular pumping function

The pressure and volume inside the ventricle can provide us with information about the passive and active properties of the myocardium. Imagine it was possible to shut down all contractile units in the myocardium, and remove all loads (e.g set the pressure to zero). This would be analogous to have a deflated balloon. In order to get some information about the stiffness of the myocardium one could try to inflate the ventricle. The stiffer the myocardium is, the higher pressure would be needed in order to increase the volume. This relationship between the pressure and volume during the inactive state is called the end diastolic pressure volume relationship (*EDPVR*).

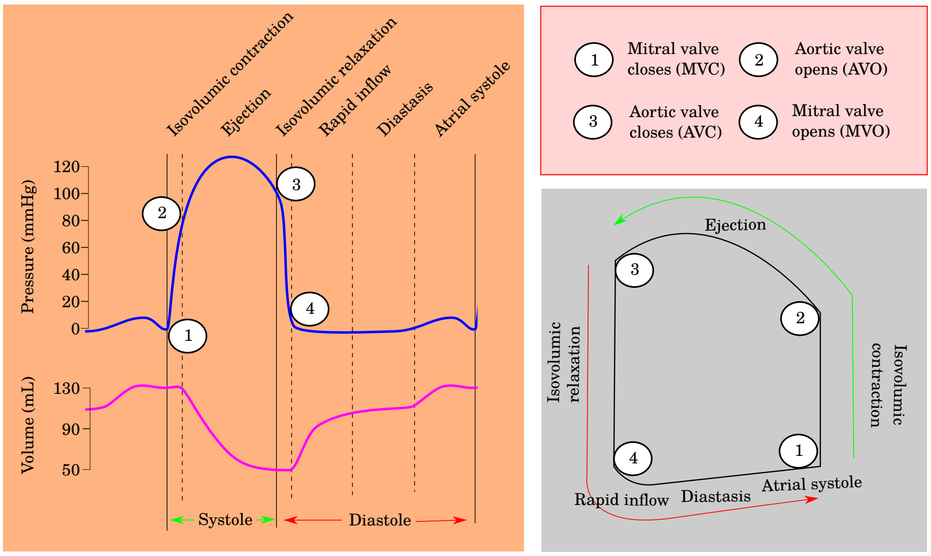
Isovolumic contraction
Ejection
Isovolumic relaxation
Rapid inflow
Diastasis
Atrial systole
Pressure (mmHg)
120
100
80
60
40
20
0
Volume (mL)
130
90
50
1
2
3
4
Systole
Diastole
① Mitral valve closes (MVC)
② Aortic valve opens (AVO)
③ Aortic valve closes (AVC)
④ Mitral valve opens (MVO)
Ejection
Isovolumic relaxation
Isovolumic contraction
Rapid inflow
Diastasis
Atrial systole

Figure 1.3: Showing the relation between pressure and volume in the left ventricle during the cardiac cycle. To the left we show a reduced version of the classical Wiggers diagram with pressure and volume plotted against time. To the right we show the pressure volume loop with volume plotted on the $x-$axis and pressure on the $y-$axis.

Similarly, imagine now that the ventricle is at the end-systolic state, when the muscle cells are contracting at their most forcefully. Changing the pressure at this state would also result in a change in volume and this relationship between pressure and volume is called the end systolic pressure volume relationship (*ESPVR*). The two pressure volume relationships are depicted in Figure 1.4.

Although single-beat estimation of these relationships do exist [71, 43], the EDPVR and ESPVR can be estimated by changing the loading condition. Changing the *preload*, i.e the load on the ventricle before it starts contracting would brings us along the EDPVR curve, while changing the *afterload*, i.e the load after the ventricle has contracted, would shift the end-systolic point along the ESPVR curve.

The ventricular pumping function depends on the loads that the ventricle experience. If the amount of blood returning from the veins into the heart increases, i.e increased preload, the end diastolic volume increases and the ventricle contracts more forcefully in order to synchronize the amount of ejected blood with the venous return. This fundamental law, is called the *Frank-Starling law*. The Frank-Starling law relates the EDPVR to the ESPVR, and states that the stroke

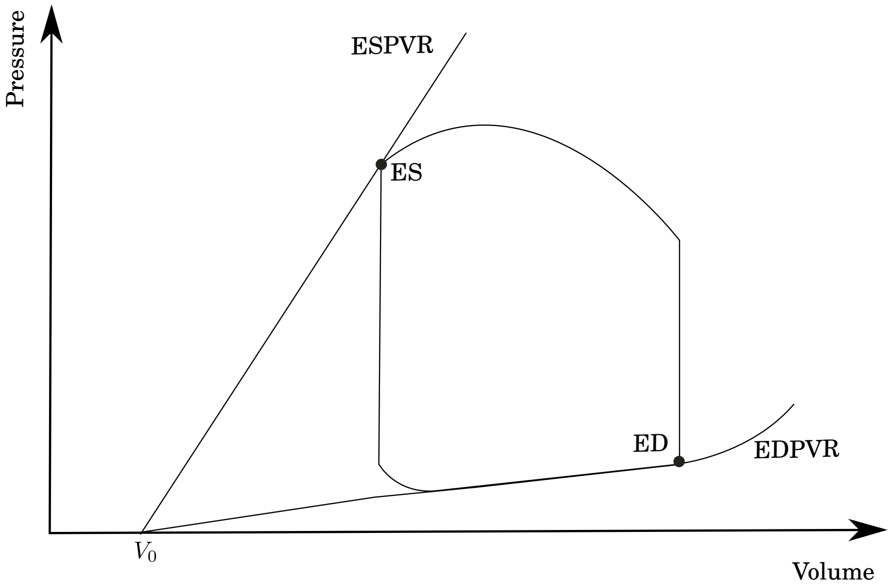

Figure 1.4: Illustration of the end diastolic pressure volume relationship (EDPVR) and the end systolic pressure volume relationship (ESPVR). The volume axis intercept V_0 from the time varying elastance model is also shown.

volume, i.e the difference in end systolic and end diastolic volume, increases in response to and increase in preload. This allows the cardiac output to be synchronized with the venous return and blood supply, without depending upon external regulation.

The slope of any pressure volume relationship is called the *elastance*, and a famous model known as the time varying elastance model, relates the cavity pressure in the ventricle to the volume and a time varying elastance $E(t)$ [69],

$$P(t) = E(t)(V(t) - V_0). \tag{1.1}$$

Here P is the endocardial pressure, V the cavity volume, E the time-varying elastance, and V_0 the volume axis intercept.

In fact, the end systolic elastance, $E(t)$ with t being time of end systole, is considered to be the gold standard in terms of quantifying myocardial *contractility*. However, it is rarely used because it is difficult to determine clinically. What should be noted is that end systolic elastance is independent of load, and therefore serves as measure of the ability of the ventricle to do work, i.e myocardial contractility.

Cardiac Pathophysiology

Pathophysiology is the study of the physiology of the diseased heart, and we will briefly mention some of the different cardiac diseases encountered in this thesis.

Heart failure

Heart failure (HF) is a common term for all heart diseases in which the heart is unable to supply the body with enough blood to meet its demand. It is common to separate between diastolic and systolic HF. Diastolic HF refers to the heart's inability to be passively filled, and thereby reduce the cardiac output according to the Frank-Starling law of the heart. In systolic HF on the other had, the heart's ability to contract efficiently is reduced.

Left bundle branch block

One type of heart failure can result from conduction block in the heart. An electrical wave travels through electrical highways of high conducting cells. One of these highways known as the Bundle of His splits into two parts, the right and left bundle. The right bundle activates the right ventricle, while the left bundle activates the left ventricle. For patients suffering from left bundle branch block, there is "road block" on the highway along the left bundle, meaning that the left ventricle is activated later than preferable, and the right ventricle is activated prior to the left ventricle. This can result in a dyssynchronous contraction, yielding a reduced pumping effect. A promising treatment for these patients is called Cardiac Resynchronization Therapy (CRT) [16].

Imagine a boat with rowers on both sides trying to get the boat moving forward. If the rowers don't synchronize their strokes, the boat will veer from side to side and have a much longer route – if it gets anywhere at all. To synchronize the rowers, we could add a coxswain who tells the rowers when to row. We can use the rower analogy to think of the contractions of the left and right side of the heart. With the heart, implanting a CRT device is like adding a coxswain to direct the rowers. The CRT's goal is to try to resynchronize the heart so that the left and right ventricles contract simultaneously. It involves pacing the heart on both the left and right ventricle so that the heart can contract in a synchronous way. Therefore CRT is often referred to as biventricular pacing, or just BiV pacing. However, experiments show that between 30-40% of the selected patients do not respond to CRT [18], which is why much research is put into increasing the responder rate.

Summary of Cardiac Physiology

The multiscale and multiphysics phenomena governing the mechanics of the heart is complex. How the molecular dynamics should be coupled to the electrophysiology at the cellular level, how the electrophysiology should be coupled to the mechanics at the organ level and what type of feedback mechanisms that should be included is far from fully understood. In this thesis we limit ourselves to the study of what is happening on the organ level, and concentrate purely on the mechanical aspect.

Mechanical modeling

In this section we will cover the necessary theory of continuum mechanics in order to model the mechanics of the heart. The theory of continuum mechanics is extensive, and we will not be able to cover everything. For a complete review of continuum mechanics the reader is therefore referred the textbook of Gerhard Holzapfel [35] from which most of the theory in this section is taken. For the even more mathematically oriented reader we refer to [54].

Kinematics

We represent the heart as a continuum body $\mathfrak{B}$ embedded in $\mathbb{R}^3$. A configuration of $\mathfrak{B}$ is a mapping $\chi : \mathfrak{B} \to \mathbb{R}^3$. We denote the *reference configuration* of the heart by $\Omega \equiv \chi_0(\mathfrak{B})$, and the *current configuration* by $\omega \equiv \chi(\mathfrak{B})$. The mapping $\varphi : \Omega \to \omega$, given by the composition $\varphi = \chi \circ \chi_0^{-1}$, is a smooth, orientation preserving (positive determinant) and invertible map. We denote the coordinates in the reference configuration by $\mathbf{X} \in \Omega$, and the coordinates in the current configuration by $\mathbf{x} \in \omega$. The coordinates $\mathbf{X}$ and $\mathbf{x}$ are commonly referred to as material and spatial points respectively, and are related through the mapping φ, by $\mathbf{x} = \varphi(\mathbf{X})$. For time-dependent problems it is common to make the time-dependence explicitly by writing $\mathbf{x} = \varphi(\mathbf{X}, t)$. In the following we will only focus on the mapping between two configurations and therefore no time-dependence is needed. The *deformation gradient* is a rank-2 tensor, defined as the partial derivative of φ with respect to the material coordinates:

$$\mathbf{F} = \nabla_{\mathbf{X}} \varphi = \mathrm{Grad}\mathbf{x}. \tag{1.2}$$

Here we also introduce the notation Grad, which means derivative with respect to reference coordinates. The deformation gradient maps vectors in the reference configuration to vectors in the current configuration, and belongs to the space of linear transformations from $\mathbb{R}^3$ to $\mathbb{R}^3$ with strictly positive determinant, which we denote by Lin^+. Another important quantity is the *displacement* field

$$\mathbf{u} = \mathbf{x} - \mathbf{X}, \tag{1.3}$$

which relates positions in the reference configuration to positions in the current configuration. From (1.2) we see that

$$\mathbf{F} = \mathrm{Grad}\mathbf{x} = \mathrm{Grad}\mathbf{u} + \mathrm{Grad}\mathbf{X} = \mathrm{Grad}\mathbf{u} + \mathbf{I}. \tag{1.4}$$

Some other useful quantities are the *right Cauchy-Green* deformation tensor $\mathbf{C} = \mathbf{F}^T\mathbf{F}$, the *left Cauchy-Green* deformation tensor $\mathbf{B} = \mathbf{F}\mathbf{F}^T$, the *Green-Lagrange* strain tensor $\mathbf{E} = \frac{1}{2}(\mathbf{C} - \mathbf{I})$, and the determinant of the deformation gradient $J = \det \mathbf{F}$.

An important concept in mechanics is the concept of stress, which is defined as force per area $\left[\frac{\mathrm{N}}{\mathrm{m}^2}\right]$. When working with different configurations one needs to be careful with which forces and which areas we are talking about. Table 1.1 shows how forces and areas are related for the most important stress tensors used in this thesis. Note that the explicit form of the stress tensor requires a constitutive law for the material at hand. This will be discussed in more detail in Section 1.3.7.

Stress tensor	Forces	Area
Second Piola-Kirchhoff (**S**)	Reference configuration	Reference configuration
First Piola-Kirchhoff (**P**)	Current configuration	Reference configuration
Cauchy (σ)	Current configuration	Current configuration

Table 1.1: Showing different stress tensors used in this thesis, and how they relate forces to areas trough different configurations.

Balance laws and transformations

In this section we will cover some basic transformations used to derive the fore-balance equations for the mechanics of the heart.

Transformations between reference and current configuration

By definition, the reference configuration Ω, and current configuration ω, are related via the deformation map φ in the sense that a point $\mathfrak{p} \in \mathfrak{B}$ with reference coordinates $\mathbf{X}$ and current coordinates $\mathbf{x}$ satisfies $\mathbf{x} = \varphi(\mathbf{X})$. Likewise a vector in the reference configuration is related to a vector in the current configuration via the deformation gradient $\mathbf{F}$; if $\mathrm{d}\mathbf{X}$ is a vector in the reference configuration it will transform to the vector $\mathrm{d}\mathbf{x}$ in the current configuration, and $\mathrm{d}\mathbf{x} = \mathbf{F}\mathrm{d}\mathbf{X}$. From this relation we also derive that the transformation of an infinitesimal volume element in the reference configuration, $\mathrm{d}V$ is related to an infinitesimal volume element in the current configuration, $\mathrm{d}v$ via the determinant of the deformation gradient,

$$\mathrm{d}v = \det(\mathbf{F})\mathrm{d}V. \tag{1.5}$$

Another important transformation is the transformation of normal vectors. By noting that we can write (1.5) using surface elements

$$\begin{aligned} \mathrm{d}s\mathbf{n}\mathrm{d}\mathbf{x} = \mathrm{d}v &= \det(\mathbf{F})\mathrm{d}V = \det(\mathbf{F})\mathrm{d}S\mathbf{N}\mathrm{d}\mathbf{X} \\ &\implies (\mathrm{d}s\mathbf{n}\mathbf{F} - \mathrm{d}S\det(\mathbf{F})\mathbf{N})\,\mathrm{d}\mathbf{X} = 0 \\ &\implies \left(\mathrm{d}s\mathbf{F}^T\mathbf{n} - \mathrm{d}S\det(\mathbf{F})\mathbf{N}\right)\mathrm{d}\mathbf{X} = 0, \end{aligned}$$

we get *Nanson's formula*

$$\mathrm{d}s\mathbf{n} = \det(\mathbf{F})\mathbf{F}^{-T}\mathrm{d}S\mathbf{N}, \tag{1.6}$$

which relates the normal vector in the current configuration to the normal vector in the reference configuration.

Conservation of linear momentum

Newton's seconds law states that the change in linear momentum equals the net impulse acting on it. For a continuum material with constant mass density ρ this implies that

$$\int_{\omega} \rho\dot{\mathbf{v}}\mathrm{d}v = \mathbf{f}, \qquad \mathbf{f} = \int_{\partial\omega} \mathbf{t}\mathrm{d}s + \int_{\omega} \mathbf{b}\mathrm{d}v, \tag{1.7}$$

where $\mathbf{v}$ is the spatial velocity field, $\mathbf{t}$ is the traction acting on the boundary, and $\mathbf{b}$ is the body force. From *Cauchy's stress theorem* we know that there exists a second order tensor σ, known as the Cauchy stress tensor that is related to the traction vector by $\mathbf{t} = \sigma\mathbf{n}$, where $\mathbf{n}$ is the unit normal in the current configuration. Using the divergence theorem we get

$$\int_{\partial\omega} \mathbf{t}\mathrm{d}s = \int_{\partial\omega} \sigma\mathbf{n}\mathrm{d}s = \int_{\omega} \nabla\cdot\sigma\mathrm{d}v,$$

and by collecting the terms from (1.7) we arrive at Cauchy's momentum equation

$$\nabla \cdot \sigma + \mathbf{b} = \rho \dot{\mathbf{v}}. \tag{1.8}$$

The contribution from the body force ($\mathbf{b}$) and inertial term ($\rho \dot{\mathbf{v}}$) can be considered negligible compared to the stresses [41, 74, 55], which is why the force balance equations is typically only stated as

$$\nabla \cdot \sigma = \mathbf{0}. \tag{1.9}$$

Note that we have formulated the balance law in the current configuration. An equivalent statement can be formulated in terms of the reference configuration

$$\nabla \cdot \mathbf{P} = \mathbf{0}, \tag{1.10}$$

where $\mathbf{P}$ is the first Piola-Kirchhoff stress tensor. Note that the operator $\nabla \cdot$ acting on the Cauchy stress tensor represents differentiation with respect to coordinates in the current configuration, while when acting on the first Piola-Kirchhoff stress tensor represent differentiation with respect to coordinates in the referece configuration.

Conservation of angular momentum

Just like linear momentum, the angular momentum is also a conserved quantity. We will not go through the derivation, but state that as a consequence, the Cauchy stress tensor is symmetric

$$\sigma = \sigma^T. \tag{1.11}$$

Hyperelasticity

Even though experimental studies have indicated visco-elastic behavior of the myocardium [20, 31], a common assumption is to consider quasi-static behavior, meaning that the inertial term in (1.8) is negligible and static equilibrium is achieved at all points in the cardiac cycle. Therefore it is also possible to model the myocardium as a hyperelastic material,which is a type of elastic material. This means that we postulate the existence of a strain-energy density function

$\Psi : \text{Lin}^+ \to \mathbb{R}^+$, and that stress is given by the relation

$$\mathbf{P} = \frac{\partial \Psi(\mathbf{F})}{\partial \mathbf{F}}. \tag{1.12}$$

Since stress has unit Pa, we see that the strain-energy density function is defined as energy per unit reference volume, and has units $\frac{\text{Joule}}{m^3}$. The strain-energy density function relates the amount of energy that is stored within the material in response to a given strain. Hence, the stresses in a hyperelastic material with a given strain-energy density function, depend only on the strain, and not the path for which the material deforms. On the contrary, if the model had been visco-elastic we would expect to see hysteresis in the stress/strain curve, but this is not possible for a hyperelastic material.

Remark 1. *The second law of thermodynamics states that the total entropy production in a thermodynamic process can never be negative. Elastic materials define a special class of materials in which the entropy production is zero. Within this thermodynamic framework the strain-energy density function coincides (up to a constant) with the Helmholtz free energy density.*

General requirements for the strain-energy density function

Some general requirements must hold for the strain-energy function. First of all, we require that the reference state is stress free and that the stored energy increases monotonically with the deformation. Formally this can be stated simply as

$$\Psi(\mathbf{I}) = 0 \qquad \text{and} \qquad \Psi(\mathbf{F}) \geq 0.$$

Moreover, expanding or compressing a body to zero volume would require an infinite amount of energy, i.e

$$\begin{aligned} \Psi(\mathbf{F}) &\to \infty \qquad \text{as} \qquad \det \mathbf{F} \to 0 \\ \Psi(\mathbf{F}) &\to \infty \qquad \text{as} \qquad \det \mathbf{F} \to \infty \end{aligned}$$

We say that the strain energy should be objective, meaning that the stored energy in the material should be invariant with respect to change of observer. Formally we must have: *given any positive symmetric rank-2 tensor* $\mathbf{C} \in \text{Sym}$*:*

$$\Psi(\mathbf{C}) = \Psi(\mathbf{Q}\mathbf{C}\mathbf{Q}^T),\ \forall \mathbf{Q} \in \mathscr{G} \subseteq \text{Orth}. \tag{1.13}$$

Here Orth is the group of all positive orthogonal matrices. If $\mathscr{G} = \text{Orth}$ we say that the material is isotropic, and otherwise we say that the material is anisotropic. This brings us to another important issue, which is related to the choice of coordinate-system. Having to deal with different coordinate-systems, and mapping quantities from one coordinate-system to another can results in complicated computations. Therefore it would be beneficial if we could work with quantities which do not depend on the choice of coordinate-system. Such quantities are called invariants. If the material is isotropic, the representation theorem for invariants [78] states that Ψ can be expressed in terms of the principle invariants of $\mathbf{C}$, that is $\Psi = \Psi(I_1, I_2, I_3)$. The principle invariants $I_i, i = 1,2,3$ are the coefficients in the characteristic polynomial of $\mathbf{C}$, and is given by

$$I_1 = \operatorname{tr}\mathbf{C}, \qquad I_2 = \frac{1}{2}\left[I_1^2 - \operatorname{tr}(\mathbf{C}^2)\right] \qquad \text{and} \qquad I_3 = \det\mathbf{C}. \tag{1.14}$$

In the case when the material constitutes a transversely isotropic behavior, that is, the material has a preferred direction $\mathbf{a}_0$, which in the case of the myocardium could be the direction of fiber muscle fibers, we have

$$\mathscr{G} = \{\mathbf{Q} \in \text{Orth} : \mathbf{Q}(\mathbf{a}_0 \otimes \mathbf{a}_0)\mathbf{Q}^T = \mathbf{a}_0 \otimes \mathbf{a}_0\},$$

with $\otimes$ being the outer product. In this case the strain-energy density function can still be expressed through invariants. However, we need to include the so called quasi-invariants, which are defined as stretches in the local microstructural coordinate-system. The transversely isotropic invariants are given by

$$I_{4\mathbf{a}_0} = \mathbf{a}_0 \cdot (\mathbf{C}\mathbf{a}_0) \qquad \text{and} \qquad I_5 = \mathbf{a}_0 \cdot (\mathbf{C}^2\mathbf{a}_0).$$

Some of the invariants do have a physical interpretation. For instance, I_3 is related to the volume ratio of material during deformation, while $I_{4\mathbf{a}_0}$ is related to the stretch along the direction $\mathbf{a}_0$. Indeed the *stretch* ratio in the direction $\mathbf{a}_0$ is given by $\lambda_{\mathbf{a}_0} = |\mathbf{F}\mathbf{a}_0|$ and we see that $I_{4\mathbf{a}_0} = \mathbf{a}_0 \cdot (\mathbf{C}\mathbf{a}_0) = \mathbf{F}\mathbf{a}_0 \cdot (\mathbf{F}\mathbf{a}_0) = \lambda_{\mathbf{a}_0}^2$. For more details about invariants see e.g [36, 49].

The theory of global existence of unique solutions for elastic problems was originally based convexity of the free energy function. An energy function $\Psi : \text{Lin}^+ \to \mathbb{R}^+$ is strictly *convex* if for each $\mathbf{F} \in \text{Lin}^+$ and $\mathbf{H} \neq \mathbf{0}$ with $\det(\mathbf{F} + (1 -$

$\lambda)\mathbf{H}) > 0$, we have

$$\Psi(\lambda\mathbf{F}+(1-\lambda)\mathbf{H}) < \lambda\Psi(\mathbf{F})+(1-\lambda)\Psi(\mathbf{F}+\mathbf{H}), \qquad \lambda \in (0,1). \tag{1.15}$$

If the response $\mathbf{P}$ is differentiable, then condition (1.15) is equivalent of saying that the response is positive definite,

$$\mathbf{H} : \frac{\partial \mathbf{P}}{\partial \mathbf{F}} : \mathbf{H} > 0, \qquad\qquad \mathbf{F} \in \mathrm{Lin}^+, \mathbf{H} \neq \mathbf{0}. \tag{1.16}$$

However, from a physical point of view this requirement is too strict [5]. A slightly weaker requirement is the strong ellipticity condition which states that (1.16) should hold for any $\mathbf{H}$ of rank-one, and is analogous to say that the strain energy function is rank-one convex.

Incompressibility

The myocardium contains small blood vessels that supply the myocardial cells with oxygen. When the myocardium contracts, this perfused blood is squeezed out, resulting in an overall loss of 2-4% volume[83]. A material that change its volume in response to applied loads is referred to as compressible. When the volume is preserved we say that the material is incompressible. Since 2-4% is very little, a common assumption in cardiac mechanical modeling, which has also been made in the work conducted in this thesis, is to assume the myocardium to be incompressible. The reason for this choice is purely numerical.

For an incompressible material, only isochoric motions are possible. This means that the volume of the material does not change during any deformation, and hence we have the constraint

$$J = \det(\mathbf{F}) = 1. \tag{1.17}$$

The constraint (1.17) can be imposed by considering the modified strain energy function

$$\Psi = \Psi(\mathbf{F}) + p(J-1), \tag{1.18}$$

where p is a scalar which serves as a Lagrange multiplier, but which can be identified as the hydrostatic pressure. If we differentiate (1.18) with respect to $\mathbf{F}$ we get the First Piola-Kirchhoff stress tensor for an incompressible material

$$\mathbf{P} = \frac{\partial \Psi(\mathbf{F})}{\partial \mathbf{F}} + Jp\mathbf{F}^{-T}. \tag{1.19}$$

Likewise the Cauchy stress tensor is given by

$$\sigma = J^{-1}\frac{\partial \Psi(\mathbf{F})}{\partial \mathbf{F}}\mathbf{F}^{T} + p\mathbf{I}. \tag{1.20}$$

Remark 2. *The sign of p is determined by whether you add or subtract the term* $p(J-1)$ *to the total strain energy in* (1.18)*. For all practical purposes, it does not matter if you add or subtract the term as long as you are consistent.*

Uncoupling of volumetric and isochoric response

The total strain energy function in (1.18) can be written as a sum of isochoric and volumetric components. Let

$$\mathbf{F} = \mathbf{F}_{\text{vol}}\mathbf{F}_{\text{iso}}, \tag{1.21}$$

then $\mathbf{F}_{\text{vol}} = J^{1/3}\mathbf{I}$ and $\mathbf{F}_{\text{iso}} = J^{-1/3}\mathbf{F}$. For compressible materials (i.e with $J \neq 1$) it is important to consider only deviatoric strains in the strain-energy density function, so that $\Psi = \Psi_{\text{iso}}(\mathbf{F}_{\text{iso}}) + \Psi_{\text{vol}}(J)$. For incompressible material ($J = 1$), we have $\mathbf{F}_{\text{vol}} = \mathbf{I}$ so that such a decomposition seems unnecessary. However, a similar decomposition has shown to be numerically beneficial [79]. Note that, in this case, a similar decoupling of the stress tensors has to be done.

Boundary Conditions

Choosing the correct boundary conditions for the model is essential, and the choice should mimic what is observed in reality. To physiologically constrain the ventricle in a correct way is difficult, and different approaches has been proposed. The boundary condition at the endocardium is typically modeled as a Neumann boundary condition, representing the endocardial blood pressure. For the left ventricle we have

$$\sigma\mathbf{n} = -p_{\text{lv}}\mathbf{n},\ \mathbf{x} \in \partial\omega_{\text{endo LV}}, \tag{1.22}$$

and for the right ventricle, “lv” is substituted with “rv”. This condition has a negative sign because the unit normal **N** is pointing out of the domain, while the pressure is acting into the domain. Note that this condition is imposed on the current configuration, and to utilize the Lagrangian formulation we can pull back this condition to the reference configuration to obtain

$$\mathbf{PN} = -p_{\mathrm{lv}} J \mathbf{F}^{-T} \cdot \mathbf{N}, \ \mathbf{X} \in \partial \Omega_{\mathrm{endo\,LV}} \tag{1.23}$$

Likewise, it is common to enforce a Neumann boundary condition on the epicardium,

$$\mathbf{PN} = -p_{\mathrm{epi}} J \mathbf{F}^{-T} \cdot \mathbf{N}, \ \mathbf{X} \in \partial \Omega_{\mathrm{epi}}. \tag{1.24}$$

However, the pressure p_{epi} is often set to zero as a simplification.

There exist a variety of boundary conditions at the base. It is common to constrain the longitudinal motion of base, even though it is observed in cardiac images that the apex tend to be more fixed than the base. A recent study shows that taking into account the base movement is important to capture the correct geometrical shape [60]. However, this has not been done in the studies in this thesis. Fixing the longitudinal motion at the base is enforced through a Dirichlet boundary condition,

$$u_1 = 0, \ \mathbf{X} \in \partial \Omega_{\mathrm{base}}, \tag{1.25}$$

where u_1 is the longitudinal component of the displacement $\mathbf{u} = (u_1, u_2, u_3)$. To apply this type of condition, it is easiest if the base is flat and located at a prescribed location, for example in the $x = 0$ plane. Constraining the longitudinal motion of the base alone is not enough since the ventricle is free to move in the basal plane. In order to anchor the geometry it is possible to fix the movement of the base in all directions

$$\mathbf{u} = \mathbf{0}, \ \mathbf{X} \in \partial \Omega_{\mathrm{base}}, \tag{1.26}$$

or fixing the endocardial or epicardial ring

$$\mathbf{u} = \mathbf{0}, \ \mathbf{X} \in \Gamma_{\mathrm{endo}} \tag{1.27}$$

$$\mathbf{u} = \mathbf{0}, \ \mathbf{X} \in \Gamma_{\mathrm{epi}}. \tag{1.28}$$

Another approach which is used in this thesis is to impose a Robin type boundary condition at the base

$$\mathbf{P}\mathbf{N} + k\mathbf{u} = \mathbf{0}, \ \mathbf{X} \in \partial\Omega_{\text{base}}, \tag{1.29}$$

or at the epicardium to mimic the pericardium

$$\mathbf{P}\mathbf{N} + k\mathbf{u} = \mathbf{0}, \ \mathbf{X} \in \partial\Omega_{\text{epi}}. \tag{1.30}$$

Here k can be seen as the stiffness of a spring that limits the movement. The limiting cases, $k = 0$ and $k \to \infty$ represent free and fixed boundary respectively. More complex boundary conditions to mimic the pericardium are also possible [23], but not considered in this thesis. An overview of the location of the different boundaries for the bi-ventricular geometry is illustrated in Figure 1.5.

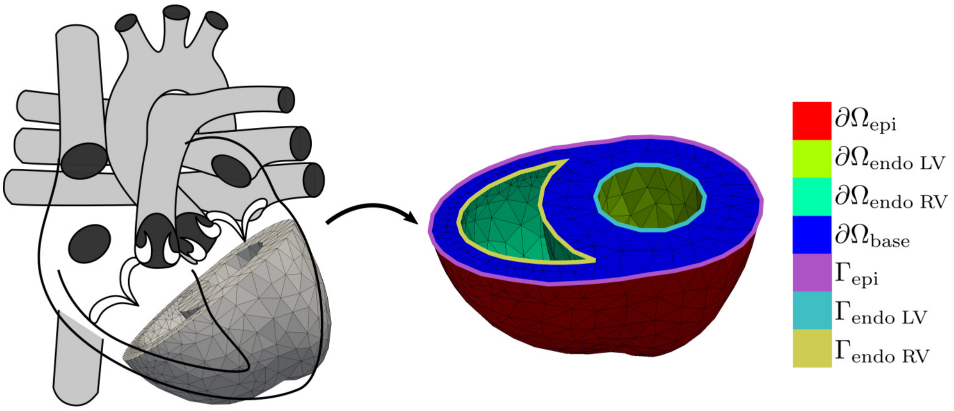
🟥 $\partial\Omega_{\text{epi}}$
🟩 $\partial\Omega_{\text{endo LV}}$
🟩 $\partial\Omega_{\text{endo RV}}$
🟦 $\partial\Omega_{\text{base}}$
🟪 Γ_{epi}
🟦 $\Gamma_{\text{endo LV}}$
🟨 $\Gamma_{\text{endo RV}}$

Figure 1.5: Illustration of the different boundaries in a bi-ventricular domain.

Force-balance equation

We will now collect all the terms that are involved in the force balance for the cardiac mechanics problem. Considering the myocardium as an incompressible, hyperelastic material we obtain the following strong form in the Lagrangian formulation

$$\begin{aligned} \nabla \cdot \mathbf{P} &= 0 \\ J - 1 &= 0, \end{aligned} \tag{1.31}$$

completed with appropriate boundary conditions. To solve this numerically using the finite element method, we need to derive the weak variational form of this equation.

Variational formulation

There are many ways to arrive at the variational formulation of the force-balance equations for the cardiac mechanics problem. One way is to consider the strong form in (1.31) and use the standard approach in the finite element method to multiply by test function in a suitable space, and perform integration by parts. Within the fields of continuum mechanics it is common to refer to this approach as the *principle of virtual work*, which states that the virtual work of all forces applied to a mechanical system vanishes in equilibrium. Within this framework, test functions are referred to as virtual variations. Another approach, which we will use here, derives the variational form by utilizing a fundamental principle in physics called the *principle of stationary potential energy*, or *minimum total potential energy principle*. This principle states that a physical system is at equilibrium when the total potential energy is minimized, and any infinitesimal changes from this state should not add any energy to the system. In order to make use of this principle we first need to sum up all the potential energy in the system. Here we separate between internal and external energy. Internal energy is energy that is stored within the material, for instance when you stretch a rubber band you increase its internal energy. External energy represent the contribution from all external forces such as gravity and traction forces. For an incompressible, hyperelastic material the total potential energy in the system is given by

$$\Pi(\mathbf{u}, p) = \Pi_{\text{int}}(\mathbf{u}, p) + \Pi_{\text{ext}}(\mathbf{u}). \tag{1.32}$$

$$\Pi_{\text{int}}(\mathbf{u}, p) = \int_{\Omega} [p(J-1) + \Psi(\mathbf{F})] \, \mathrm{d}V \tag{1.33}$$

$$\Pi_{\text{ext}}(\mathbf{u}) = -\int_{\Omega} \mathbf{B} \cdot \mathbf{u} \mathrm{d}V - \int_{\partial\Omega_N} \mathbf{T} \cdot \mathbf{u} \mathrm{d}S \tag{1.34}$$

Here $\mathbf{B}$ represents body forces acting on a volume element in the reference domain, e.g gravity, and $\mathbf{T} = \mathbf{PN}$ represents first Piola-Kirchhoff traction force acting on the Neumann boundary $\partial\Omega_N$. According to the *Principle of stationary potential energy* we have

$$D_{\delta\mathbf{u}}\Pi(\mathbf{u}, p) = 0, \qquad \text{and} \qquad D_{\delta p}\Pi(\mathbf{u}, p) = 0. \tag{1.35}$$

Here $\delta\mathbf{u}$ and δp are virtual variations in the space for the displacement and hydrostatic pressure respectively, and

$$D_{\mathbf{v}}\Phi(\mathbf{x}) = \frac{\mathrm{d}}{\mathrm{d}\varepsilon}\Phi(\mathbf{x}+\varepsilon\mathbf{v})\big|_{\varepsilon=0} \tag{1.36}$$

is the directional derivative of Φ at $\mathbf{x}$ is the direction $\mathbf{v}$. This operator is also known as the Gâteaux operator. The virtual variations $\delta\mathbf{u}$ and δp represents an arbitrary direction with infinitesimal magnitude. We have

$$0 = D_{\delta p}\Pi(\mathbf{u},p) = \int_{\Omega}\delta p(J(\mathbf{u})-1)\mathrm{d}V, \tag{1.37}$$

and

$$0 = D_{\delta\mathbf{u}}\Pi(\mathbf{u},p) = \int_{\Omega}\left[pJ\mathbf{F}^{-T}+\mathbf{P}\right] : \mathrm{Grad}\delta\mathbf{u}\mathrm{d}V - \int_{\Omega}\mathbf{B}\cdot\delta\mathbf{u}\mathrm{d}V$$

Note that the traction forces are now incorporated into the stress tensors after application of the divergence theorem. These equations are also commonly referred to as the Euler-Lagrange equations. Here $\mathbf{u} \in V = \left[H_D^1(\Omega)\right]^3$, with $H_D^1(\Omega) = \{\mathbf{v} : \int_{\Omega}\left[|\mathbf{v}|^2 + |\mathrm{Grad}\mathbf{v}|^2\right]\mathrm{dV} < \infty \wedge \mathbf{v}\big|_{\partial\Omega_D} = 0\}$ and $p \in Q = L^2(\Omega)$, with $\partial\Omega_D$ representing the Dirichlet boundary. In summary, the Euler-Lagrange equations written in a mixed form reads : *Find* $(\mathbf{u},p) \in V \times Q$ *such that*

$$\begin{pmatrix} D_{\delta p}\Pi(\mathbf{u},p) \\ D_{\delta\mathbf{u}}\Pi(\mathbf{u},p) \end{pmatrix} = \mathbf{0}. \qquad \forall\,(\delta\mathbf{u},p) \in V \times Q. \tag{1.38}$$

Discretization of the force balance equations

Equation (1.31) is only possible to solve analytically for very simplified problems. Therefore we need to employ numerical methods to solve the problem. One such method is the finite element method (FEM). When using the finite element method, we often refer to such approximation as a Galerkin approximation. This is based on approximating the solution by linear combinations of basis functions in a finite dimensional subspace of the true solution. If V and Q are two suitable Hilbert spaces for the displacement $\mathbf{u}$ and the hydrostatic pressure p respectively, we now select some finite dimensional subspaces $V_h \subset V$ and $Q_h \subset Q$, which are spanned by a finite number of basis functions.

For incompressible problems such as (1.31), we cannot choose the approximation spaces V_h, Q_h at random. A known numerical issue that arises for such saddle-point problems is *locking*, which can be seen if the material do not deform even if forces are applied. The problem is solved by requiring the finite element approximation to satisfy the discrete inf-sup condition [46]. There exist several mixed elements that satisfies this condition [14]. The elements used in this thesis are the Taylor-Hood finite elements [75]. Let the domain of interest be denoted by Ω, and let $\mathscr{T}_h$ be a triangulation of that domain in the sense that $\bigcup_{T \in \mathscr{T}_h} T = \overline{\Omega}$. Let $\mathscr{P}_k(T)$ be the linear space of all polynomials of degree $\leq k$ defined on T. Then for $k \geq 2$, the Taylor-Hood finite element spaces are the spaces

$$V_h = \{\phi \in C(\Omega) \mid \phi \big| T \in \mathscr{P}_k(T), T \in \mathscr{T}_h\}, \tag{1.39}$$

$$Q_h = \{\phi \in C(\Omega) \mid \phi \big| T \in \mathscr{P}_{k-1}(T), T \in \mathscr{T}_h\}, \tag{1.40}$$

where $C(\Omega)$ denotes the space of continuous function on Ω. In this thesis we have exclusively used these elements with $k = 2$.

Remark 3. *The basis functions that span the Taylor-Hood finite element spaces are also known as the Lagrangian basis functions. These basis functions, of degree n, are polynomials of degree n on each element, but only continuous at the nodes (i.e not continuously differentiable). Consequently, differentiating a function that is expressed as a linear combination of the Lagrangian basis functions, will not be continuous at the nodes, and therefore caution has to be made when evaluating features that depends on the derivative of such functions. Examples of such features are stress and strain with depends on the deformation gradient which again depends on the derivative of the displacement. One way to deal with this issue is to 1) use other types of elements that are continuously differentiable everywhere, such a the cubic Hermite elements or 2) evaluate the features at the Gaussian quadrature points where there is no problem with continuity.*

Constitutive relations

We have now covered a mechanical framework which holds any for material in general. What differentiate the mechanics of soft living tissue, like the myocardium, from other materials is the constitutive relations which describes the response of a material to applied load. Such constitutive relations often comes from experimental observations, both observations of anatomical structure but also from experiments done on tissue slabs.

We have already covered the theory of hyperelasticity and incompressibility in Section 1.3.3 and 1.3.4 respectively which are types of constitutive relations.

In this section we will cover constitutive relations which only apply to soft living tissue such as the myocardium. In particular, we will consider a complete constitutive model of the mechanical behavior of the myocardium that accounts for both the passive and the active response of the myocardium.

Modeling of the passive myocardium

The passive response of the myocardium has been investigated through uni-axial, bi-axial and shear deformation experiments [20]. In 2009 Holzapfel and Ogden proposed an orthotropic constitutive model of the passive myocardium [36] which is based on the experiments done in [20], and is the model used in this thesis. Other constitutive models for the passive myocardium exists [17, 30, 56] but is not considered here. The model assumes a local orthonormal coordinate system with the fiber axis $\mathbf{f}_0$, sheet axis $\mathbf{s}_0$ and sheet-normal axis $\mathbf{n}_0$. From this coordinate system we define the invariants

$$\begin{aligned} I_1 &= \operatorname{tr}(\mathbf{C}), \\ I_{4\mathbf{f}_0} &= \mathbf{f}_0 \cdot (\mathbf{C}\mathbf{f}_0), \\ I_{4\mathbf{s}_0} &= \mathbf{s}_0 \cdot (\mathbf{C}\mathbf{s}_0), \\ I_{8\mathbf{f}_0\mathbf{s}_0} &= \mathbf{s}_0 \cdot (\mathbf{C}\mathbf{f}_0), \end{aligned} \tag{1.41}$$

Here $I_{4\mathbf{f}_0}$ and $I_{4\mathbf{s}_0}$ are the stretches along the fiber, sheet axis respectively and $I_{8\mathbf{f}_0\mathbf{s}_0}$ is related to the angle between the fiber and sheets in the current configuration given that they are orthogonal in the reference configuration. Note that since $(\mathbf{f}_0, \mathbf{s}_0, \mathbf{n}_0)$ is an orthonormal system, we have the relation $I_1 = I_{4\mathbf{f}_0} + I_{4\mathbf{s}_0} + I_{4\mathbf{n}_0}$, and so $I_{4\mathbf{n}_0}$ is redundant. The orthotropic Holzapfel and Ogden model reads

$$\begin{aligned} \Psi(I_1, I_{4\mathbf{f}_0}, I_{4\mathbf{s}_0}, I_{8\mathbf{f}_0\mathbf{s}_0}) =& \frac{a}{2b}\left(e^{b(I_1-3)} - 1\right) \\ &+ \frac{a_f}{2b_f}\left(e^{b_f(I_{4\mathbf{f}_0}-1)_+^2} - 1\right) \\ &+ \frac{a_s}{2b_s}\left(e^{b_s(I_{4\mathbf{s}_0}-1)_+^2} - 1\right) \\ &+ \frac{a_{fs}}{2b_{fs}}\left(e^{b_{fs}I_{8\mathbf{f}_0\mathbf{s}_0}^2} - 1\right). \end{aligned} \tag{1.42}$$

Here $(x)_+ = \frac{1}{2}(x + |x|)$, so that the the terms involving $I_{4\mathbf{f}_0}$ and $I_{4\mathbf{s}_0}$ only contribute to the stored energy during elongation. From (1.42) we see that it is easy to identify the physical meaning of each term. For example the first term represents the isotropic contribution which is the overall stiffness in the extracellular matrix while the second term accounts for the extra stiffness along the fibers when they are elongated. It is also straight forward to prove that the strain-energy function is convex, and that the requirements for existence and uniqueness discussed in Section 1.3.3 are fulfilled.

In this thesis we have used a transversely isotropic version of (1.42) which is obtained by setting $a_{fs} = b_{fs} = a_s = b_s = 0$, i.e

$$\Psi(I_1, I_{4\mathbf{f}_0}) = \frac{a}{2b}\left(e^{b(I_1-3)} - 1\right) + \frac{a_f}{2b_f}\left(e^{b_f(I_{4\mathbf{f}_0}-1)_+^2} - 1\right). \tag{1.43}$$

If we further set $a_f = b_f = b = 0$ so that in a is the only nonzero parameter, then the Holzapfel-Ogden model reduces (after a series expansion of the exponential and a limiting argument) to

$$\Psi(I_1) = \frac{a}{2}(I_1 - 3), \tag{1.44}$$

which is the model of a Neo Hookean material. The Cauchy stress can be derived analytically from (1.42), by using the chain rule and (1.20),

$$\begin{aligned} J\sigma =& \frac{\partial \Psi(\mathbf{F})}{\partial \mathbf{F}}\mathbf{F}^T + p\mathbf{I} = \sum_{i \in \{1, 4\mathbf{f}_0, 4\mathbf{s}_0, 8\mathbf{f}_0\mathbf{s}_0\}} \psi_i \frac{\partial I_i}{\partial \mathbf{F}}\mathbf{F}^T + p\mathbf{I} \\ =& p\mathbf{I} + a\left(e^{b(I_1-3)} - 1\right)\mathbf{B} + 2a_f(I_{4\mathbf{f}_0} - 1)_+ e^{b_f(I_{4\mathbf{f}_0}-1)^2}\mathbf{f}\otimes\mathbf{f} \\ & + 2a_f(I_{4\mathbf{s}_0} - 1)_+ e^{b_f(I_{4\mathbf{s}_0}-1)^2}\mathbf{s}\otimes\mathbf{s} + a_{fs}I_{8\mathbf{f}_0\mathbf{s}_0}e^{b_{fs}I_{8\mathbf{f}_0\mathbf{s}_0}^2}\left(\mathbf{f}\otimes\mathbf{s} + \mathbf{s}\otimes\mathbf{f}\right), \end{aligned} \tag{1.45}$$

where $\mathbf{B} = \mathbf{F}\mathbf{F}^T$ is the left Cauchy-Green tensor, $\mathbf{f} = \mathbf{F}\mathbf{f}_0$ and $\mathbf{s} = \mathbf{F}\mathbf{s}_0$.

Modeling of the active contraction

One feature that separates the myocardium from other hyperelastic materials such as rubber, is its ability to actively generate force without external loads. This active component of the model can be incorporated using two fundamentally different approaches known as the *active stress* and *active strain* formulation.

The *active stress* approach is based on the classical three element Hill model illustrated in Figure 1.6, where the active contribution naturally decomposes the total stress into a sum of passive and active stresses [57]. Hence, in the active stress formulation [40] one assumes that the total Cauchy stress σ can be written

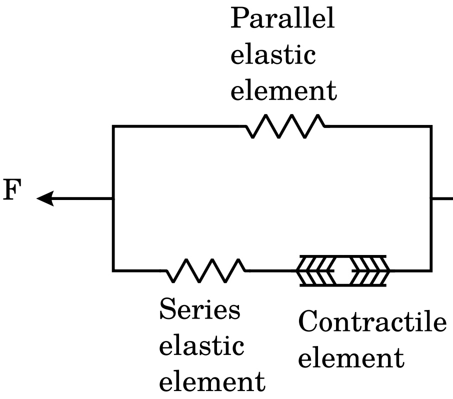

Figure 1.6: The classical three-element Hill muscle model with one contractile element and two non-linear springs, one arranged in series and one parallel.

as an additive sum of one passive contribution σ_p and one active contribution σ_a,

$$\sigma = \sigma_p + \sigma_a \tag{1.46}$$

The passive contribution is determined by the material model used

$$\sigma_p = \frac{1}{J}\frac{\partial \Psi(\mathbf{F})}{\partial \mathbf{F}}\mathbf{F}^T, \tag{1.47}$$

while the active contribution is given by

$$\sigma_a = \sigma_{ff}\mathbf{f}\otimes\mathbf{f} + \sigma_{ss}\mathbf{s}\otimes\mathbf{s} + \sigma_{nn}\mathbf{n}\otimes\mathbf{n}, \tag{1.48}$$

and the different constants σ_{ff}, σ_{ss}, and σ_{nn}, which are the active stress in the fiber, sheet and sheet-normal direction respectively, are typically coupled to the electrophysiology and calcium dynamics. There are experimental evidence that the active stresses in the transverse direction of the fibers (σ_{ss}, and σ_{nn}), are non-negligible [48], and one approach is to assume a uniform transverse activation in which the total active tension can be written as

$$\sigma_a = T_a\left[\mathbf{f}\otimes\mathbf{f} + \eta\left(\mathbf{s}\otimes\mathbf{s} + \mathbf{n}\otimes\mathbf{n}\right)\right], \tag{1.49}$$

where η represent the amount of transverse activation and $T_a \in \mathbb{R}$ is the magnitude of the active tension. In the limiting case ($\eta = 0.0$), the active tension acts purely along the fibers and (1.49) reduces to

$$\sigma_a = T_a \mathbf{f} \otimes \mathbf{f}. \tag{1.50}$$

Note that, by observing that

$$\frac{\partial I_{4\mathbf{a}_0}}{\partial \mathbf{F}} = \frac{\partial (\mathbf{a}_0 \cdot \mathbf{C}\mathbf{a}_0)}{\partial \mathbf{F}} = 2\mathbf{a} \otimes \mathbf{a}_0 \implies \mathbf{a} \otimes \mathbf{a} = \frac{1}{2} \frac{\partial I_{4\mathbf{a}_0}}{\partial \mathbf{F}} \mathbf{F}^T$$

and that $I_1 = I_{4\mathbf{f}_0} + I_{4\mathbf{s}_0} + I_{4\mathbf{n}_0}$, we can instead decompose the strain-energy function into a passive and active parts [61], $\Psi = \Psi_p + \Psi_a$, with

$$\Psi_a = \frac{T_a}{2J} \left((I_{4\mathbf{f}_0} - 1) + \eta \left[(I_1 - 3) - (I_{4\mathbf{f}_0} - 1) \right] \right), \tag{1.51}$$

so that $J\sigma_a = \frac{\partial \Psi_a}{\partial \mathbf{F}} \mathbf{F}^T$.

The *active strain* formulation is a relatively new way of modeling the active contraction in the heart and was first introduced in [73]. This formulation is based on a multiplicative decomposition of the deformation gradient,

$$\mathbf{F} = \mathbf{F}_e \mathbf{F}_a. \tag{1.52}$$

The active part $\mathbf{F}_a$, is an inelastic process driven by the biochemistry and can be seen as the actual distortion of the microstructure. The elastic part $\mathbf{F}_e$ is responsible for preserving compatibility of the tissue and stores all the energy in the deformations. As a consequence, the strain energy function is a function of the elastic deformation gradient only. The decoupling can be illustrated by considering two sarcomeres connected in series as shown in Figure 1.7.

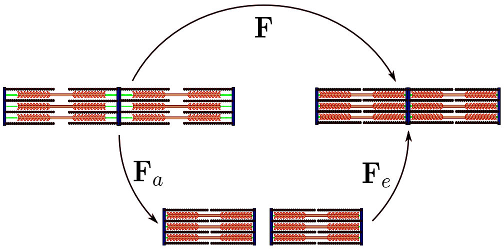

Figure 1.7: Illustration of the active strain formulation. During the active deformation, the sarcomeres shortens as if they were all detached. The elastic deformation ensures compatibility of the tissue.

The general form of the active deformation gradient for a material with an orthotropic active response is given by

$$\mathbf{F}_a = \mathbf{I} - \gamma_f \mathbf{f}_0 \otimes \mathbf{f}_0 - \gamma_s \mathbf{s}_0 \otimes \mathbf{s}_0 - \gamma_n \mathbf{n}_0 \otimes \mathbf{n}_0 \tag{1.53}$$

We add the constraint $\det(\mathbf{F}_a) = 1$, meaning that the active deformation is volume preserving. Further we assume that the activation is transversely isotropic, so that the sheet and sheet-normal axis is treated in the same way. It is then straight forward to verify that $\gamma_n = \gamma_s = 1 - (1 - \gamma_f)^{-1/2}$, and we have

$$\mathbf{F}_a = (1 - \gamma)\mathbf{f}_0 \otimes \mathbf{f}_0 + \frac{1}{\sqrt{1-\gamma}}(\mathbf{I} - \mathbf{f}_0 \otimes \mathbf{f}_0), \tag{1.54}$$

where we set $\gamma = \gamma_f$ for convenience.

While the motivation behind the active stress formulation is purely physiological and based on the classical Hill model shown in Figure 1.6, the motivation behind the active strain formulation is more driven by ensuring mathematical robustness. In particular it has been shown [4] that with the active strain formulation, properties such as frame invariance and rank-one ellipticity is inherited from the strain energy function. In contrast, rank-one ellipticity is not guaranteed for the active stress formulation.

For a more extensive comparison of the active stress and active strain approach we refer to [4, 26], and for an overview of other methods to model the active contraction we refer to [27].

Implementation details

The cardiac mechanics solver developed during the work of this thesis is implemented using the finite element framework FEniCS. Here we briefly explain the main components of FEniCS as well as some numerical considerations made when implementing the solver.

The FEniCS Project

The FEniCS project is an open-source computing platform for solving partial differential equations (PDEs) using the finite element method (FEM). Solving PDEs using FEM involves many implementation details that can be tedious to implement yourselves. The idea behind FEniCS is to automate code generation so that the user can spend more time on doing research and less time on implementation of assembly matrices. At the core of FEniCS is DOLFIN [52], which is a

C++/Python library, and works as the main interface in FEniCS. In this thesis only the Python interface has been used, in which C++ code is automatically generated using SWIG. This allows for simplicity through the Python scripting language and the speed of the C++ language. The domain specific language used to represent weak formulations is called the Unified Form Language (UFL) [2], and allows for e.g automatic differentiation of forms and expressions. The FEniCS form compiler (FFC) [51] compiles code written in UFL to Unified Form-assembly Code (UFC) [3] which are optimized C++ code. The Python interface also makes use of the Instant module which allows for just-in-time (JIT) compilation of C++ code. The compiled code is also stored in a cache so that compilation of a form only happens once. Also, the relatively new UFL Analyser and Compiler System (UFLACS) allows for fast compilation of complex forms such as variational formulations that include the Holzapfel Ogden material model (1.42).

For more information about FEniCS, the reader is referred to the official web page (https://fenicsproject.org) or any of the cited literature.

Numerical considerations

The solution of non-linear problems such as the one described here are typically solved using methods like Newton's method. The convergence of such methods depends on the initial guess, and if the initial guess is too far from the true solution, the solver might diverge. Moreover, if the initial guess is close to the true solution the convergence rate is in general quadratic.

Let us consider a typical numerical problem of inflating the ventricular geometry from a stress-free configuration to end-diastole. This involves increasing the pressure, or the boundary traction on the endocardium, from zero to the end-diastolic pressure. A strategy know as the *incremental load* technique is usually a good approach. In this strategy you select some incremental step-size (for instance 0.4 kPa), and increase the pressure linearly until the target pressure is reached. If the solver diverges you decrease the step-size (for instance by a factor of 0.5) until convergence is reached, and continue to step up the pressure with the new step-size. This is very robust, but definitely a slow approach. Since many of the constitutive models for myocardium consist of an exponential relationship between the stress and strain (so called Fung-type relation), the amount of stress needed to displace a material will be higher if the material is a state with high strain compared to a state of low strain. Therefore, in the low strain state, the Newtons solver might perform fewer iterations to reach convergence when the load is increased. As a result, one could improve the incremental load technique by adapting the step size if the number of newton iterations are below a certain threshold (for instance 8 iterations).

An even more clever strategy uses a technique from bifurcation and chaos theory and is known as numerical continuation [1]. Suppose we want to solve the non-linear problem $F(\mathbf{u},\lambda) = 0$ with state variable $\mathbf{u}$ and parameter λ. For instance $\mathbf{u}$ could be the displacement and λ could be the endocardial pressure. The idea behind numerical continuation is that given a solution pair $(\mathbf{u}_0, \lambda_0)$ there exist (under conditions stated by the implicit function theorem) a solution curve $\mathbf{u}(\lambda)$ such that $F(\mathbf{u}(\lambda),\lambda) = 0$ and $\mathbf{u}(\lambda_0) = \mathbf{u}_0$. To explicitly find such a curve is not always easy but a simple approximation can be found by linear extrapolation: Given two pairs $(\mathbf{u}_0, \lambda_0)$ and $(\mathbf{u}_1, \lambda_1)$, and a new target parameter λ_2, a possible solution is

$$\mathbf{u}_2 = (1-\delta)\mathbf{u}_0 + \delta\mathbf{u}_1 \qquad\qquad \delta = \frac{\lambda_2 - \lambda_0}{\lambda_1 - \lambda_0}. \tag{1.55}$$

Choosing $\mathbf{u}_2$ as initial guess for the non-linear solver has been successfully performed by others in non-linear cardiac mechanics problems [63], and this approach is also used in this thesis.

Personalization of Cardiac Biomechanics

In this section we will go through the steps needed to personalize the mechanical model developed in the previous section. We will start by giving a brief overview of the interaction between medical imaging and cardiac computational modeling. Then we will explain how the geometries are extracted from the medical images and turned into computational geometries that we can use for finite element computations. Finally we will explain how to incorporate additional data into model by means of adjoint based data assimilation techniques.

Medical Imaging

Since the discovery of X-ray in 1895, medical imaging has played a central role in diagnosis, treatment planning and follow-up. Without the huge advancements in medical imaging the last decades, computational models would not have been as important and promising as they have become.

Cardiac computational modeling often relies on data obtained using medical imaging techniques, and the quality of such data is therefore of fundamental importance [44]. It is clear that without advancements in medical imaging technology, the role of computational models would be limited to simple, idealized cases. With access to high quality images, detailed information about cardiac structure can be used to e.g build anatomically correct models. The computational models can then later be validated using the same images, or additional data can be extracted from the images in order to compute potential biomarkers. Figure 1.8 summarizes this interaction between medical images and computational models.

Today there are three main non-invasive imaging modalities used in cardiology. These are echocardiography (Echo), magnetic resonance imaging (MRI) and computed tomography (CT). Each modality offers advantages and disadvantages over the other. For example, MRI provides high quality images, uses zero radiation, but is expensive and lacks temporal resolution. CT can more accurately reconstruct the 3D image in contrast to MRI, in which 2D slices needs to be glued together to form a 3D surface. However, CT exposes the patient to radiation, which increases the chance of developing cancer. Finally echocardiography is easy to use, cheap, harmless, and has good temporal resolution, but is clearly inferior when it comes to image quality.

The main modality used in this thesis is 4D echocardiography, and we will therefore focus on data acquired using this modality. With 4D we mean three

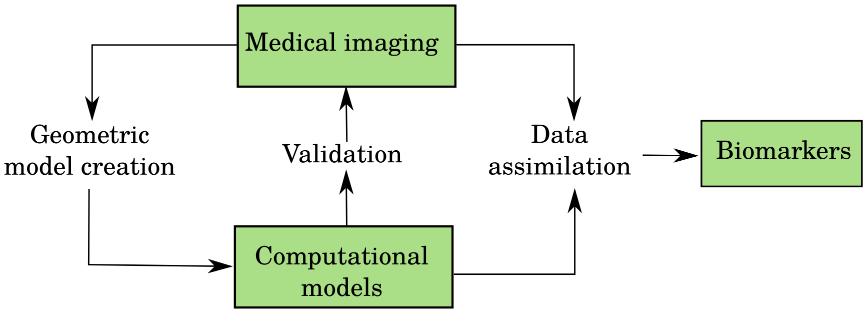

Figure 1.8: Interaction between medical imaging and computational models. Medical images are used to extract geometric structure. These geometries together with the computational models can later be validated against the medical images. Computational models can also be used together with the medical images to assimilate additional data in order to extract clinically useful biomarkers.

spatial and one temporal dimension. The speed of sound in human tissue (which is approximately 1540 m/s) put some limitations on the image quality versus the frame-rate [65] for these 3D volume images. In order to enhance these 3D volume images, disjoint subvolumes acquired during N cardiac cycles (N typically between 2 and 8)[9] are stitched together.

The images are further processed using some image segmentation tool. One such tool is EchoPac, which is used for analyzing images acquired with the echo scanner from GE Vingmed (Horten, Norway). The 4D Auto LVQ tool in EchoPac, is a tool for processing 3D echo images, and can be used to extract traces of volume, triangulated surfaces and 3D strain traces [34], together with a structured mesh of the American Heart Association (AHA) segments [12] for each time point, see Figure 1.9.

Geometry and microstructure

Mesh generation

In this section we will explain how to generate a left ventricular mesh based on segmented surfaces coming from 4D echocardiography. Figure 1.9 shows an example of how the exported data from the image segmentation tool look like. For each time point we can extract triangulated surfaces of the endocardium and epicardium which can be seen in Figure 1.9a. Together with these surfaces we are also given a so called strain mesh (Figure 1.9b) located approximately in the midwall, which defines the approximate location of the AHA-segments [12], and can

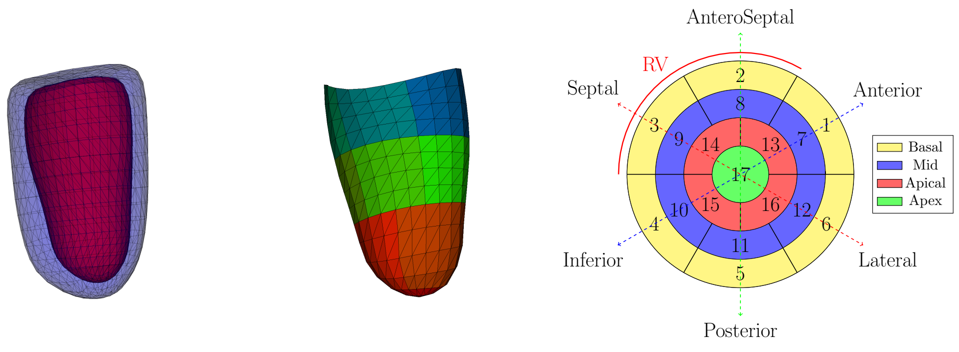

(a) (b) (c)

Figure 1.9: Figure 1.9a shows triangulated surfaces of the endo- and epicardium, and Figure 1.9b shows a structured mesh of the American Heart Association (AHA) segments. These surfaces are exported from the image segmentation tool EchoPac. Figure 1.9c shows the American Heart Association (AHA) segments illustrated on a so called bullseye plot with name and numbers on the different segments.

be used to orient the surfaces.

As discussed in Section 1.3.5, we constrain the basal movement in the longitudinal direction, which is easiest to accomplish using a flat base located at a prescribed location. In order to make the base flat, we first orient the surfaces so that the longitudinal axis is aligned with the x-axis, and the apex pointing in the positive x direction. To construct the basal plane we first take out the basal points from the strain mesh, and use these points to construct a least square fitting plane (Figure 1.10a). Let $(x_i, y_i, z_i), i = 1, \cdots, N$ be the basal points, and suppose the basal plane solves the equation $z = ax + by + c$, for some unknown constants a, b, c. Following a least square approach, we select the parameters (a, b, c) that minimizes to sum

$$\sum_{i=1}^{N} (ax_i + by_i + c - z_i)^2 . \tag{1.56}$$

Once the parameters for the basal plane are found we adjust the size of the cut, by moving the plane along the longitudinal axis (here $x-$axis), until the cavity volume agrees with the measured volume given by the image segmentation tool within some specified tolerance. When the correct cut size is found, the points above the plane is removed, and the remaining surfaces are smoothed using the mesh generation tool GAMer [84].

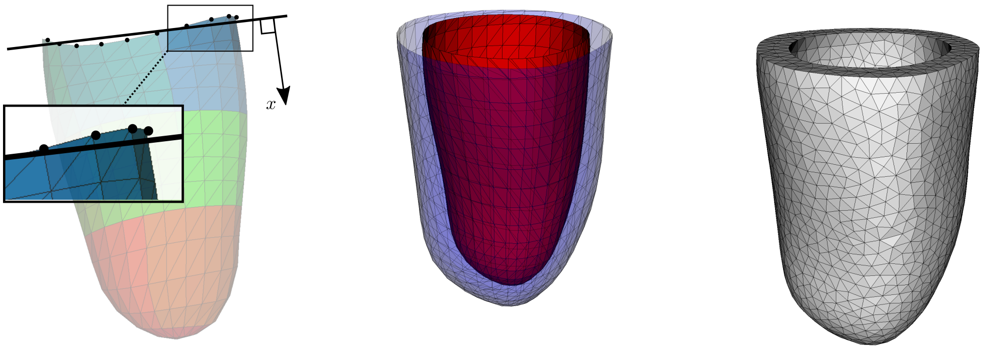

(a) (b) (c)

Figure 1.10: A least square fitting plane is fitted to the points belonging to the basal boundary in the strain mesh (Figure 1.10a). This plane is used to cut the endo- and epicardial surfaces (Figure 1.10b) and Gmsh is used to mesh these surfaces together (Figure 1.10c).

The actual mesh generation is performed using Gmsh [25], which mesh the endocardial and epicardial surface together using frontal-Delaunay meshing algorithm. Gmsh also marks the endocardial, the epicardial and the basal facets, along with the endocardial and epicardial basal rings.

Remark 4. *The cavity volume is computed by generating the whole mesh, and then computing the volume using Equation* (1.63)*. The cut size is found by using a one-dimensional optimization algorithm with the objective functional representing the squared error between computed and measured volume.*

Rule-based fiber architecture

Both the passive and active properties of the myocardium depends on the underlying muscle fiber architecture, and it is therefore of high relevance to capture this architecture as accurately as possible.

Unfortunately, imaging technology does not currently provide a way of extracting patients-specific fiber orientation *in vivo*. Diffusion Tensor MRI (DT-MRI) [6] can be utilized to reconstruct the fiber and laminar structure *ex vivo*[67], and recent studies have shown promising results in measuring fiber orientations *in vivo* using DT-MRI [76]. By using DT-MRI measurements of multiple hearts it is possible to build statistical atlases [62] which could be used to generate fiber fields based on transformation between a patient-specific geometry and the geometries from the atlas [77].

An alternative method for assigning myocardial fiber orientation is by rule-based methods [64, 7]. In this thesis we have used an algorithm called the Laplace – Dirichlet Rule-Based (LDRB) algorithm, proposed by Bayer et al [7].

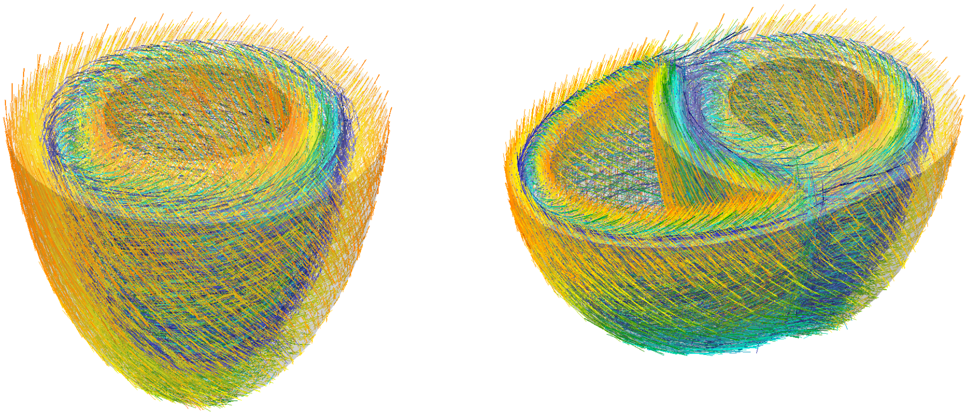

Figure 1.11: The LDRB algorithm [7] applied to an LV (left) and BiV (right) geometry with an helix fiber angle of 60° and $-60°$ on the endo- and epicardium respectively. Color represents the helical angle, with blue being 0° (circumferential) which can be seen in the midwall.

The LDRB algorithm takes as input the geometry Ω, the helical fiber angle on the endo- and epicardium (α_{endo} and α_{epi}) and the transverse fiber angle on the endo- and epicardium (β_{endo} and β_{epi}), and outputs a set of three orthogonal vector fields, one representing the fiber angle $(\mathbf{f}_0)$, one representing the sheet angle $(\mathbf{s}_0)$ and the final direction is called the sheet normal direction $(\mathbf{n}_0)$. Figure 1.11 shows the output of this algorithm applied to both an LV and a BiV ellipsoidal geometry.

The ventricular coordinate system

When dealing with geometric shapes such as a left ventricle, finding a coordinate system that is easy to work with is important. For example, when studying spherical shapes, the spherical coordinate system is usually easier to work with. Likewise, a coordinate system that is easy to use when studying ellipsoidal shapes like the left ventricle is the *prolate spheroidal coordinate system* [41]. The Cartesian coordinates (x,y,z) are related to the prolate spheroidal coordinates by

$$\begin{aligned} x &= a \sinh \mu \sin \nu \cos \theta, \\ y &= a \sinh \mu \sin \nu \sin \theta, \\ z &= a \cosh \mu \cos \nu, \end{aligned} \tag{1.57}$$

where a is the focal point, $\nu \in [0, \pi]$ is the *longitudinal* coordinate, $\theta \in [0, 2\pi]$ is the *circumferential* azimuth angle and μ is the *radial* coordinate. For an ellipse given by the equation $\frac{x^2}{b^2} + \frac{y^2}{c^2} = 1$ with b being the semi-major axis, and c the semi-minor axis, the focal point is given by

$$a = \sqrt{b^2 - c^2}. \tag{1.58}$$

The prolate spheroidal coordinate axes are illustrated in Figure 1.12a. The inverse relation, going from the Cartesian coordinate (x, y, z) to the prolate spheroidal coordinate (μ, ν, θ) given the focal point a, is a bit more intricate, but can be computed as follows

$$\begin{aligned} \nu &= \arccos(\tau), \\ \mu &= \operatorname{arccosh}(\rho), \\ \theta &= \arctan \frac{z}{y}, \\ \tau &= \frac{1}{2a}\big(\sqrt{(x+a)^2 + y^2 + z^2} \\ &\quad + \sqrt{(x-a)^2 + y^2 + z^2}\big), \\ \rho &= \frac{1}{2a}\big(\sqrt{(x+a)^2 + y^2 + z^2} \\ &\quad - \sqrt{(x-a)^2 + y^2 + z^2}\big). \end{aligned} \tag{1.59}$$

It is possible to estimate the focal point by taking b in (1.58) to be the maximum distance from the base to the apex, and c the maximum radius at the base. Using this estimate, the base is assumed to be located approximately at the center of the ellipsoid, i.e $\nu = \pi/2$ [45].

This coordinate system can be used when e.g marking the mesh according to the AHA segments and to create vector fields in the longitudinal, circumferential and radial direction. These vector fields are useful when comparing the simulated results to the image-based measurements.

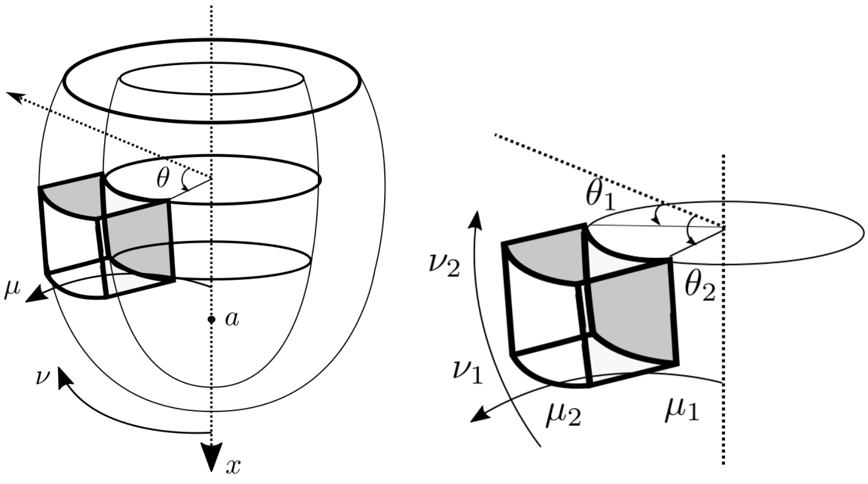

(a) (b)

Figure 1.12: Illustration of the prolate spheroidal coordinate system.

Choosing the reference geometry

A general problem in biomechanics is that the geometry extracted from imaging data is not the stress-free geometry, meaning that the geometry that we observe is subjected to a physical load, e.g blood pressure. In order for the stress and strain to be correct, we need to find a geometry, so that when loaded with the measured loads, gives back the geometry observed in the medical images. This is analogous to the problem of finding the geometry of a deflated balloon, given that we have an image of an inflated version of the balloon. Having this picture in mind, it is intuitive that such a geometry not necessarily is unique. Several techniques have been applied in order to estimate the unloaded geometry, such as the inverse design analysis (ID) [29] or the modified updated Lagrangian formulation (MULF) [24]. Other approaches includes using the mid-diastolic or end-systolic geometry. Another popular technique is a fixed point iteration scheme, known as the backward displacement method [8]. Figure 1.13 illustrate the backward displacement method applied to an LV geometry. We briefly explain the steps in this methods.

Suppose you are given geometry $\Omega_{\mathscr{I}}$ taken from some medical image, which is loaded with a pressure $p_{\mathscr{I}}^{\mathrm{LV}}$ (assume LV only of simplicity). We want to find the unloaded geometry $\Omega_{\mathscr{U}}$, so that when we load $\Omega_{\mathscr{U}}$ with $p_{\mathscr{I}}^{\mathrm{LV}}$, you get back the starting geometry $\Omega_{\mathscr{I}}$. Let $\mathbf{X}_{\mathscr{I}}$ denote the coordinates in $\Omega_{\mathscr{I}}$, and let $\mathbf{d}$ denote the displacement field which is the solution of (1.38) after applying the pressure $p_{\mathscr{I}}^{\mathrm{LV}}$. What we want, is to find $\mathbf{X}_{\mathscr{U}}$ so that $\mathbf{X}_{\mathscr{I}} = \mathbf{X}_{\mathscr{U}} + \mathbf{d}(\mathbf{X}_{\mathscr{U}})$. To find $\mathbf{X}_{\mathscr{U}}$ we

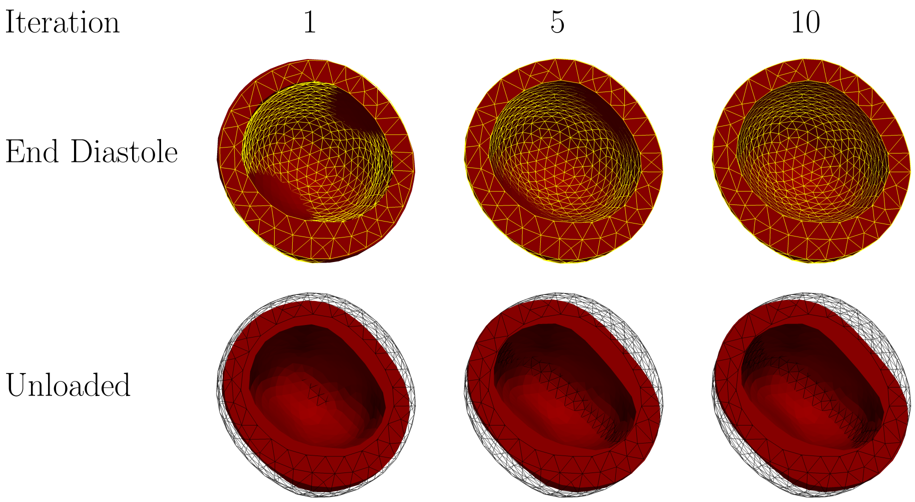

Figure 1.13: Showing 1, 5, and 10 iterations of the backward displacement method applied to a left ventricular geometry. To row top shows the original geometry in solid and the inflated unloaded geometry in yellow wire-frame for 1,5 and 10 iterations. Bottom row shows the unloaded geometry in solid and the original image based geometry in wire-frame.

let

$$\mathbf{X}_{n+1} = g(\mathbf{X}_n) = \mathbf{X}_{\mathscr{I}} - \mathbf{d}(\mathbf{X}_n), \qquad \mathbf{X}_0 = \mathbf{X}_{\mathscr{I}}. \tag{1.60}$$

According to Banach Fixed Point Theorem, the mapping g has a fixed-point if $\|\nabla g\|_\infty = \|\nabla \mathbf{d}\|_\infty < 1$. This means that as long as the deformation resulting from the applied pressure does not result in a stretch that is more than 100%, this method will converge. Of course the question about convergence of the fixed point method is one thing. Another thing is the convergence of the nonlinear solver. For bi-ventricular geometries, the backward displacement method might fail to converge, especially if the tissue is soft and the pressure in the right ventricle is high. In this case the right ventricular free wall might collided with the septal wall when subtracting the displacement. An example of this is illustrated in Figure 1.14.

An alternative to the backward displacement method that does not necessary converge towards a fixed point but provides a more stable way of obtaining an unloaded configuration was proposed in Ragahavan et. al [66]. In this algorithm, only one iteration of the backward displacement method is applied but the subtracted displacement is multiplied by a scalar k, which could be estimated to minimizing some residual.

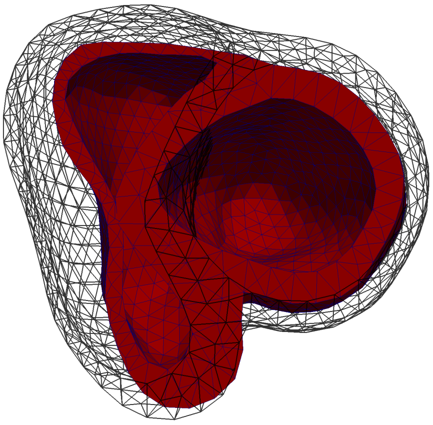

Figure 1.14: Backward displacement method might fail for bi-ventricular geometries. This can be seen be noticing that the RV free wall is buckling and colliding with the septum. Here the image-based geometry is shown in black wire-frame, while the estimated unloaded geometry is shown in red.

Since the backward displacement method really does converge towards a fixed point, it is favorable to the Rahavan method. Therefore, a hybrid approach is to apply the backward displacement method as long as the non-linear solver converges, and switch to the Rahavan method upon divergence.

Coupled material parameter estimation and unloading algorithm

One thing to note is that the unloaded configuration depends upon the chosen material parameters, which are generally also unknown. For example, applying the backward displacement method to a geometry will result in a smaller unloaded cavity volume if the material is softer. Therefore, the material parameters estimation is coupled to the problem of finding the unloaded, zero pressure geometry. In [58], Nikou et al proposed a method for estimating material parameters and the unloaded geometry by iterating between the two methods, and terminating if the difference in unloaded cavity volume was less than 5%. This method is general and could be applied using any unloading algorithm and any method to estimate the material parameters. In the last paper in this thesis, we analyze this method and show that it actually converges to the correct solution and is stable to noise in the measurements.

Data Assimilation

The constitutive laws in cardiac mechanics comes from experiments done on tissue slabs, and relates stress in the material to strain. If we had the same data available for a given patient we could easily have performed a regression analysis to identify the parameters in the constitutive model. However, this type of data typically requires that tissue samples are taken from the myocardium, which is not an option when dealing with living humans. In general, when dealing with physical systems such as the heart or the weather, it is not always possible to design an experiment which allow us to determine all properties of a physical system [15]. In such cases we have to take the measurements that we have, and do our best to incorporate them into the model.

For example, the type of data that we usually have available, are data that can be extracted using imaging techniques such as motion data, volume traces, regional strain traces etc. One technique to estimate model parameters based on such observations is called data assimilation.

The field of data assimilation has its roots in meteorology, where a typical problem is to make predictions on the weather, based on observations (of temperature, humidity etc.) at different locations.

There are basically two main approaches to assimilate data; *sequential data assimilation* and *variational data assimilation*. Sequential data assimilation, which is often referred to as filtering, is based on a predictor-corrector approach where you start from your initial data and use a filter to predict the next state. Once you have your measurement available you correct the estimate based on the new observations. Some examples of sequential procedures include Kalman filtering and Luenberger observers [15].

The other approach which is taken in this thesis is called variational data assimilation, and also referred as 4D-var. This approach is based on minimizing a cost functional that represents the mismatch between observations and simulations, with possibly additional regularization terms added to the objective functional. For a more thorough review of other data assimilation techniques we refer to the paper by Chapelle et. al [15].

Pipeline

We will now explain the general setup and the main steps in variational data assimilation, and will denote the *state variable* by $\mathbf{w}$, which is our case represents jointly the displacement and hydrostatic pressure $\mathbf{w} = (\mathbf{u}, p)$.

The state variables are described by some *physical forward model* $\mathscr{M}$, which is our case is governed by the force balance equation in (1.31). Moreover this model typically depends on some parameters μ that we want to adjust based on the observations at hand. We will refer to these parameters as the *control parameters*. For example, the control parameters could be related to the stiffness of the myocardium which we want to adjust to each individual patient based on some clinical observations. We can therefore assume that the underlying model can be written in the form $\mathscr{M}(\mathbf{w}, \mu) = 0$. Note that the state variable $\mathbf{w}$ typically depends on the control parameters μ, but to ease notation, we do not write this dependency explicitly

We are also given a set of measurements (or observations) that we want to assimilate, and we denote a single observation by y. For example, y might by a volume measurements at some given time point in the cardiac cycle, measured using e.g ultrasound and image processing techniques. The *observation operator* $\mathscr{H}$, is approximation of the observation, and act as an operator from the state space to the observation space. For a single observation, we therefore have the relation

$$y = \mathscr{H}(\mathbf{w}) + \xi, \tag{1.61}$$

where $\xi = \xi_{\mathscr{H}} + \xi_{\mathbf{y}}$ represents both the error in the measurements ($\xi_{\mathbf{y}}$) (e.g noise in the data) and error in the representation of the observation ($\xi_{\mathscr{H}}$) (that $\mathscr{H}$ do not represent the data good enough).

Finally all observations are combined into a single cost function $\mathscr{J} = \mathscr{J}(\mathbf{w}, \mu)$ which represents the overall mismatch between observations and simulations. The aim is to minimize this functional while ensuring that the governing force balance equation is satisfied. This can be done in the following steps

1. For some initial guess μ_0, solve the forward model $\mathscr{M} = 0$ to obtain $\mathbf{w}_0$.
2. Compute $\mathscr{J}(\mathbf{w}_0, \mu_0)$.
3. Compute the gradient $D\mathscr{J}(\mathbf{w}_0, \mu_0)$ to find the direction of the steepest descent.
4. Move along the steepest direction and update the initial guess.

The above steps are continued until we have reached a minimum for the cost functional, e.g when the norm of the gradient becomes zero. In practice we continue these steps until either the norm of the gradient is below a prescribed tolerance, or the number of iterations exceed a maximum number. Using this gradient descent approach will always bring you towards a minimum. However, the minimum you find might not be a global minimum. In this case, the choice of initial guess determines which local minima you will end up in. If you can prove that your cost functional is convex with respect to the control parameters, you known that the minimum you find is a global one.

The data assimilation pipeline is summarized in Figure 1.15.

Remark 5. *There exists gradient-free optimization methods that can be used to avoid gradient computations. Examples include genetic algorithms or particle swarm algorithms. The drawback with such methods is that they typically requires a lot of functional evaluations. In our case functional evaluations are very computationally expensive, because every functional evaluation requires a solution of the non-linear forward model.*

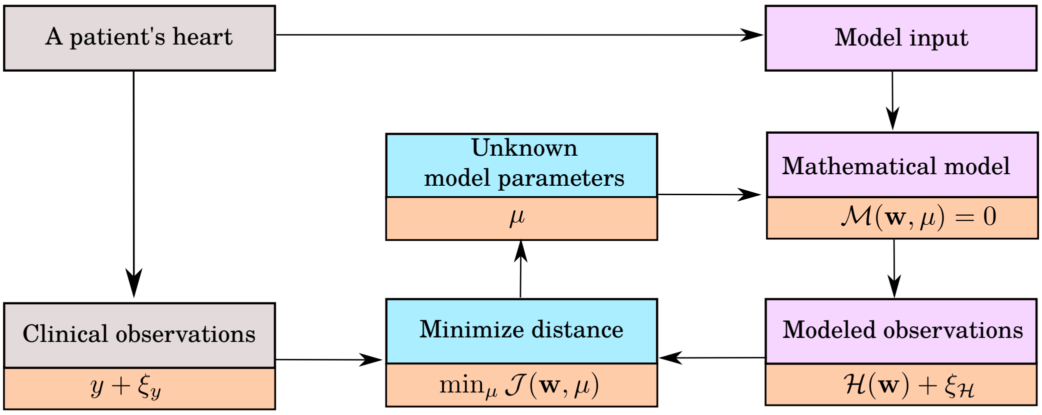
A patient's heart
Model input
Unknown model parameters
μ
Mathematical model
$\mathcal{M}(\mathbf{w}, \mu) = 0$
Clinical observations
$y + \xi_y$
Minimize distance
$\min_\mu \mathcal{J}(\mathbf{w}, \mu)$
Modeled observations
$\mathcal{H}(\mathbf{w}) + \xi_{\mathcal{H}}$

Figure 1.15: The different components involved in the data assimilation procedure. The mathematical description of each component is displayed below each box. From a patients heart we typically extract information that are used as input to the model. This can for instance be information about geometry or information about boundary conditions. This model input is used to create a mathematical model of the heart, which also depends on some parameters μ. These unknown parameters are determined by minimizing the distance between the clinical observations y and the modeled observation $\mathscr{H}(\mathbf{w})$.

We will now describe some of the main observation operators used in this thesis before we explain how to solve the data assimilation problem efficiently using the adjoint method.

The volume observation operator $\mathscr{H}_{\text{volume}}$ In some cases, the ventricular cavity volume can easily be computed analytically from the displacement field $\mathbf{u}$. Denote the inner cavity of the left ventricle in the current configuration by ω_{endo}. Further let dv and $\mathbf{x}$ denote an infinitesimal volume element and the coordinate in the current configuration respectively. Then by the divergence theorem we have

$$\mathscr{H}_{\text{volume}}(\mathbf{u}) = \int_{\omega_{\text{endo}}} \mathrm{d}v = \frac{1}{3}\int_{\omega_{\text{endo}}} \nabla \cdot \mathbf{x} \mathrm{d}v = \frac{1}{3}\int_{\partial \omega_{\text{endo}}} \mathbf{x} \cdot \mathbf{n} \mathrm{d}s, \tag{1.62}$$

where $\mathbf{n}$ and ds are the unit normal and a surface element on the current configuration respectively. Note that the boundary $\partial \omega_{\text{endo}}$ includes the endocardial basal boundary. However in the case when the base is flat and fixed in longitudinal direction and located at the $x = 0$ plane, the contribution from this boundary integral will be zero. In this case the boundary integral will be the same as the integral over the endocardial boundary, with the only change being the change of sign on the normal vector. By Nansons formula we obtain

$$\mathscr{H}_{\text{volume}}(\mathbf{u}) = -\frac{1}{3}\int_{\partial \Omega_{\text{endo}}} (\mathbf{X} + \mathbf{u}) J \mathbf{F}^{-T} \mathbf{N} \mathrm{d}S, \tag{1.63}$$

where now $\partial \Omega_{\text{endo}}$, $\mathbf{X}$, $\mathbf{N}$ and dS are respectively the endocardial surface, the reference coordinate, the unit normal and a surface element in the reference configuration.

The strain observation operator $\mathscr{H}_{\text{strain}}$ Another observation that is encountered in this thesis is strain, or more precisely average regional strain in the circumferential, radial or longitudinal direction. Let Ω_j denote the volume for which the strain should be averaged over, and let $\mathbf{e}_k$ denote the unit vector field in the preferred strain direction. Then for a given strain tensor $\mathbf{A}$ we define

$$\mathscr{H}_{\text{strain}}(\mathbf{u}) = \frac{1}{|\Omega_j|}\int_{\Omega_j} \mathbf{e}_k^T \mathbf{A}(\mathbf{u}) \mathbf{e}_k \mathrm{d}V. \tag{1.64}$$

The strain tensor $\mathbf{A}$ is typically chosen to be the Green-Lagrange strain tensor $\mathbf{E}$, or the material displacement gradient tensor $\mathbf{F} - \mathbf{I}$.

Remark 6. *Measured strains are computed relative to some reference geometry, which do not always coincide with the reference geometry chosen for your simulation (for example if you use the unloaded geometry). In these cases you have to either recompute the measured strain according to the chosen reference for* *the simulation, or recompute the simulated strains according to the correct reference geometry for your measurements. In the latter case, the strain tensor can be computed using the modified deformation gradient* $\tilde{\mathbf{F}} = \mathbf{F}\mathbf{F}_{\mathrm{ref}}^{-1}$ *where* $\mathbf{F}_{\mathrm{ref}}$ *is the deformation gradient from your current reference to the correct reference state.*

PDE-constrained optimization

The variational data assimilation problem in cardiac mechanics belongs to a class of problems called PDE-constrained optimization problems, which can be formulated as follows:

$$\begin{aligned} &\underset{\mu \in P}{\text{minimize}} && \mathscr{J}(\mathbf{w}, \mu) \\ &\text{subject to} && \mathscr{M}(\mathbf{w}, \mu) = 0. \end{aligned} \tag{1.65}$$

Here $\mathscr{J}(\mathbf{w}, \mu) : W \times P \mapsto \mathbb{R}$ is the objective functional that we want to minimize, $W = V \times Q$ is the state space, P is the parameter space and $\mathscr{M}(\mathbf{w}, \mu) = 0$ is the force balance equation given by (1.31).

The typical way of solving the problem (1.65) is to turn the constrained problem into an unconstrained problem. One way to do this is to consider the *reduced functional*

$$\widehat{\mathscr{J}}(\mu) = \mathscr{J}(\mathbf{w}(\mu), \mu). \tag{1.66}$$

Since $\widehat{\mathscr{J}}$ is a pure function of μ, we have eliminated the constraint and turned the problem into an unconstrained problem:

$$\underset{\mu \in P}{\text{minimize}} \quad \widehat{\mathscr{J}}(\mu). \tag{1.67}$$

Note that a solution to (1.67) satisfies the optimality condition $D\widehat{\mathscr{J}} = 0$. In the following, D refers to the total derivative with respect to the control μ, while D_x refers to the partial derivative with respect to x.

Computing the functional gradient

To move along the gradient descent it is required to actually compute this functional gradient. The "naive" approach would be to estimate the gradient using finite difference approximation. However, this requires one functional evaluation for each degree of freedom in the parameter space, so when the number of parameters are large this becomes impractical.

By the chain rule we have

$$D\widehat{\mathscr{J}} = D\mathscr{J}(\mathbf{w}(\mu),\mu) = D_{\mu}\mathscr{J}(\mathbf{w}(\mu),\mu) + D_{\mathbf{w}}\mathscr{J}(\mathbf{w}(\mu),\mu)D_{\mu}\mathbf{w}(\mu).$$

The terms $D_{\mathbf{w}}\mathscr{J}(\mathbf{w}(\mu),\mu)$ and $D_{\mu}\mathscr{J}(\mathbf{w}(\mu),\mu)$ are typically straight forward to compute. The term $D_{\mu}\mathbf{w}(\mu)$, on the other hand, is more involved. If we take the total derivative of the force balance equation, we obtain

$$D\mathscr{M}(\mathbf{w}(\mu),\mu) = D_{\mathbf{w}}\mathscr{M}(\mathbf{w}(\mu),\mu)D_{\mu}\mathbf{w}(\mu) + D_{\mu}\mathscr{M}(\mathbf{w}(\mu),\mu) = 0,$$

and we see that

$$D_{\mathbf{w}}\mathscr{M}(\mathbf{w}(\mu),\mu)D_{\mu}\mathbf{w}(\mu) = -D_{\mu}\mathscr{M}(\mathbf{w}(\mu),\mu). \tag{1.68}$$

The system (1.68) is known as the tangent linear system, and can be computed numerically using ordinary algorithmic differentiation techniques. However it requires that you first specify the parameter μ, meaning that it becomes expensive to compute the functional gradient at several control points.

We could instead plug in the solution to (1.68) to get

$$D\widehat{\mathscr{J}} = D_{\mu}\mathscr{J}(\mathbf{w}(\mu),\mu) - z^{*}D_{\mu}\mathscr{M}(\mathbf{w}(\mu),\mu), \tag{1.69}$$

where

$$\begin{aligned} z^{*} &= D_{\mathbf{w}}\mathscr{J}(\mathbf{w}(\mu),\mu)\left(D_{\mathbf{w}}\mathscr{M}(\mathbf{w}(\mu),\mu)\right)^{-1} \\ \implies z^{*}D_{\mathbf{w}}\mathscr{M}(\mathbf{w}(\mu),\mu) &= D_{\mathbf{w}}\mathscr{J}(\mathbf{w}(\mu),\mu) \end{aligned}$$

Note that in (1.69), the variable z^{*} represents a Lagrange multiplier enforcing the PDE constraint. In order to solve this system, we need to have it on the form $A\mathbf{x} = b$, and we take the adjoint (Hermitian transpose) to get

$$D_{\mathbf{w}}\mathscr{M}(\mathbf{w}(\mu),\mu)^{*}z = D_{\mathbf{w}}\mathscr{J}(\mathbf{w}(\mu),\mu)^{*} \tag{1.70}$$

Equation (1.70) is called the adjoint equation. To compute the gradient we can now solve for z and then insert z^{*} into (1.69) to compute the gradient.

Dolfin-Adjoint

Dolfin-Adjoint [22] is a software package that is based on the FEniCS project, which aims to derive the discrete adjoint equation and the tangent linear models of finite element models implemented within the FEniCS framework. While the traditional approach is to derive the adjoint code from the forward code using automatic differentiation tools, Dolfin-Adjoint utilizes the high level symbolic representation [2] in FEniCS to derive the discrete adjoint equations from the discrete forward equations, and then the FEniCS system derives the adjoint code from the discrete adjoint equations. For more information about Dolfin-Adjoint the reader is referred to the official web page (http://www.dolfin-adjoint.org/en/latest/).

Multiobjetive optimization

Parameters in the model are estimated based on minimizing a cost functional representing the mismatch between observations and simulations. Assume we are given N different observations, then in principle we have N different cost functionals to minimize:

$$\begin{aligned} \underset{\mu \in P}{\text{minimize}} \quad & \{\mathscr{J}_1(\mathbf{w},\mu), \mathscr{J}_2(\mathbf{w},\mu), \cdots, \mathscr{J}_N(\mathbf{w},\mu)\} \\ \text{subject to} \quad & \mathscr{M}(\mathbf{w},\mu) = 0 \end{aligned} \tag{1.71}$$

with

$$\mathscr{J}_i(\mu) = (\mathbf{y} - \mathscr{H}(\mathbf{w}(\mu)))^2, \; i = 1, \cdots, N \tag{1.72}$$

The above observations comes from the same source, and hence it should be intuitive that minimizing one of them, would also bring the other closer to a minimum. However, with the presence of noise in the data, this might not always be the case, and hence we have conflicting objectives. Problem (1.71) is called a multiobjetive optimization problem [19]. Such problems typically do not have a single optimal solution, but a family of solutions called *Pareto optimal solutions*. The basic methods for solving such problems includes *the weighted method* and *the ε-constraint method*. In this thesis we have only used the weighted method, which is based on minimizing a weighted sum of the individual cost functionals, i.e:

$$\begin{aligned} \underset{\mu \in P}{\text{minimize}} \quad & \sum_{i=1}^{N} \lambda_i \mathscr{J}_i(\mathbf{w}, \mu) \\ \text{subject to} \quad & \mathscr{M}(\mathbf{w}, \mu) = 0. \end{aligned} \tag{1.73}$$

Here λ_i represents a weighting of the different objectives, and the choice of λ_i should be based on 1) the importance of objective i and 2) the relative size of the cost functional $\mathscr{J}_i$. It is also common to require $\sum_i \lambda_i = 1$ so that the weighted sum is a convex combination of the objective functionals.

Regularization

Regularization is an important concept in many scientific disciplines concerned with data fitting. When using data that essentially are realizations of a stochastic process, we need to take into account that the data are corrupted with noise. Moreover, the model we are using is a simplification of a physical process, and fitting the data exactly to the model is unrealistic. This is especially important if the number of parameters we are trying to estimate are more than the number of data points used as input. In such cases it is often beneficial to make some assumptions about the solution we are looking for in order to avoid overfitting. For example, we may assume that the parameter we are searching for is smooth. Suppose that $\mu \in H^1(\Omega)$ is the parameter we want to find, and that we want to favor smooth solutions. Then the norm of the gradient $\|\nabla \mu\|$ should be small. One way to achieve this is to add a penalty term to the objective functional so that instead of minimizing $\mathscr{J}(\mathbf{w}, \mu)$ we minimize $\mathscr{J}(\mathbf{w}, \mu) + \lambda \|\nabla \mu\|$, where the constant λ, known as the regularization parameter, controls the smoothness of μ. Note that in the limit $\lambda \to \infty$ we would end up with a constant value of μ. This approach is referred to as Tikhonov regularization.

Another reason for using regularization is to stabilize the solver for the underlying PDE that we solve. Parameters with sharp spikes can make Newtons iterations in-feasible, and restricting the parameter space to exclude such solutions might help to stabilize the Newton solver.

Identifiability of parameters

When dealing with parameter estimation, you should always consider questions about identifiability and uniqueness. This depends on the model, the data and the objective functional [32]. A first test should be to generate synthetic data with some prescribed parameters, feed this error-free data to the data assimilation method, and ensure that you are able to retrieve the parameters that generated that data. If you end up with a different parameter set than the one generated the data, your problem is not *structurally identifiable* [13]. Your problem is said to be *practical identifiable* if the parameters can be determined uniquely based on the data at hand. If the test passes you should try to add noise to the data, and see if your data assimilation is stable with respect to noise in the measurements.

Demonstrating identifiability is often difficult, especially when your data is corrupted with noise, and when the complexity of the model increases. Balancing the complexity of the model in terms of *model fidelity*, i.e whether your model is rich enough to represent the data, and the identifiability is often key in order to have robust model. A too simple model will often fail to represent your data, while a too complex model might give completely different answers with just a slight perturbation of the data, i.e with noise added to the measurement. The same problem is encountered in other scientific disciplines. For example, in statistical learning theory, *overfitting* is related to overparameterization of the model, in which you can perfectly represent your data, but a small perturbation will cause a significant error.

Another problem, which is also related to identifiability is the question about uniqueness of the solution. A practical test is to start the optimization algorithm from different initial points and see if you end up at the same optimum. If this does not happen, it is likely that the objective functional is not convex, which is a requirement for uniqueness. Unfortunately, this is the case for many problems in PDE-constrained optimization. In these cases, the objective functional might have several distinct local minima, in which case different techniques for finding the best local minima exist [21].

Extraction of biomarkers

As can be seen from Figure 1.8, data assimilation of computational models and medical imaging can be used to extract biomarkers. By biomarker, we mean an indicator of some biological of physiological process that gives insight into the state or condition of that process. Examples of biomarkers that can be extracted from a computational model are parameters related to tissue stiffness, like the parameters in the Holzapfel-Ogden material law (1.43), parameters related to contractility like the active stress (T_a in (1.49)) or the active strain (γ in (1.54)), or estimates or myofiber stress. Computational models open a new door when it comes to extraction of biomarkers, and mechanical features such as stress, contractility and elastance can easily be computed using a computational model. Of course, validation of these models is what matter most in order to make these biomarkers clinically useful [11].

Summary of papers

In this final introductory section we summarize the papers that make up this thesis, and we also give some final concluding remarks and future directions.

Paper 1: High-resolution data assimilation of cardiac mechanics applied to a dyssynchronous ventricle

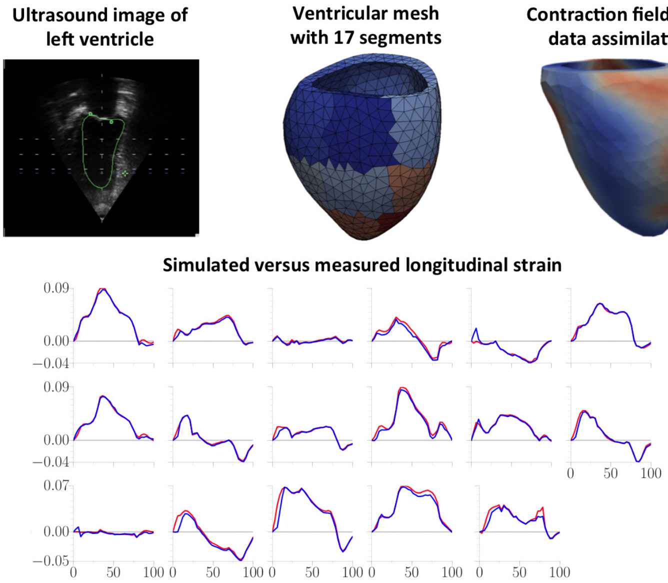

Figure 1.16: Summary figure for paper 1

In this paper we develop and test a pipeline for constructing a patient-specific mechanical simulation of a patient's heart, based on clinical measurements and adjoint-based data assimilation techniques.

As a model case we consider one patient, diagnosed with left bundle branch block and selected for cardiac resynchronization therapy (CRT). Prior to the CRT implantation the patient had 4D echocardiography taken for which the LV geometry, LV volumes and LV regional strains throughout the cardiac cycle are measured. During implantation of the CRT device the LV pressure were also measured invasively. The LV pressure measurements were used as boundary condition at the endocardium, while the LV volume and LV regional strain were incorporated into a cost functional that we wanted to minimize.

The pipeline is divided into two phases, a passive phase where we estimate the linear isotropic parameters a in (1.43) as a global material parameter using the measurement points belonging atrial systole, and an active phase where we estimate a spatially varying contraction parameter (γ in (1.54)) at each measurement point with active contraction. During the passive phase we only fit the volumes, while during the active phase a total of 51 strain measurements in the radial, longitudinal and circumferential direction in each AHA segment (Figure 1.9) were used additionally in the optimization.

The results show an excellent fit with measured strain an volume, with a average relative error in the volume and strain of less than 0.4 % and 3 % respectively using a contraction parameter with one degree of freedom for each vertex in the geometry (2661 parameters in total). Parameters at lower spatial resolution are also tested to show the necessity of high spatial resolution to fit the measured strain data. A synthetic test is also performed in order to show that the method is able to recapitulate the generated data, also with noise added to the data. Moreover, a sensitivity analysis to different parameters are presented in the appendix.

Paper 2: Estimating cardiac contraction through high resolution data assimilation of a personalized mechanical model

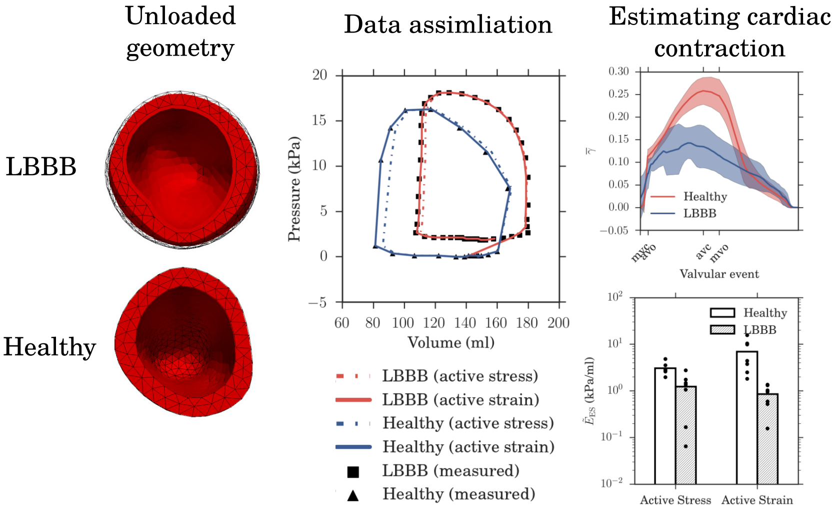

Figure 1.17: Summary figure for paper 2

In this paper we apply the method developed in the previous paper to a cohort of patients and estimate indices of cardiac contractility. More specifically, a group of seven patients diagnosed with left bundle branch block and selected for cardiac resynchronization therapy (CRT), and a group of seven healthy control subjects were included in the study.

The pipeline is similar to the one outlined in paper 1, with the exception that we also estimate the unloaded, stress-free configuration using the method outlined in Section 1.4.3.

The optimized active strain parameter in (1.54) as well as the optimized active stress parameter in (1.49) are averaged over the ventricle and compared between the two groups. The healthy group showed a significant increase in both of these parameters. Furthermore, an estimation of the end-systolic elastance by perturbation of the model at the end-systolic state, while fixing the remaining quantities, was also conducted. This estimate of end-systolic elastance were also significantly higher in the healthy control group.

Paper 3: Efficient estimation of personalized biventricular mechanical function employing gradient-based optimizatio

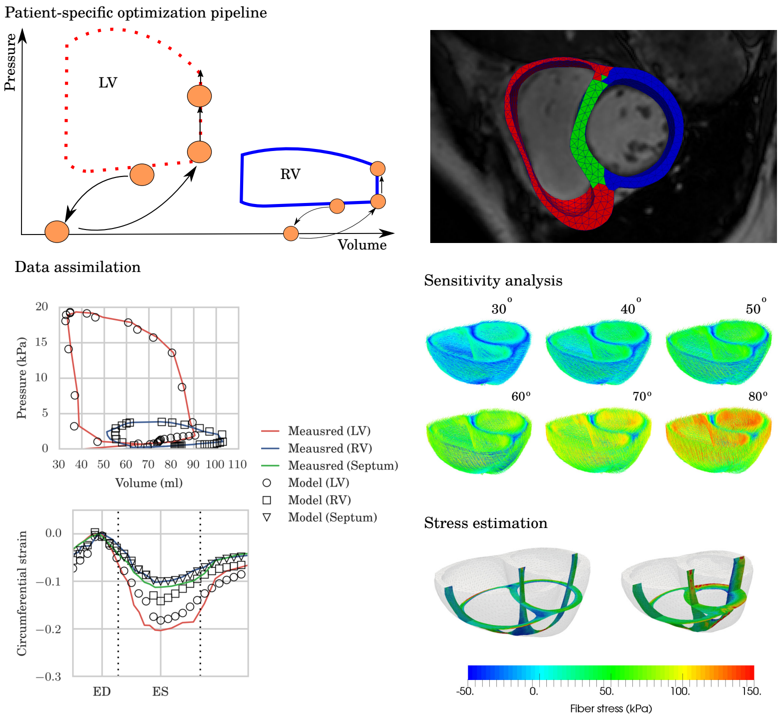

Figure 1.18: Summary figure for paper 3

In this paper we extend the work in the two previous paper to bi-ventricular geometries, and use it to estimate patient-specific myofiber stress and indices of contractility. Furthermore, we investigate the sensitivity of these computed features the helical fiber angle and the choice of active modeling framework.

In this work we estimate the linear isotopic material parameter in (1.43), spatially resolved on the LV and RV, by minimizing the error in end-diastolic LV and RV cavity volumes. We use a simplified algorithm to estimate the unloaded geometry, since the problem of estimating an unloaded BiV-geometry is not well-posed because buckling of the RV free wall might occur. The amount of active contraction is estimated during the active phase, by minimizing simulated and measured volumes and circumferential strain. The active control parameter, which are γ in (1.54) and T_a in (1.49) for the active strain and active stress formulation respectively, are spatially resolved on the LV free wall (LVFW), the RV free wall (RVFW) and the septum. With so few control parameters, issues related to conflicting objectives, i.e that is is not possible to minimize both the strain and volume, is evident. However, with a low dimensional parameter space, questions regarding identifiability and uniqueness of the estimated parameters are easier to answer. In this study we also perform a validation of the model, by comparing simulated and measured longitudinal strain which is not used in the optimization.

The results show low variability with respect to choice of fiber angle and active modeling framework. Also, the fit of data depends upon the choice of fiber angle, and a steeper fiber angle than previously suggested, provides the best fit. The work here could potentially be used to extract patient-specific maps of ventricular fiber stress and contractility which could be useful in diagnostic of several heart diseases related to heart failure.

Paper 4: Assessment of regional myocardial work from a patient-specific cardiac mechanics model

In this paper we investigate if it is possible to assess regional myocardial work using data assimilation and finite element modeling. The amount of work performed by the left ventricle equals to the amount to work needed to eject blood against the intraventricular pressure. Effectively, a global measure of work is therefore the same as the area of the pressure volume (PV) loop which is most commonly refered to as stroke work. However, stroke work is a global measure which does not reflect whether some regions in the ventricle work harder than others to compensate for regional dysfunction, in order to maintain the stroke work needed to

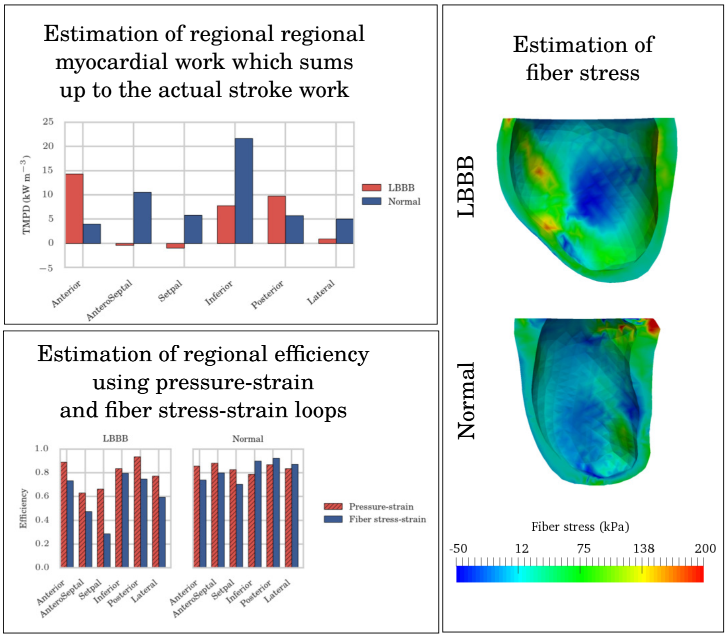

Figure 1.19: Summary figure for paper 4

meet the body's demand. Therefore a regional measure of work would be helpful in assessment of patients with regional dysfunction, and preferable we would have a regional meausure that summed up to the actual stroke work. The area of the pressure-strain loops, where strain here refers to as regional longitudinal strain, has been proposed as a meausure regional myocardial work, and indices based on these work calculations have shown to be a good predictor of response to cardiac resynchronization therapy, a treatment given to patients with regional dysfunction.

To check the validity of these work calculations we estimate work using well known laws from continuum mechanics in a personalized cardiac mechanics model, similar to the models in the previous papers. These work calculations are compared to estimates using the pressure-strain loops approach, and to the "gold-standard" PV area. Our estimates of global mechanical work are in good agreements with estimated PV area, while the pressure-strain loops quantitatively underestimates the total mechanical work. However, relative measures of regional efficiency seems to be independent of how work is computed, and yields the same results in terms of assesment of regional dysfunction. Our finding therefore suggest that regional myocardial work can be assessed using patient-specific finite element modeling, while regional dysfunction in terms of indices of efficiency are independent of how work is computed.

In this study we also perform a convergence analysis of the algorithm for determining the unloaded, zero-pressure geometry as well as the algorithm for joint estimation of material parameters and unloaded geometry.

Other contributions

Along with the research articles presented in this thesis, other types of contributions in terms of talks, posters and software has been made during the writing of this thesis. These contributions are listed below.

Talks

- Henrik Finsberg, Gabriel Balaban, Joakim Sundnes, Hans Henrik Odland, Marie Rognes, and Samuel T. Wall. “Patient Constrained Ventricular Stress Mapping”, Conference Presentation at MALT 2015, Lugano, Switzerland (2015).

- Henrik Finsberg, Gabriel Balaban, Joakim Sundnes, Marie Rognes, and Samuel T. Wall. “Personalization of a Cardiac Computational Model using Clinical Measurements”, Conference Presentation at 28th Nordic Seminar on Computational Mechanics. Vol. 28. Tallin, Estonia, (2015).

- Henrik Finsberg, Gabriel Balaban, Joakim Sundnes, Marie Rognes, and Samuel T. Wall. “Optimization of a Spatially Varying Cardiac Contraction parameter using the Adjoint Method”, Conference Presentation at FEniCS 16, Oslo, Norway,(2016).

- Henrik Finsberg, Gabriel Balaban, Joakim Sundnes, Hans Henrik Odland, Marie Rognes, and Samuel T. Wall. “Personalized Cardiac Mechanical Model using a High Resolution Contraction Field ”, Conference Presentation at VPH16 Translating VPH to the Clinic, Amsterdam, Netherlands (2016).

- Henrik Finsberg, John Aalen,Camilla K. Larsen, Espen Remme, Joakim Sundnes, Otto A. Smiseth, and Samuel T. Wall. “Assessment of regional myocardial work via through adjoint-based data assimilation. ”, Conference Presentation at the International Conference on Computational Science and Enfineering, Oslo, Norway (2016).

Posters

- Henrik Finsberg, Gabriel Balaban, Joakim Sundnes, Marie Rognes, and Samuel T. Wall. “Patient Specific Modeling of Cardiac Mechanics using the

Active Strain Formulation ”, Geilo Winter School, Geilo, Norway, (2016).

- Henrik Finsberg, Ce Xi, J. Tan, L. Zhong, LC Lee, Joakim Sundnes, and Samuel T. Wall. “Mechanical Analysis of Pulmonary Hypertension via Adjoint based Data Assimilation of a Finite Element Model ”, Summer Biomechanics, Bioengineering, and Biotransport Conference, Tucson, AZ, (2017).

Software

- Pulse-Adjoint, FEniCS-based cardiac mechanics solver and data assimilator, source: https://bitbucket.org/finsberg/pulse_adjoint
- Mesh-Toolbox, Toolbox for generating FEniCS meshes from 4D Echo, source: https://bitbucket.org/finsberg/mesh_generation

Closing remarks and future directions

Although we have shown that the techniques developed in this thesis are powerful, and opens up new possibilities in terms of patient-specific mechanical simulations, many questions still have to be answered before we can fully embrace the output of such simulations.

First of all, is should be clear that *the quality of biomarkers you can extract from a data-driven model cannot be any better than the data used as input to the model*. A typical saying is that garbage in = garbage out, meaning that if the data you use to constrain the model is noisy, then you will also fit this noise if you allow for enough degree of freedom. Regularization techniques (Section 1.4.5) provides a way to attack this problem, but it is not clear what is the best approach.

A rule of thump is that *the spatial resolution of the parameters should be reflected in the spatial resolution of the observations*. This means that if one is trying to fit data that are spatially resolved at some level, then choosing parameters that are resolved at a finer level should be done with caution. Regarding both paper 1, 2 and 4 we see that the spatial resolution chosen was at a much finer level than the input data. In this case, regularization techniques were used to restrict the parameter space, by assuming that the solution we seek had specific properties, e.g smoothness.

Regarding the mechanical modeling of the heart, *choosing appropriate boundary conditions* that reflect the reality has been an issue during the work of this thesis, and several different choices have been made. Moreover, *accounting for the orthotropic as well as the visco-elastic behavior of the myocardium* is something that should be investigated in future studies. Accounting for an orthotropic behavior would acquire more parameters to be estimated, which would thus require more input data. In this thesis we have also not fully explored the *spatial resolution of the material parameters*, and it should be investigated whether it is possible to relate locally estimated tissue stiffness to e.g myocardial infarction.

Finally, when estimating high dimensional parameters, a natural question concerning uniqueness of these estimates arises. It is obvious that if one allows for enough degree of freedom in the parameter space, then it is possible to fit almost any type of data. Therefore *more work on ensuring identifiability* of these estimates should be done. If the output of such models should have any clinical utility, then uniqueness of the estimated parameters is absolutely pivotal. Moreover, *validation* of these model is what matter most in terms of translating such computational models into the clinic.

Bibliography

[1] Eugene L Allgower and Kurt Georg. *Introduction to numerical continuation methods*. SIAM, 2003.

[2] Martin S Alnæs, Anders Logg, Kristian B Ølgaard, Marie E Rognes, and Garth N Wells. Unified form language: A domain-specific language for weak formulations of partial differential equations. *ACM Transactions on Mathematical Software (TOMS)*, 40(2):9, 2014.

[3] Martin Sandve Alnæs, Anders Logg, and Kent-Andre Mardal. Ufc: a finite element code generation interface. *Automated Solution of Differential Equations by the Finite Element Method*, pages 283–302, 2012.

[4] D Ambrosi and S Pezzuto. Active stress vs. active strain in mechanobiology: constitutive issues. *Journal of Elasticity*, 107(2):199–212, 2012.

[5] John M Ball. Convexity conditions and existence theorems in nonlinear elasticity. *Archive for rational mechanics and Analysis*, 63(4):337–403, 1976.

[6] Peter J Basser, James Mattiello, and Denis LeBihan. Mr diffusion tensor spectroscopy and imaging. *Biophysical journal*, 66(1):259–267, 1994.

[7] JD Bayer, RC Blake, G Plank, and NA Trayanova. A novel rule-based algorithm for assigning myocardial fiber orientation to computational heart models. *Annals of biomedical engineering*, 40(10):2243–2254, 2012.

[8] Joris Bols, Joris Degroote, Bram Trachet, Benedict Verhegghe, Patrick Segers, and Jan Vierendeels. A computational method to assess the in vivo stresses and unloaded configuration of patient-specific blood vessels. *Journal of computational and Applied mathematics*, 246:10–17, 2013.

[9] Svein Brekke, Stein I Rabben, Asbjørn Støylen, Asbjørn Haugen, Geir U Haugen, Erik N Steen, and Hans Torp. Volume stitching in three-dimensional echocardiography: distortion analysis and extension to real time. *Ultrasound in medicine & biology*, 33(5):782–796, 2007.

[10] David C Brock and Gordon E Moore. *Understanding Moore's law: four decades of innovation*. Chemical Heritage Foundation, 2006.

[11] Matthieu Caruel, Radomir Chabiniok, Philippe Moireau, Yves Lecarpentier, and Dominique Chapelle. Dimensional reductions of a cardiac model for effective validation and calibration. *Biomechanics and modeling in mechanobiology*, 13(4):897–914, 2014.

[12] Manuel D Cerqueira, Neil J Weissman, Vasken Dilsizian, Alice K Jacobs, Sanjiv Kaul, Warren K Laskey, Dudley J Pennell, John A Rumberger, Thomas Ryan, Mario S Verani, et al. Standardized myocardial segmentation and nomenclature for tomographic imaging of the heart a statement for healthcare professionals from the cardiac imaging committee of the council on clinical cardiology of the american heart association. *Circulation*, 105(4):539–542, 2002.

[13] Radomir Chabiniok, Vicky Y Wang, Myrianthi Hadjicharalambous, Liya Asner, Jack Lee, Maxime Sermesant, Ellen Kuhl, Alistair A Young, Philippe Moireau, Martyn P Nash, et al. Multiphysics and multiscale modelling, data–model fusion and integration of organ physiology in the clinic: ventricular cardiac mechanics. *Interface focus*, 6(2):20150083, 2016.

[14] Dominique Chapelle and Klaus-Jürgen Bathe. The inf-sup test. *Computers & structures*, 47(4-5):537–545, 1993.

[15] Dominique Chapelle, Marc Fragu, Vivien Mallet, and Philippe Moireau. Fundamental principles of data assimilation underlying the verdandi library: applications to biophysical model personalization within euheart. *Medical & biological engineering & computing*, 51(11):1221–1233, 2013.

[16] John GF Cleland, Jean-Claude Daubert, Erland Erdmann, Nick Freemantle, Daniel Gras, Lukas Kappenberger, and Luigi Tavazzi. The effect of cardiac resynchronization on morbidity and mortality in heart failure. *New England Journal of Medicine*, 352(15):1539–1549, 2005.

[17] Kevin D Costa, Jeffrey W Holmes, and Andrew D McCulloch. Modelling cardiac mechanical properties in three dimensions. *Philosophical Transactions of the Royal Society of London A: Mathematical, Physical and Engineering Sciences*, 359(1783):1233–1250, 2001.

[18] Jean-Claude Daubert, Leslie Saxon, Philip B Adamson, Angelo Auricchio, Ronald D Berger, John F Beshai, Ole Breithard, Michele Brignole, John Cleland, David B DeLurgio, et al. 2012 ehra/hrs expert consensus statement

on cardiac resynchronization therapy in heart failure: implant and follow-up recommendations and management. *Heart rhythm*, 9(9):1524–1576, 2012.

[19] Kalyanmoy Deb, Karthik Sindhya, and Jussi Hakanen. Multi-objective optimization. In *Decision Sciences: Theory and Practice*, pages 145–184. CRC Press, 2016.

[20] Socrates Dokos, Bruce H Smaill, Alistair A Young, and Ian J LeGrice. Shear properties of passive ventricular myocardium. *American Journal of Physiology-Heart and Circulatory Physiology*, 283(6):H2650–H2659, 2002.

[21] Patrick E Farrell. Multiple local minima of pde-constrained optimisation problems via deflation. Technical report, Unspecified, 2015.

[22] Patrick E Farrell, David A Ham, Simon W Funke, and Marie E Rognes. Automated derivation of the adjoint of high-level transient finite element programs. *SIAM Journal on Scientific Computing*, 35(4):C369–C393, 2013.

[23] Thomas Fritz, Christian Wieners, Gunnar Seemann, Henning Steen, and Olaf Dössel. Simulation of the contraction of the ventricles in a human heart model including atria and pericardium. *Biomechanics and modeling in mechanobiology*, 13(3):627–641, 2014.

[24] Michael W Gee, Ch Förster, and WA Wall. A computational strategy for prestressing patient-specific biomechanical problems under finite deformation. *International Journal for Numerical Methods in Biomedical Engineering*, 26(1):52–72, 2010.

[25] Christophe Geuzaine and Jean-François Remacle. Gmsh: A 3-d finite element mesh generator with built-in pre-and post-processing facilities. *International Journal for Numerical Methods in Engineering*, 79(11):1309–1331, 2009.

[26] Giulia Giantesio, Alessandro Musesti, and Davide Riccobelli. A comparison between active strain and active stress in transversely isotropic hyperelastic materials. *arXiv preprint arXiv:1709.04977*, 2017.

[27] A Goriely. Five ways to model active processes in elastic solids: active forces, active stresses, active strains, active fibers, and active metrics. *Mechanics Research Communications*, 2017.

[28] Phillip Gould, Dhanjoo Ghista, Lawrence Brombolich, and Israel Mirsky. In vivo stresses in the human left ventricular wall: analysis accounting for the irregular 3-dimensional geometry and comparison with idealised geometry analyses. *Journal of biomechanics*, 5(5):521IN13523–522539, 1972.

[29] Sanjay Govindjee and Paul A Mihalic. Computational methods for inverse finite elastostatics. *Computer Methods in Applied Mechanics and Engineering*, 136(1):47–57, 1996.

[30] Julius M Guccione, Andrew D McCulloch, LK Waldman, et al. Passive material properties of intact ventricular myocardium determined from a cylindrical model. *J Biomech Eng*, 113(1):42–55, 1991.

[31] Osman Gültekin, Gerhard Sommer, and Gerhard A Holzapfel. An orthotropic viscoelastic model for the passive myocardium: continuum basis and numerical treatment. *Computer methods in biomechanics and biomedical engineering*, 19(15):1647–1664, 2016.

[32] Myrianthi Hadjicharalambous, Radomir Chabiniok, Liya Asner, Eva Sammut, James Wong, Gerald Carr-White, Jack Lee, Reza Razavi, Nicolas Smith, and David Nordsletten. Analysis of passive cardiac constitutive laws for parameter estimation using 3d tagged mri. *Biomechanics and modeling in mechanobiology*, 14(4):807–828, 2015.

[33] Robert M Heethaar, YC Pao, and Erik L Ritman. Computer aspects of three-dimensional finite element analysis of stresses and strains in the intact heart. *Computers and Biomedical Research*, 10(3):271–285, 1977.

[34] Andreas Heimdal. 4d strain: advanced research application for quantitative echocardiography. *United Kingdom: GE Healthcare*, 2011.

[35] Gerhard A Holzapfel. *Nonlinear solid mechanics*, volume 24. Wiley Chichester, 2000.

[36] Gerhard A Holzapfel and Ray W Ogden. Constitutive modelling of passive myocardium: a structurally based framework for material characterization. *Philosophical Transactions of the Royal Society of London A: Mathematical, Physical and Engineering Sciences*, 367(1902):3445–3475, 2009.

[37] RM Huisman, P Sipkema, N Westerhof, and G Elzinga. Comparison of models used to calculate left ventricular wall force. *Medical and Biological Engineering and Computing*, 18(2):133–144, 1980.

[38] Peter Hunter, Peter V Coveney, Bernard de Bono, Vanessa Diaz, John Fenner, Alejandro F Frangi, Peter Harris, Rod Hose, Peter Kohl, Pat Lawford, et al. A vision and strategy for the virtual physiological human in 2010 and beyond. *Philosophical Transactions of the Royal Society of London A: Mathematical, Physical and Engineering Sciences*, 368(1920):2595–2614, 2010.

[39] Peter J Hunter and Bruce H Smaill. The analysis of cardiac function: a continuum approach. *Progress in biophysics and molecular biology*, 52(2):101–164, 1988.

[40] PJ Hunter, AD McCulloch, and HEDJ Ter Keurs. Modelling the mechanical properties of cardiac muscle. *Progress in biophysics and molecular biology*, 69(2):289–331, 1998.

[41] PJ Hunter, JS Wayne, LK Waldman, JM Guccione, and AD McCulloch. Kd costa. 1996.

[42] Arnold M Katz. *Physiology of the Heart*. Lippincott Williams & Wilkins, 2010.

[43] Stefan Klotz, Ilan Hay, Marc L Dickstein, Geng-Hua Yi, Jie Wang, Mathew S Maurer, David A Kass, and Daniel Burkhoff. Single-beat estimation of end-diastolic pressure-volume relationship: a novel method with potential for noninvasive application. *American Journal of Physiology-Heart and Circulatory Physiology*, 291(1):H403–H412, 2006.

[44] Pablo Lamata, Ramón Casero, Valentina Carapella, Steve A Niederer, Martin J Bishop, Jürgen E Schneider, Peter Kohl, and Vicente Grau. Images as drivers of progress in cardiac computational modelling. *Progress in biophysics and molecular biology*, 115(2):198–212, 2014.

[45] Sander Land, Viatcheslav Gurev, Sander Arens, Christoph M Augustin, Lukas Baron, Robert Blake, Chris Bradley, Sebastian Castro, Andrew Crozier, Marco Favino, et al. Verification of cardiac mechanics software: benchmark problems and solutions for testing active and passive material

behaviour. In *Proc. R. Soc. A*, volume 471, page 20150641. The Royal Society, 2015.

[46] Patrick Le Tallec. Existence and approximation results for nonlinear mixed problems: application to incompressible finite elasticity. *Numerische Mathematik*, 38(3):365–382, 1982.

[47] Ian J LeGrice, BH Smaill, LZ Chai, SG Edgar, JB Gavin, and Peter J Hunter. Laminar structure of the heart: ventricular myocyte arrangement and connective tissue architecture in the dog. *American Journal of Physiology-Heart and Circulatory Physiology*, 269(2):H571–H582, 1995.

[48] DHS Lin and FCP Yin. A multiaxial constitutive law for iviammalian left ventricular myocardium in steady-state barium contracture or tetanus. 1998.

[49] I Liu et al. On representations of anisotropic invariants. *International Journal of Engineering Science*, 20(10):1099–1109, 1982.

[50] Anders Logg, Kent-Andre Mardal, and Garth Wells. *Automated solution of differential equations by the finite element method: The FEniCS book*, volume 84. Springer Science & Business Media, 2012.

[51] Anders Logg, Kristian B Ølgaard, Marie E Rognes, and Garth N Wells. Ffc: the fenics form compiler. *Automated Solution of Differential Equations by the Finite Element Method*, pages 227–238, 2012.

[52] Anders Logg, Garth N Wells, and Johan Hake. Dolfin: A c++/python finite element library. *Automated Solution of Differential Equations by the Finite Element Method*, pages 173–225, 2012.

[53] Augustus Edward Hough Love. *A treatise on the mathematical theory of elasticity*. Cambridge university press, 2013.

[54] Jerrold E Marsden and Thomas JR Hughes. *Mathematical foundations of elasticity*. Courier Corporation, 1994.

[55] Samuel E Moskowitz. Effects of inertia and viscoelasticity in late rapid filling of the left ventricle. *Journal of biomechanics*, 14(6):443–445, 1981.

[56] Martyn P Nash and Peter J Hunter. Computational mechanics of the heart. *Journal of elasticity and the physical science of solids*, 61(1-3):113–141, 2000.

[57] Martyn P Nash and Alexander V Panfilov. Electromechanical model of excitable tissue to study reentrant cardiac arrhythmias. *Progress in biophysics and molecular biology*, 85(2):501–522, 2004.

[58] Amir Nikou, Shauna M Dorsey, Jeremy R McGarvey, Joseph H Gorman III, Jason A Burdick, James J Pilla, Robert C Gorman, and Jonathan F Wenk. Effects of using the unloaded configuration in predicting the in vivo diastolic properties of the heart. *Computer methods in biomechanics and biomedical engineering*, 19(16):1714–1720, 2016.

[59] Denis Noble. Modeling the heart–from genes to cells to the whole organ. *Science*, 295(5560):1678–1682, 2002.

[60] Arnab Palit, Pasquale Franciosa, Sunil K Bhudia, Theodoros N Arvanitis, Glen A Turley, and Mark A Williams. Passive diastolic modelling of human ventricles: effects of base movement and geometrical heterogeneity. *Journal of Biomechanics*, 2016.

[61] Pras Pathmanathan, SJ Chapman, DJ Gavaghan, and JP Whiteley. Cardiac electromechanics: the effect of contraction model on the mathematical problem and accuracy of the numerical scheme. *Quaterly Journal of Mechanics and Applied Mathematics*, 2010.

[62] Jean-Marc Peyrat, Maxime Sermesant, Xavier Pennec, Hervé Delingette, Chenyang Xu, Elliot McVeigh, and Nicholas Ayache. Towards a statistical atlas of cardiac fiber structure. *Medical Image Computing and Computer-Assisted Intervention–MICCAI 2006*, pages 297–304, 2006.

[63] Simone Pezzuto. *Mechanics of the heart: constitutive issues and numerical experiments*. PhD thesis, Italy, 2013.

[64] Mark Potse, Bruno Dubé, Jacques Richer, Alain Vinet, and Ramesh M Gulrajani. A comparison of monodomain and bidomain reaction-diffusion models for action potential propagation in the human heart. *IEEE Transactions on Biomedical Engineering*, 53(12):2425–2435, 2006.

[65] Stein Inge Rabben. Technical principles of transthoracic three-dimensional echocardiography. In *Textbook of Real-Time Three Dimensional Echocardiography*, pages 9–24. Springer, 2010.

[66] ML Raghavan, Baoshun Ma, and Mark F Fillinger. Non-invasive determination of zero-pressure geometry of arterial aneurysms. *Annals of biomedical engineering*, 34(9):1414–1419, 2006.

[67] Damien Rohmer, Arkadiusz Sitek, and Grant T Gullberg. Reconstruction and visualization of fiber and laminar structure in the normal human heart from ex vivo diffusion tensor magnetic resonance imaging (dtmri) data. *Investigative radiology*, 42(11):777–789, 2007.

[68] Kevin L Sack, Neil H Davies, Julius M Guccione, and Thomas Franz. Personalised computational cardiology: Patient-specific modelling in cardiac mechanics and biomaterial injection therapies for myocardial infarction. *Heart failure reviews*, 21(6):815–826, 2016.

[69] Kiichi Sagawa, Hiroyuki Suga, Artin A Shoukas, and Kenneth M Bakalar. End-systolic pressure/volume ratio: a new index of ventricular contractility. *The American journal of cardiology*, 40(5):748–753, 1977.

[70] Harold Sandler and Harold T Dodge. Left ventricular tension and stress in man. *Circulation Research*, 13(2):91–104, 1963.

[71] Hideaki Senzaki, Chen-Huan Chen, and David A Kass. Single-beat estimation of end-systolic pressure-volume relation in humans. *Circulation*, 94(10):2497–2506, 1996.

[72] Daniel D Streeter, Henry M Spotnitz, Dali P Patel, John Ross, and Edmund H Sonnenblick. Fiber orientation in the canine left ventricle during diastole and systole. *Circulation research*, 24(3):339–347, 1969.

[73] Larry A Taber and Renato Perucchio. Modeling heart development. *Journal of elasticity and the physical science of solids*, 61(1-3):165–197, 2000.

[74] Ronald J Tallarida, Ben F Rusy, and Michael H Loughnane. Left ventricular wall acceleration and the law of laplace. *Cardiovascular research*, 4(2):217–223, 1970.

[75] Cedric Taylor and P Hood. A numerical solution of the navier-stokes equations using the finite element technique. *Computers & Fluids*, 1(1):73–100, 1973.

[76] Nicolas Toussaint, Christian T Stoeck, Tobias Schaeffter, Sebastian Kozerke, Maxime Sermesant, and Philip G Batchelor. In vivo human cardiac fibre architecture estimation using shape-based diffusion tensor processing. *Medical image analysis*, 17(8):1243–1255, 2013.

[77] Fijoy Vadakkumpadan, Viatcheslav Gurev, Jason Constantino, Hermenegild Arevalo, and Natalia Trayanova. Modeling of whole-heart electrophysiology and mechanics: toward patient-specific simulations. In *Patient-Specific Modeling of the Cardiovascular System*, pages 145–165. Springer, 2010.

[78] C-C Wang. A new representation theorem for isotropic functions: An answer to professor gf smith's criticism of my papers on representations for isotropic functions. *Archive for Rational Mechanics and Analysis*, 36(3):166–197, 1970.

[79] Jeffrey A Weiss, Bradley N Maker, and Sanjay Govindjee. Finite element implementation of incompressible, transversely isotropic hyperelasticity. *Computer methods in applied mechanics and engineering*, 135(1-2):107–128, 1996.

[80] Alan YK Wong and PM Rautaharju. Stress distribution within the left ventricular wall approximated as a thick ellipsoidal shell. *American heart journal*, 75(5):649–662, 1968.

[81] Robert H Woods. A few applications of a physical theorem to membranes in the human body in a state of tension. *Transactions of the Royal Academy of Medicine in Ireland*, 10(1):417–427, 1892.

[82] Group Members Writing, D Mozaffarian, EJ Benjamin, AS Go, DK Arnett, MJ Blaha, M Cushman, SR Das, S de Ferranti, JP Després, et al. Heart disease and stroke statistics-2016 update: A report from the american heart association. *Circulation*, 133(4):e38, 2016.

[83] FC Yin, CC Chan, and Robert M Judd. Compressibility of perfused passive myocardium. *American Journal of Physiology-Heart and Circulatory Physiology*, 271(5):H1864–H1870, 1996.

[84] Zeyun Yu, Michael J Holst, Yuhui Cheng, and J Andrew McCammon. Feature-preserving adaptive mesh generation for molecular shape modeling and simulation. *Journal of Molecular Graphics and Modelling*, 26(8):1370–1380, 2008.

Paper 1

High Resolution Data Assimilation of Cardiac Mechanics

High Resolution Data Assimilation of Cardiac Mechanics

Gabriel Balaban[1,2,5], Henrik Finsberg[1,2,5*], Hans Henrik Odland[4,5,7], M. E. Rognes[1,3], Stian Ross[4,5], Joakim Sundnes[1,2,5], and Samuel Wall[1,5,6]

1. Simula Research Laboratory, Lysaker, Norway
2. Department of Informatics, University of Oslo, Oslo, Norway
3. Department of Mathematics, University of Oslo, Oslo, Norway
4. Faculty of Medicine, University of Oslo, Oslo, Norway
5. Center for Cardiological Innovation, Oslo, Norway
6. Department of Mathematical Science and Technology, NMBU, Ås, Norway
7. Department of Pediatrics, Oslo University Hospital, Oslo, Norway

Abstract

Computational models of cardiac mechanics, personalized to a patient, offer access to mechanical information above and beyond direct medical imaging. Additionally, such models can be used to optimize and plan therapies in-silico, thereby reducing risks and improving patient outcome. Model personalization has traditionally been achieved by data assimilation, which is the tuning or optimization of model parameters to match patient observations. Current data assimilation procedures for cardiac mechanics are limited in their ability to efficiently handle high dimensional parameters. This restricts parameter spatial resolution, and thereby the ability of a personalized model to account for heterogeneities that are often present in a diseased or injured heart. In this paper we address this limitation by proposing an adjoint-gradient based data assimilation method that can efficiently handle high-dimensional parameters. We test this procedure on a synthetic data set, and provide a clinical example with a dyssynchronous left ventricle with highly irregular motion. Our results show that the method efficiently handles a high dimensional optimization parameter, and produces an excellent agreement for personalized models to both synthetic and clinical data.

---

[*] Both of these authors contributed equally to this work.

Introduction

Computational models of cardiac mechanics, personalized to the level of the individual through the use of clinical imaging, have potential to be a powerful aid in the diagnosis and treatment of cardiac disease. By relating image-based data to fundamental physical processes, models can give additional insight into the function or dysfunction of the individual's heart, beyond what can be directly measured or observed in the images. This is becoming more important as the resolution and accuracy of clinical imaging continues to improve. This increasingly detailed data combined with biophysical models has promise in analysis of regionally and temporally resolved differences in the mechanics of the heart, important in diseases such as heart failure and the application of cardiac resynchronization therapy.

A key step in making these clinically useful cardiac mechanics models is proper data assimilation from patient observations into a fit model. This involves the optimization, or tuning, of individual model parameters in order to make the model match the observations of the patient's heart. Over the last decade several data assimilation methods have been developed and proposed for this problem. The earliest studies employed gradient based optimization in order to minimize the discrepancy between model-derived data and clinical observations. The gradients necessary for these optimizations were calculated using direct differentiation [35] or finite difference [2, 14, 40]. More recent efforts include the use of global optimization methods: in particular genetic algorithms [29, 36], a Monte Carlo method [31], subplex algorithm [41], and parameter sweeps [1, 19]. Finally, reduced order unscented Kalman filtering has also been successfully applied as a data assimilation tool for patient-specific model creation [9, 42, 28].

The increasingly large amount of easily obtainable geometric and motion data, however, is a challenge for data assimilation into personalized computational models using the techniques mentioned above. This is as the computational expense scales badly with the number of model parameters to be fit. In the case of the Kalman filtering strategies, at least one extra evaluation of the model is required per additional model parameter to be optimized. The calculation of model-data mismatch gradients by finite difference or direct differentiation suffers from the same limitation. Global methods on the other hand are affected by the curse of dimensionality; that is, a rapid expansion of the space of parameters that must be searched as the number of dimensions increases. For high dimensional problems the run-time needed to carry out a global search can be computationally prohibitive.

In contrast, the calculation of a functional gradient by the adjoint formula is nearly independent of the number of optimization parameters, requiring one forward and one backward adjoint solve of the mathematical model. The forward solve is typically needed to evaluate the functional, and the evaluation of the gradient at the same point requires only an additional backward solve of the adjoint system. Furthermore, this backward solve is always linear, and therefore computationally less expensive than the forward solve if the mathematical model is nonlinear. These methods have been widely explored in model optimization, with adjoint-based data assimilation techniques having previously been employed for cardiac mechanics, specifically using linear elastic models and clinical data [10, 37], and also nonlinears model combined with experimental data [4].

In this work we provide an improved data assimilation pipeline for high resolution optimization, demonstrating the parameterization of mechanical contraction in high spatial resolution driven by 4D echocardiography patient data. This high dimensional optimization problem is efficiently solved using an adjoint gradient based technique, described in detail in our previous work [4]. We demonstrate our method on the pathological case of a dyssynchronous left ventricle, which has complex and irregular motion, as well as on a synthetic case consisting of data generated by our mechanical model. This study is to the best of our knowledge the first to use adjoint-based data assimilation for nonlinear cardiac mechanics with clinical data, and the first to consider the resolution of a parameter at the same scale as the discretization of the cardiac geometry. These are important considerations as better understanding of myocardial properties emerges and the collection of high resolution clinical data continues to expand.

The rest of this paper is organized as follows: In Section 2.2 we present a mathematical model that accounts for the three main drivers of ventricular mechanics; blood pressure, tissue elasticity and muscle contraction. We also describe clinical measurements of a patient suffering from dyssynchrony, and our data assimilation procedure for fitting the model to these measurements. Numerical results are presented in Section 2.3, and discussed in Section 2.4. Finally, we provide some concluding remarks in Section 2.5.

Materials and Methods

Wall motion modelling

In order to estimate the position of the myocardial walls through the cardiac cycle we adopt a continuum mechanics description of cardiac wall motion. In this description we consider a fixed left ventricular reference geometry Ω, with endocardial boundary $\partial\Omega_{\text{endo}}$, and basal boundary $\partial\Omega_{\text{base}}$.

Our fundamental quantity of interest is the vector valued displacement map $\mathbf{u}(\mathbf{X})$, where $\mathbf{X} \in \Omega$. At any given point in time in the cardiac cycle, $\mathbf{u}(\mathbf{X})$ relates the current geometry ω to the reference geometry by

$$\mathbf{X} + \mathbf{u}(\mathbf{X}) = \mathbf{x}, \quad \mathbf{x} \in \omega, \quad \mathbf{X} \in \Omega. \tag{2.1}$$

Assuming that the cardiac walls are in equilibrium, it is possible to determine the value of $\mathbf{u}$ from the principle of virtual work

$$\delta W(\mathbf{u}) = 0, \tag{2.2}$$

which states that the virtual work, $\delta W(\mathbf{u})$, of all forces applied to a mechanical system vanishes in equilibrium. For our ventricular wall motion model, the virtual work $\delta W(\mathbf{u})$, is given by

$$\begin{aligned} \delta W(\mathbf{u}, p) = & \int_\Omega \mathbf{P} : \text{Grad}\ \delta\mathbf{u}\ dV + \int_\Omega (J-1)\delta p + pJ\mathbf{F}^{-T} : \text{Grad}\ \delta\mathbf{u}\ dV \\ & + p_{\text{lv}} \int_{\partial\Omega_{\text{endo}}} J\mathbf{F}^{-T}\mathbf{N} \cdot \delta\mathbf{u}\ dS + \int_{\partial\Omega_{\text{base}}} k\mathbf{u} \cdot \delta\mathbf{u}\ dS. \end{aligned} \tag{2.3}$$

Here we have introduced the hydrostatic pressure p in order to enforce the incompressibility constraint $J = 1$, with $J = \det\mathbf{F} = \det(\text{Grad}\ \mathbf{u} + \mathbf{I})$, and $\mathbf{I}$ being the second order identity tensor. Furthermore, $\mathbf{N}$ denotes the unit outward normal vector, k the constant of a spring that we introduce at the basal boundary, and p_{lv} the intra-ventricular blood pressure. The virtual variables $\delta\mathbf{u}$ and δp are test functions whose values are arbitrary when the system (2.2) is in mechanical equilibrium.

In order to anchor the computational geometry, we fix $\mathbf{u}$ in the longitudinal direction at the base by using a Dirichlet boundary condition. At the epicardial boundary normal forces are set to 0, and so there is no term for this boundary in (2.3).

The internal stresses of our model are given by $\mathbf{P}$, the first Piola-Kirchhoff tensor, which can be calculated as a derivative of a strain energy functional in the case of a hyperelastic material. In our model we employ a reduced version [24, 17, 1, 19] of the Holzapfel-Ogden strain energy law [20],

$$\psi(\mathbf{C}) = \frac{a}{2b}\left(e^{b(I_1(\mathbf{C})-3)} - 1\right) + \frac{a_f}{2b_f}\left(e^{b_f(I_{4f}(\mathbf{C})-1)_+^2} - 1\right), \tag{2.4}$$

which gives the amount of strain energy, ψ, stored per unit volume myocardium undergoing the strain $\mathbf{C} = \mathbf{F}^T\mathbf{F}$. The notation $(\cdot)_+$ refers here to $\max\{\cdot,0\}$. Furthermore the mechanical invariants I_1 and I_{4f} are defined as

$$I_1(\mathbf{C}) = \operatorname{tr}\mathbf{C}, \qquad I_{4f} = \mathbf{f}_0 \cdot \mathbf{C}\mathbf{f}_0, \tag{2.5}$$

with $\mathbf{f}_0$ indicating the local myocardial fiber direction. The material parameters a, a_f, b, b_f are scalar quantities which influence the shape of the stress-strain relationship, and can be adapted to personalize the elastic properties of a myocardial tissue model to a specific patient.

The Lagrange multiplier formulation of incompressibility that we employ enforces its constraint only weakly. This can cause convergence issues in the numerical solution of the work balance equation (2.2). We therefore eliminate volumetric strains from the energy function (2.4) by a simple modification

$$\tilde{\psi}(\mathbf{C}) = \psi(J^{-\frac{2}{3}}\mathbf{C}). \tag{2.6}$$

This modification has been shown to improve the robustness of Newton-Raphson methods applied to incompressible hyperelastic problems [Figure 3C of [25]].

In order to account for muscle contraction we apply the active strain framework [30]. In this framework the amount of muscle fiber shortening is specified by a field γ via a split of the deformation gradient

$$\mathbf{F} = \mathbf{F}_e\mathbf{F}_a(\gamma), \tag{2.7}$$

where $\mathbf{F}_e$ is the elastic part and $\mathbf{F}_a(\gamma)$ the active part of the deformation gradient. For the value of $\mathbf{F}_a(\gamma)$ we adopt a simple relation [17, 11] which satisfies the incompressibility constraint by design and directly relates the amount of active fiber shortening to the value of γ

$$\mathbf{F}_a = (1-\gamma)\mathbf{f}_0 \otimes \mathbf{f}_0 + \frac{1}{\sqrt{1-\gamma}}(\mathbf{I} - \mathbf{f}_0 \otimes \mathbf{f}_0). \tag{2.8}$$

In the case $\gamma = 0$ there is no muscle shortening at all, and the amount of shortening increases with increased γ up to the theoretical limit of $\gamma = 1$. Physiologically, γ models the length change along muscle fibers neglecting elastic effects. This, together with the elastic resistance gives the strength of the muscle contraction.

Muscle contraction is accounted for in terms of virtual work by modifying the first Piola-Kirchhoff stress tensor, so that the strain energy only depends on the elastic part of the deformation

$$\mathbf{P} = \frac{\partial \tilde{\psi}}{\partial \mathbf{F}} = \frac{\partial \tilde{\psi}(\mathbf{C}_e)}{\partial \mathbf{F}} \tag{2.9}$$

with $\mathbf{C}_e = \mathbf{F}_e^T \mathbf{F}_e$.

Given an amount of fiber shortening γ, the value of the elastic parameters a, b, a_f, b_f, the intraventricular blood pressure p_{lv} and the spring constant k, the myocardial wall displacement $\mathbf{u}$ and hydrostatic pressure p can be obtained by solving the principle of virtual work (2.2).

Clinical measurements

Clinical data were obtained at the Oslo University Hospital in the context of the Impact study [22]. Specifically, we consider the case of an 82 year old man in NYHA functional class III systolic heart failure with coronary artery disease, and left bundle branch block. A left bundle branch block normally causes both electrical and mechanical dyssynchrony. In this case the ECG revealed a QRS width of 140 ms and the echocardiographically derived ejection fraction of 30 %.

Prior to cardiac resynchronization therapy implant, the patient had echocardiographic and left ventricular (LV) pressure measurements taken, which are the basis for the clinical data used in this study. Pressure recordings were carried out with an intravascular pressure sensor catheter (Millar micro catheter) that was positioned in the LV via the right femoral artery. Pressure data were obtained automatically and digitized (Powerlab system, AD Instruments) before offline analyses were performed with a low pass filter of 10Hz.

Images of the patient's left ventricle (LV) were captured with 4D echocardiography using a GE Vingmed E9 machine (GE healthcare Vingmed, Honrten, Norway). Speckle tracking motion analysis was carried out with GE's software package EchoPac. Data from 6 beats were combined in EchoPac in order to obtain a single sequence of images for a single heartbeat. Analysis of these images resulted in LV cavity volume measurements as well as regional strain curves defined for a 17 segment delineation of the LV according to the AHA representation [8]. The strain curves were measured in the local left ventricular longitudinal, radial and circumferential directions. Both strains and volumes were measured 34 times throughout the cardiac cycle.

Valvular events were used to synchronize the pressure to the strain and volume data. The timing of the observed valvular events in the images were matched with the observed valvular events in the pressure trace. In the pressure trace, aortic valve opening (AVO) was selected after the steepest increase of the pressure ($\frac{dp}{dt}$ max), and mitral valve closure just before $\frac{dp}{dt}$ max . Aortic valve closure (AVC) was chosen just before the pressure had its largest decrease after AVO, and the mitral valve opening before the pressure dropped down to baseline after AVC. A pressure-volume loop based on the synchronization is displayed in Figure 2.2.

Finally a linear correction of the strain curves was performed in order to eliminate drift; with drift being defined as the value of the strain obtained at the end of the cardiac cycle. Theoretically drift should be zero for a stable cyclical heartbeat. The linear correction enforces the cyclical property.

Ventricular geometry generation

The computational mechanics framework used for our wall motion model, described in Section 2.2.1, requires a reference stress-free geometry from which to define displacements. Such a geometry typically does not exist in-vivo due to the presence of blood pressure on the endocardial walls. Algorithms exist for calculating stress free geometries given a loaded state [7, 15]. However for the sake of simplicity we derive our reference geometry from an echocardiographic image of the LV at the beginning of atrial systole, as the pressure is near minimal at this point, and the ventricular myocardium can be assumed to be relaxed.

From the image at the beginning of atrial systole, triangulated data points for left ventricular endocardial and epicardial surfaces, along with a 17 segment delineation, were extracted using the EchoPac software package. The segment delineation was given on a so called strain mesh, which is a 2-D surface constructed by EchoPac and located approximately in the mid wall of the LV.

We constructed a flat ventricular base by cutting the raw geometry with a plane that was fit via least-squares to the points at the base. After the fitting, the longitudinal position of the cutting plane was adjusted so that the cavity volume of the resulting mesh agreed with the measured volume to a tolerance of 1 ml. Points on the epicardial and endocardial surfaces that lay above the cutting plane were removed.

We employed Gmsh [16] to create a linear tetrahedral volumetric mesh between the endocardial and epicardial surfaces. This mesh had 1262 elements, and is shown in Figure 2.1b. Myocardial fiber orientations were assigned using a rule based method, with a fiber helix angle of 40 degrees on the endocardium rotated clockwise throughout the ventricular wall to -50 degrees on the epicardium [6]. A streamline representation of the local myocardial fibers is displayed in Figure 2.1c.

Finally, the AHA-segments from the strain mesh were transferred onto the volumetric mesh. This was accomplished by computing prolate spherical coordinates for the barycenter of each tetrahedron, and then assigning an AHA-zone to the tetrahedron based on the corresponding prolate spherical coordinate in the strain mesh. AHA-segments on the volumetric mesh are shown in Figure 2.1d.

Parameter Estimation

Now that we have a mathematical description of cardiac motion, along with a personalized computational geometry and target data, we next turn to the problem of personalizing the motion model via the estimation of the elastic parameters and the fiber contraction. As dyssynchrony is a disease which primarily effects the contraction properties of the ventricle, we focus our efforts on contraction modelling and employ a very simple personalization of stiffness properties. That is only the parameter a is optimized to fit the ventricular volumes, and the other elastic parameters are kept fixed at the values ($a_f = 1.685, b = 9.726, b_f = 15.779$), which were obtained from a bi-axial loading experiment [Table 1 row 3 of [20]].

Fiber contraction varies throughout the cardiac cycle, and so we estimate the parameter γ separately at each time measurements were taken. Furthermore, as the contraction of the left ventricle may occur dyssynchronously, we allow for γ to vary in space as well as in time.

Muscle shortening is typically present in the ventricles throughout systole and in early diastole until the muscles fully release their contraction. During the phase of atrial systole we do not expect muscle contraction in the ventricle, and so we set $\gamma = 0$ for this phase. This allows us to estimate elastic properties independently

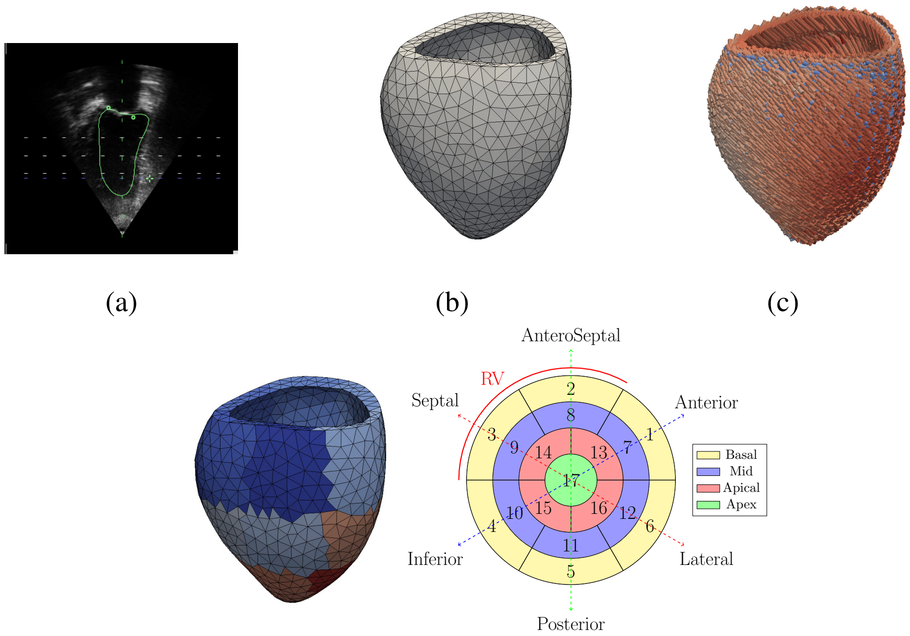
AnteroSeptal
RV
Septal
Anterior
Inferior
Lateral
Posterior
1
2
3
4
5
6
7
8
9
10
11
12
13
14
15
16
17
Basal
Mid
Apical
Apex

(a) (b) (c)

(d) (e)

Figure 2.1: Ventricular geometry generation. Endo and epi-cardial surfaces are marked on 3-D ultrasound images. Figure (2.1a) shows the endocardial marking for a 2-D slice of one such image. Next a computational geometry is generated from epi and endo-cardial surfaces (2.1b), and rule based fibers are assigned (2.1c). Finally AHA segments are assigned to the geometry (2.1d), according to the standardized scheme (2.1e).

of contraction during atrial systole, and then estimate contraction at each point in the rest of the cardiac cycle with the material parameters fixed. In Figure 2.2 we show the pressure-volume loop of the patient under consideration, and highlight the phases where we estimate the contraction and elastic parameters.

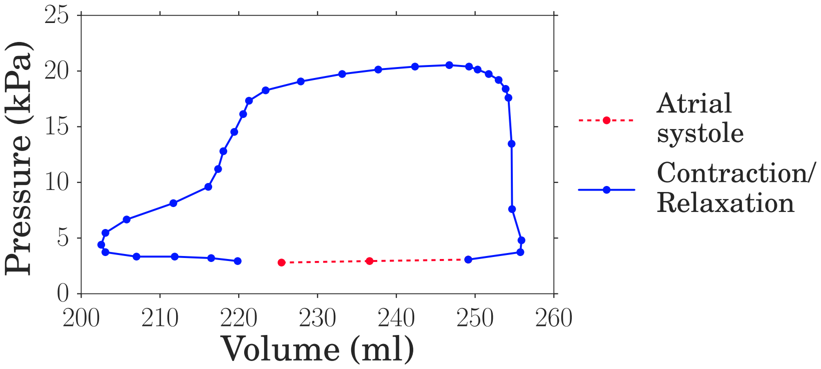

Figure 2.2: Patient pressure-volume relationship for the left ventricle. Measurements in the blue solid line are used to estimate contraction, whereas measurements in the red dashed line are used to estimate elasticity.

Definition of functionals

As described in Section 2.2.2, the data available for our personalization of the wall motion model are pressure, volume and strain measurements throughout the cardiac cycle. The pressure measurements are included in the model as a boundary condition via the virtual work (2.2), and thus our data assimilation only needs to fit the model to the volume and strain measurements. This requires that we define a suitable set of functionals that quantify the model-strain and model-volume mismatches. The personalization of the wall motion model can then be achieved by optimizing the contraction and elastic parameters in order to minimize the total model-data mismatch.

Let i denote the index of an observed cavity volume V^i, or strain ε^i, in the cardiac cycle. Furthermore let $j \in \{1,..,17\}$ be the index of an AHA segment Ω_j, and $k \in \{c,r,l\}$ indicate a direction: circumferential, radial or longitudinal, respectively. Given a measurement point i, we define the model-strain mismatch

$$I^i_{\text{strain}} = \sum_{j=1}^{17} \sum_{k\in\{c,r,l\}} \left(\varepsilon^i_{kj} - \tilde{\varepsilon}^i_{kj}\right)^2, \tag{2.10}$$

for model strain $\tilde{\varepsilon}^i_{kj}$ and measured strain ε^i_{kj}. The speckle tracking software we use provides the measured strain ε^i_{kj}. This strain is regionally averaged and of Lagrangian type. In order to mimic this in our model we define the model strain as

$$\varepsilon_{kj} = \frac{1}{|\Omega_j|} \int_{\Omega_j} \mathbf{e}_k^T \nabla \mathbf{u}\, \mathbf{e}_k \, dx, \tag{2.11}$$

where $\mathbf{e}_k$ denotes a unit direction field and $|\Omega_j|$ the volume of segment j.

Furthermore we also define the model-volume mismatch

$$I^i_{\mathrm{vol}} = \left(\frac{V^i - \tilde{V}^i}{V^i} \right)^2, \tag{2.12}$$

where the model volume is calculated by the formula

$$\tilde{V}^i = -\frac{1}{3} \int_{\partial\Omega_{\mathrm{endo}}} (\mathbf{X} + \mathbf{u}) \cdot J\mathbf{F}^{-T} \mathbf{N} \, dS. \tag{2.13}$$

We note that this method of calculating the model volume depends upon $(\mathbf{X} + \mathbf{u}) \cdot \mathbf{N} = 0$ at the basal plane. These conditions hold in our model as the basal plane is defined with 0 longitudinal coordinate and longitudinal displacements are also set to 0 in this plane.

In order to have a single optimization target to describe the fit to data we combine the strain (2.10) and volume (2.13) mismatches into one single functional

$$I^i_{\mathrm{data}}(\alpha) = \alpha I^i_{\mathrm{vol}} + (1 - \alpha) I^i_{\mathrm{strain}}. \tag{2.14}$$

Here the parameter α controls the relative emphasis of the parameter estimation on volume or strain matching.

In our study we consider a high dimensional representation of γ in order to more accurately capture the details of a dyssynchronous contraction. However this can easily lead to an over-parametrized problem in which many parameter combinations produce the same functional values. In order to further constrain the optimization we introduce a 1st order Tikohonov regularization functional

$$I^i_{\mathrm{smooth}}(\lambda) = \lambda \|\nabla \gamma^i\|^2, \tag{2.15}$$

where $\|\cdot\|$ represents the standard L^2 norm. This functional discriminates between γ parameter sets based on their smoothness. The parameter λ can be adjusted to control the size of the functional and hence the relative emphasis on smoothing.

Parameter estimation as an optimization problem

The elastic parameters of the reduced Holzapfel-Ogden law (2.4) represent the passive elastic properties of the myocardium. We personalize these properties by adjusting the parameter a to match measured left ventricular volumes. Mathematically this problem is formulated as

$$\begin{aligned} \underset{a}{\text{minimize}} \quad & \sum_{i=1}^{N_{\text{AS}}} I^i_{\text{vol}} \\ \text{subject to} \quad & \delta W(p^i_{\text{lv}}, a) = 0 \quad \forall i \ \in \{1, ...N_{AS}\}, \end{aligned} \tag{2.16}$$

where δW is given by (2.3), and $N_{\text{AS}} = 3$ indicates the total number of measurements available in atrial systole.

The contraction field that we seek should fit the data as closely as possible while also being as smooth as possible. In order to achieve this we minimize both the data and smoothness functionals as follows:

$$\begin{aligned} \underset{\gamma}{\text{minimize}} \quad & I^i_{\text{data}}(\alpha) + I^i_{\text{smooth}}(\lambda) \\ \text{subject to} \quad & \delta W(p^i_{\text{lv}}, a, \gamma^i) = 0 \\ & \gamma^i(\mathbf{X}) \in [0,1), \ \mathbf{X} \in \Omega. \end{aligned} \tag{2.17}$$

This problem is solved for every measurement point i not in atrial systole.

The optimization problems (2.16) and (2.17) have two free parameters whose values must be chosen, namely the strain-volume weighing α and the regularization λ. The value of λ can be expected to influence the trade-off between the optimized values of the data functional I^i_{data} and the regularization functional I^i_{smooth}. Similarly α can be expected to influence the trade-off between I^i_{strain} and I^i_{vol}. In our study we choose the values of α and λ by examining their effects on the functionals that they weigh. The choices we made are further described in Section 2.3.3

The spatial resolution of the parameter γ affects the amount of detail that can be captured by the model and simultaneously the number of variables that need to be optimized. We therefore test 3 different resolutions of γ. The lowest resolution, “scalar”, is simply a single global value. The next resolution is “regional”, and consists of a separate value for each of the 17 AHA zones. Finally, the highest resolution we consider is “P1” and consists of a separate value at each of the vertices of the mesh, with a linear interpolation between vertices. Using our ventricular mesh, a P1 resolution of γ has 1262 separate variables.

Implementation of mechanics and optimization solvers

For the numerical solution of the work balance equation (2.2) we employ a Galerkin finite element method with Taylor-Hood tetrahedral elements [21]; that is, a continuous piecewise quadratic representation of the displacement field and a continuous piecewise linear representation of the pressure field.

The software implementation of our finite element method is based on the package FEniCS [27], which automatically generates matrix and vector assembly code from a symbolic representation of the work balance equation (2.2). The resulting nonlinear systems were solved using the PETSc implementation of a Newton trust region algorithm [5], while the inner linear solves were handled by a distributed memory parallel LU solver [26].

To solve the optimization problems (2.16) and (2.17), we apply a sequential quadratic programming algorithm (SQP) [23]. This algorithm requires the derivatives of the function to be optimized, which in our case are the gradients of the mismatch functionals in problems (2.16) and (2.17) with respect to a and γ respectively. These gradients are automatically computed by solving a machine derived adjoint equation via the software framework dolfin-adjoint [12].

In addition to gradients, the SQP algorithm requires evaluations of the mismatch functionals for given values of the control variables, which again relies on the solution of the work balance equation (2.2). In the case of problem (2.17), the control variable is γ, which has a large influence on the solution of (2.2). Numerical solution of (2.2) by Newton's method depends upon having a good initial guess, which in our case are the values of the mechanical state variables, $\mathbf{u}, p$, resulting from the previous solve of (2.2). If the value of γ differs too greatly from one solve to the next the Newton algorithm might fail due to the root of the system being too far away from the initial guess. To avoid this problem we make use of a homotopy procedure that moves from one value of γ to the next in small increments, and solves (2.2) each time the value of γ is changed. This procedure is presented as Algorithm 1 and is similar to the one found in [34].

All algorithms, solvers and relevant data are publicly available online [13].

Algorithm 1 Max Increment Homotopy Newton Solver

```
  Initial Variables
      $\mathbf{u}_{prev}$            Previous displacement field
      $p_{prev}$            Previous tissue hydrostatic pressure field
      $\gamma_{next}$            Desired tissue contraction field
      $\delta\gamma_{max}$           Maximum change in a component per Newton solve
  Set
      $\gamma_0 = \gamma_{prev}$
      $\mathbf{u}_0 = \mathbf{u}_{prev}$
      $p_0 = p_{prev}$
      $M = \left\lceil \frac{\|\gamma_{next} - \gamma_{prev}\|_\infty}{\delta\gamma_{max}} \right\rceil$
      $\delta\gamma = \frac{1}{M}(\gamma_{next} - \gamma_{prev})$

  Use Newton's method M times with fixed increment $\delta\gamma$
  for $i \in \{1...M\}$ do
      $\gamma_i = \gamma_{i-1} + \delta\gamma$
      Initialize Newton solver with $\mathbf{u}_{i-1}, p_{i-1}$
      Solve $\delta W(\mathbf{u}_i, p_i, \gamma_i) = 0$ for $\mathbf{u}_i, p_i$
  Output $\mathbf{u}_i, p_i$
```

Error Estimation

The optimization functionals introduced in Section 2.2.5 are defined separately for each measurement point. For the purposes of evaluating goodness of fit over the entire cardiac cycle we consider metrics that are averaged over measurement points. Furthermore we relate errors to the sizes of the data for ease of interpretation. In the case of the model-volume error we introduce the volume metric

$$\bar{I}_{\mathrm{vol}} = \frac{\|V^i - \tilde{V}^i\|_{\ell^1}}{\|V^i\|_{\ell^1}} \tag{2.18}$$

where the ℓ^1 norm is taken with respect to the measurement point index i. Furthermore we consider two average strain metrics

$$\bar{I}_{\mathrm{strain}} = \frac{1}{51}\sum_{j=1}^{17}\sum_{k\in\{c,r,l\}} \frac{\|\varepsilon^i_{k,j} - \tilde{\varepsilon}^i_{k,j}\|_{\ell^1}}{\|\varepsilon^i_{k,j}\|_{\ell^1}}, \tag{2.19}$$

$$\bar{I}^{\mathrm{relmax}}_{\mathrm{strain}} = \frac{1}{51}\sum_{k\in\{c,r,l\}} \frac{\sum_{j=1}^{17}\|\varepsilon^i_{k,j} - \tilde{\varepsilon}^i_{k,j}\|_{\ell^1}}{\max_j \|\varepsilon^i_{k,j}\|_{\ell^1}}. \tag{2.20}$$

Here N specifies the number of measurement points used in the optimization, and the factor 51 is 17×3, the number of AHA segments times the number of strain measurements per segment. The first metric considers relative differences between norms, whereas the second relates errors norms to the maximum strain norm over all segments. This second metric emphasizes larger features in the strain curves more heavily, and deemphasizes small scale features such as noise.

Similarly to the average data errors introduced above we also introduce a smoothness metric that is averaged across measurement points

$$\bar{I}_{\mathrm{smooth}} = \frac{1}{N}\sum_{i=1}^{N} I^i_{\mathrm{smooth}}, \tag{2.21}$$

and a combined data metric based on the strain and volume metrics

$$\bar{I}_{\mathrm{data}} = \bar{I}_{\mathrm{vol}} + \bar{I}_{\mathrm{strain}}. \tag{2.22}$$

Finally we also define an error metric for a synthetic data test of the contraction optimization (2.17). In this test a contraction field γ_{ground} is chosen and synthetic data is generated from the mechanics model. This data is then used to calculate a reproduction of the contraction γ_{repr}. In order to compare the ground truth and reproduced contraction fields we employ a relative L^2 norm

$$\|\varepsilon_\gamma\|_{\text{avg}} = \frac{1}{N}\sum_{i=1}^{N} \frac{\|\gamma^i_{\text{repr}} - \gamma^i_{\text{ground}}\|_{L^2}}{\|\gamma^i_{\text{ground}}\|_{L^2}}. \tag{2.23}$$

Numerical Experiments

In this section we present the results of our numerical experiments. We first estimate the parameter a using volume measurements in atrial systole. We then test the estimation of contraction γ using synthetic data generated by the wall motion model. This gives an idea of how well the algorithm can perform under idealized circumstances. Next, we carry out the contraction estimation using the clinical strain and volume data. Finally, we consider lower resolution representations of γ, and compare the resolutions based on computational expense and data matching capability.

In all of the experiments below, optimizations were terminated if the difference between the value of the mismatch in the current and previous iteration was less than 10^{-9} for the passive material parameter optimization and 10^{-6} for the contraction parameter optimization or if the SQP algorithm was not able to further reduce the mismatch value. In the active parameter optimization the SQP algorithm was initialized with the value of γ from the previous measurement point in the cardiac cycle.

In order to obtain convergence of Newton's method for the solution of the virtual work equation (2.2), we set $\delta\gamma_{max} = 0.02$ in the homotopy Newton solver (Algorithm 1), and limit γ to the interval $[0, 0.9]$. In the cases that Newton's method did not converge, $\delta\gamma_{max}$ was halved until convergence was obtained.

Strains were calculated with respect to the measurement point defined as start of atrial systole, as the reference geometry taken from the image corresponding to this point was assumed to be stress and strain free. Similarly, pressures for the clinical data were adjusted downward by the pressure measured at the start of atrial systole, 2.8 kPa, so that the adjusted start of atrial systole pressure was 0, and therefore compatible with the stress free assumption.

The value of the basal spring-constant was set to $k = 1.0$ kPa. This allowed for some motion in the basal plane, and was shown in a sensitivity analysis (see Appendix 2.7.2) to give optimal γ values whose spatial average is close to that obtained with a completely fixed boundary.

Estimation of elastic parameter a

An estimate of the parameter a was obtained by minimizing the mismatch between model derived and clinically measured volumes in atrial systole, as described in (2.16). The optimal a value obtained was 0.435, with goodness of fit $\bar{I}_{\text{vol}} = 0.0035$. The same optimal a value was obtained from 8 randomly chosen starting points between 0 and 45.

Synthetic dataset creation

In order to evaluate the performance of our contraction estimation method (2.17) under idealized conditions we have performed synthetic data tests. The data for these tests was constructed by solving the virtual work equation (2.2) for a given set of elastic parameters (a, a_f, b, b_f), contraction γ, and cavity pressures. The a parameter was set to 0.435, as obtained previously by fitting the model to the patient atrial systolic volume data. The other three elastic parameters were fixed to the values mentioned in Section 2.2.4. The contraction γ was chosen to be a wave with Gaussian shape and P1 resolution traveling along the longitudinal axis.

Eight points of measurement were used in the synthetic tests. This was fewer than the number of in-vivo measurement points, which allowed for faster computations. The pressure values that were chosen for the synthetic measurement points can be seen in Figure 2.5. These pressures start at 0, increase to the maximum atrial systole pressure that was measured in-vivo and then decrease linearly back to 0.

For the synthetic strain data we considered three different cases. The first case consisted of the displacement gradient tensor defined over the entire ventricular geometry. Next we considered regionally averaged values of the diagonal components of the displacement gradient. The regional averaging mimics the strain curves generated by the speckle tracking software. Finally we consider 30 noisy realizations of the regional strain curves. The noise that was added to these curves was estimated from the drift values of the in-vivo strain and is described in Appendix 2.7.5.

Choice of functional weights α and λ

The optimization functional weights α and λ were chosen based on trial optimizations using the synthetic and in-vivo datasets. The strains in the synthetic data were regionally averaged and noisy. In these trials we first set $\lambda = 0$ and tested α values ranging from 0 to 1.0 in increments of 0.1, in addition to the values 0.95, 0.99, 0.999, and 0.9999. For each level of α we recorded the values of the fit metrics, $\bar{I}_{\text{vol}}$ and $\bar{I}_{\text{strain}}$, and plotted them against each other (Figure 2.3). Based on the plot we chose $\alpha = 0.95$ as this value gave a good balance between volume and strain matching. With the value of α fixed to 0.95 we tested λ from 10^{-6} to 100.0 in increasing powers of 10. The effect of the choice of λ on the smoothness and data functionals is shown in Figure 2.3. Based on this plot we selected points that gave near optimal fit values with a high level of smoothness. These points were $\lambda = 1.0$ for the synthetic case and $\lambda = 0.01$ for the patient case.

Contraction estimation with synthetic data

Using the synthetic datasets described in Section 2.3.2 as a target we calculated optimized contraction fields. All elastic parameters were kept fixed throughout the optimization so that the test was restricted to the contraction field. We quantified the error in the reproduction of γ using P1 resolution for the three cases of strain. Errors in the relative norm, $||\varepsilon_\gamma||_{\text{avg}}$, were 0.033 for the full displacement gradient tensor and 0.227 for the regionally averaged diagonal of the displacement gradient without noise. The average error for the 30 noisy regionally averaged cases was 0.224 with a standard deviation of 0.009. We note that the reproduction error was lowest for the full clean strains, and an order of magnitude higher for the regional clean and regional noisy strains. We also note that the reproduction error using regional clean strains was very close to the average reproduction error from the 30 regional noisy strains. The maximum error for all three cases of strain occured in the apex, and was 0.06, 0.0701, 0.0724 for the full, regional clean and regional noisy cases respectively.

For the case of the full clean strains we have plotted the reconstructed contraction field alongside the ground truth in Figure 2.5. We note that the ground truth and reproduction appear very similar. In order to visualize the effect of the noise in strain on the optimized contraction field we plotted the mean and standard deviation of the 30 synthetic strain curves, and mean and standard deviation of the average of the contraction field resulting from the 30 strain curves. Both of these plots are restricted to the anterior basal segment and are shown in Figure 2.4. We note that the effect of the noise on the average contraction field is minimal.

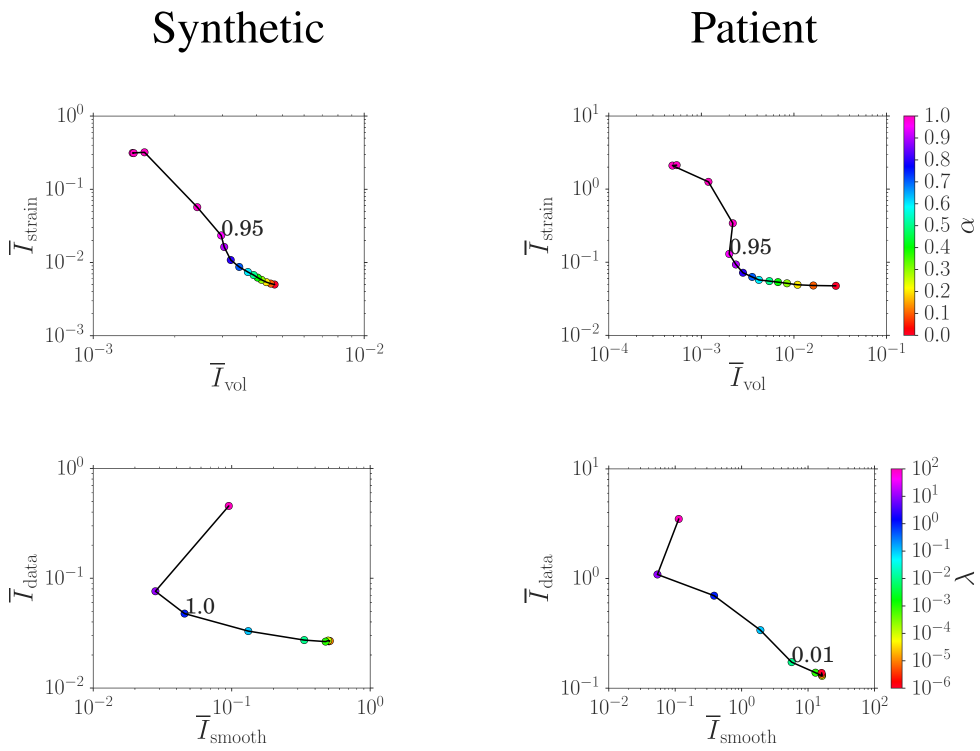

Figure 2.3: Trade-off curves for various α and λ values used in model personalization with synthetic strain data and in-vivo patient data. The synthetic strains are noisy and regionally averaged. The contraction parameter is represented at P1 resolution. Top: optimal strain mismatch (2.20) versus average volume mismatch (2.18) for a range of α values and $\lambda = 0.0$. Bottom: Total data mismatch versus contraction gradient size for a range of λ values and $\alpha = 0.95$.

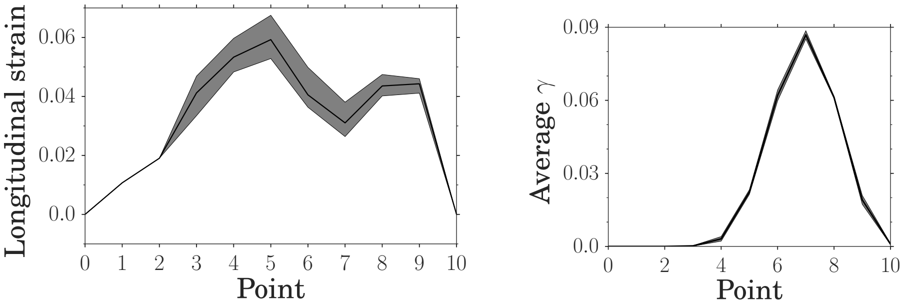

Figure 2.4: On the left are the mean (solid line) and standard deviation (highlighted area) of 30 synthetic longitudinal strain curves in the anterior basal segment corrupted by Gaussian noise. On the right are the mean and standard deviations of γ averaged over the same segment.

Contraction estimation with in-vivo data

Using the in-vivo data described in Section 2.2.2 as a target, we calculated optimized contraction fields at P1 resolution. These contraction fields are shown in Figure 2.8. We note that the value of the contraction varies significantly in space and time. A comparison of the estimated to the measured PV loop is shown in Figure 2.7. Optimized and measured strains are compared in Figure 2.6.

Effect of contraction parameter resolution

In order to quantify the effects of the resolution of the contraction field γ we have repeated the contraction estimation from in-vivo data using regional and scalar resolutions. The fit values obtained for these resolutions are compared to the fit value of the P1 resolution in Table 2.2. The results show that the P1 resolution of γ gives an order of magnitude better strain and volume matches than the scalar and regional resolutions, and that $\bar{I}_{\text{strain}}^{\text{relmax}}$ is about an order of magnitude lower than $\bar{I}_{\text{strain}}$ in all three cases.

The computational cost of the data assimilation using the three resolutions of γ is compared in Table 2.1. We note that the number of forward and adjoint solves increases with the resolution and that the average runtime of an adjoint solve in the scalar and P1 resolutions are almost the same.

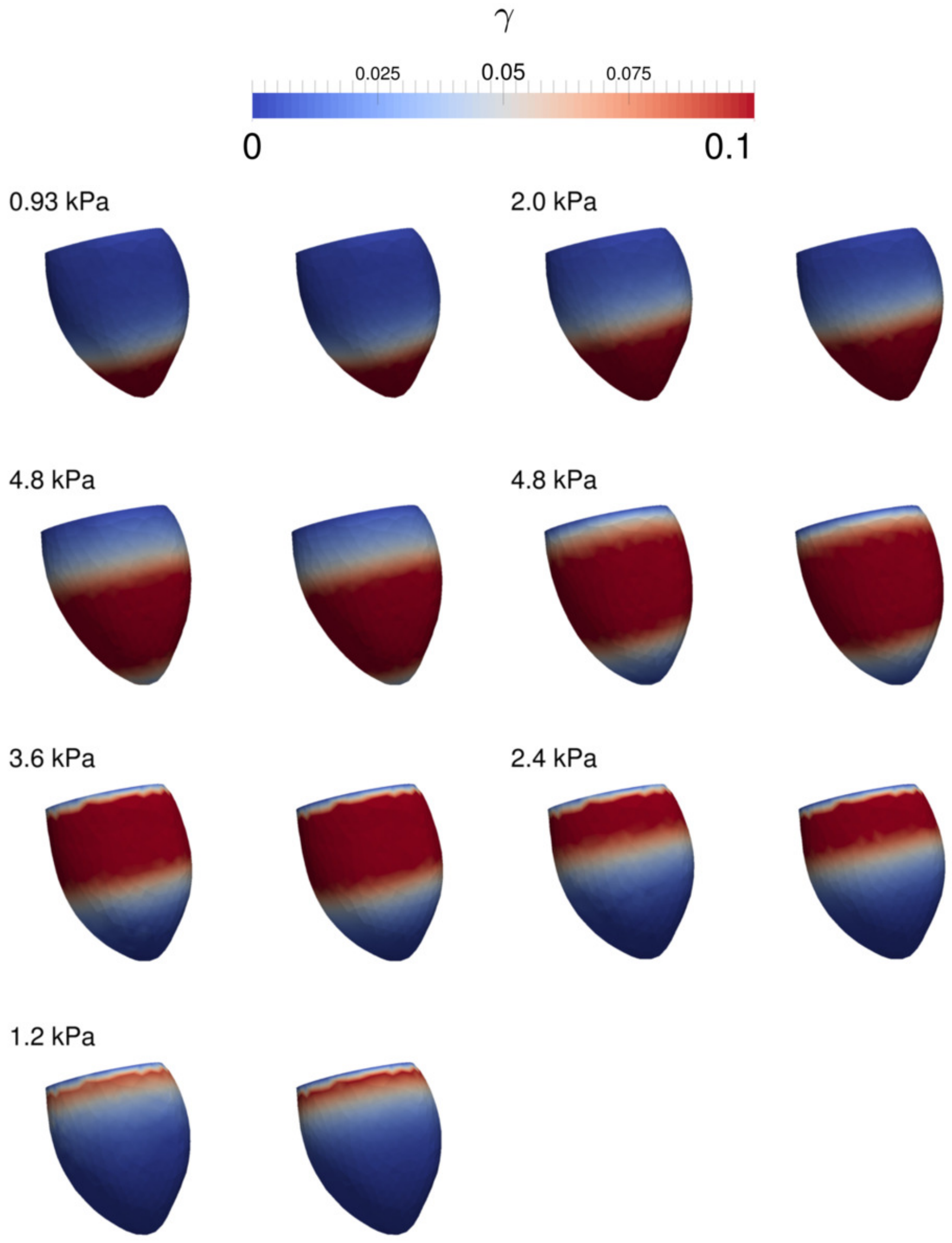
γ
0.025
0.05
0.075
0
0.1
0.93 kPa
2.0 kPa
4.8 kPa
4.8 kPa
3.6 kPa
2.4 kPa
1.2 kPa

Figure 2.5: Lateral view of the ground truth and reconstructed contraction fields at 7 measurement points during the synthetic data test. The target for the optimization is the full strain field with no noise. At each pressure the reconstruction is displayed on the left and the ground truth on the right.

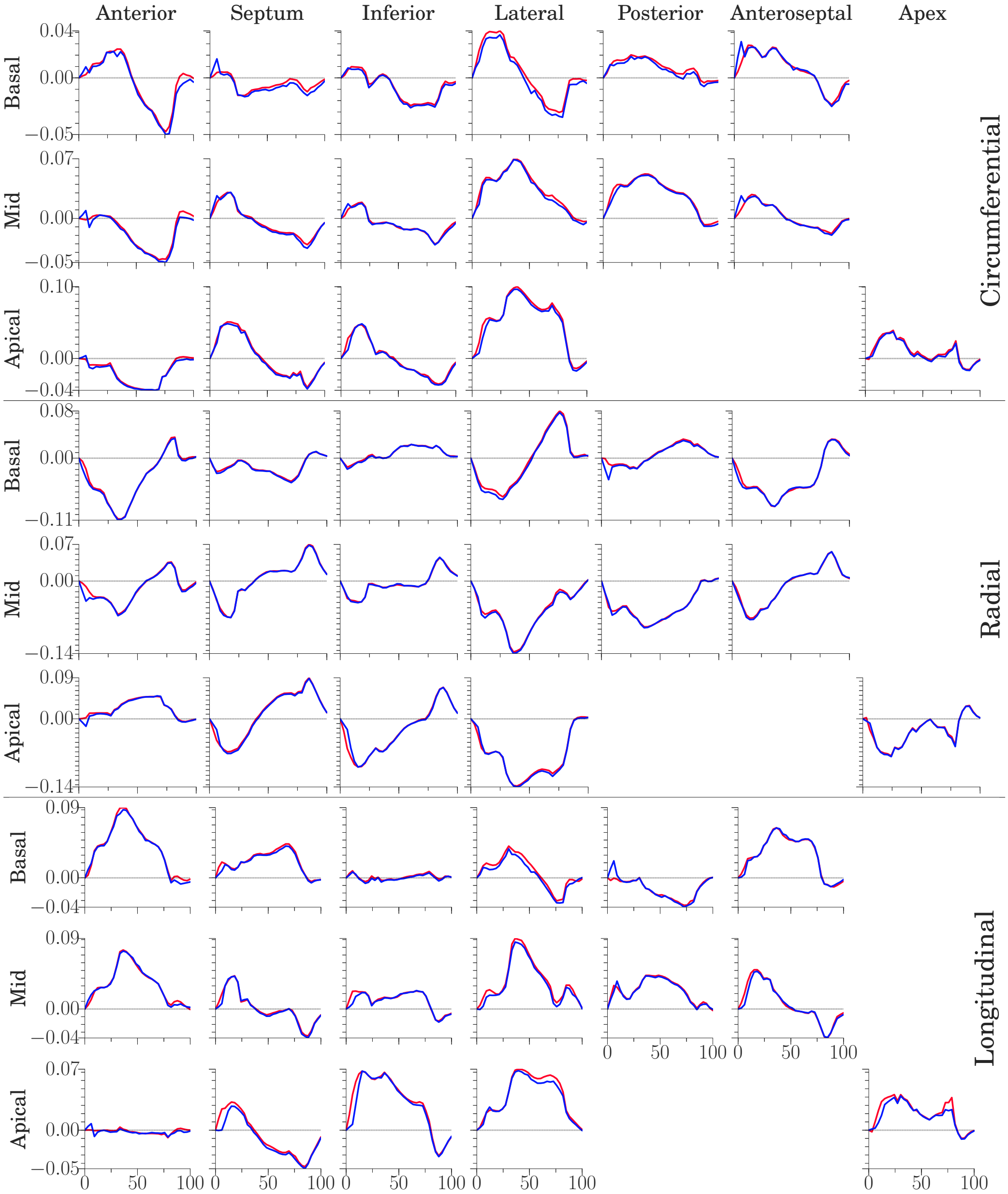

Figure 2.6: Comparison of regional strain curves starting in end diastole. In red: optimized wall motion model data. In blue: clinical data from speckle tracking echocardiography. In each plot the y-axis represents strain while the x-axis shows the progression in time of the cardiac cycle as a percentage.

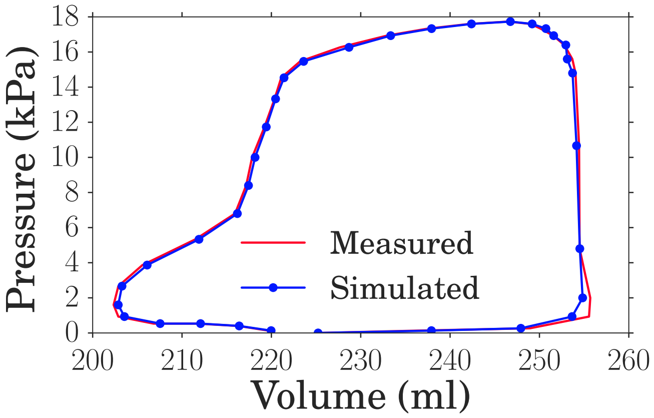

Figure 2.7: Clinically measured (red) versus optimized wall motion model (blue) left ventricular cavity volumes.

Table 2.1: Performance of the contraction optimization with the clinical data for different resolutions of contraction parameter γ. The second and third column display the average number of forward and adjoint solves required to optimize γ at a single measurement point. The fourth column shows the total run time over all measurement points and the final column the average run time of an adjoint solve.

resolution of γ	forward solves average	adjoint solves average	total run time (s)	adjoint evaluation average run time (s)
scalar	4.6	2.8	280	7.4
regional	12	6.5	210	19.3
P1	46	46	1100	7.9

Table 2.2: Relative misfit for different representation of γ

resolution of γ	$\bar{I}_{\text{vol}}$	$\bar{I}_{\text{strain}}$	$\bar{I}^{\text{relmax}}_{\text{strain}}$
scalar	0.044	1.5	0.27
regional	0.024	1.1	0.16
P1	0.0037	0.17	0.029

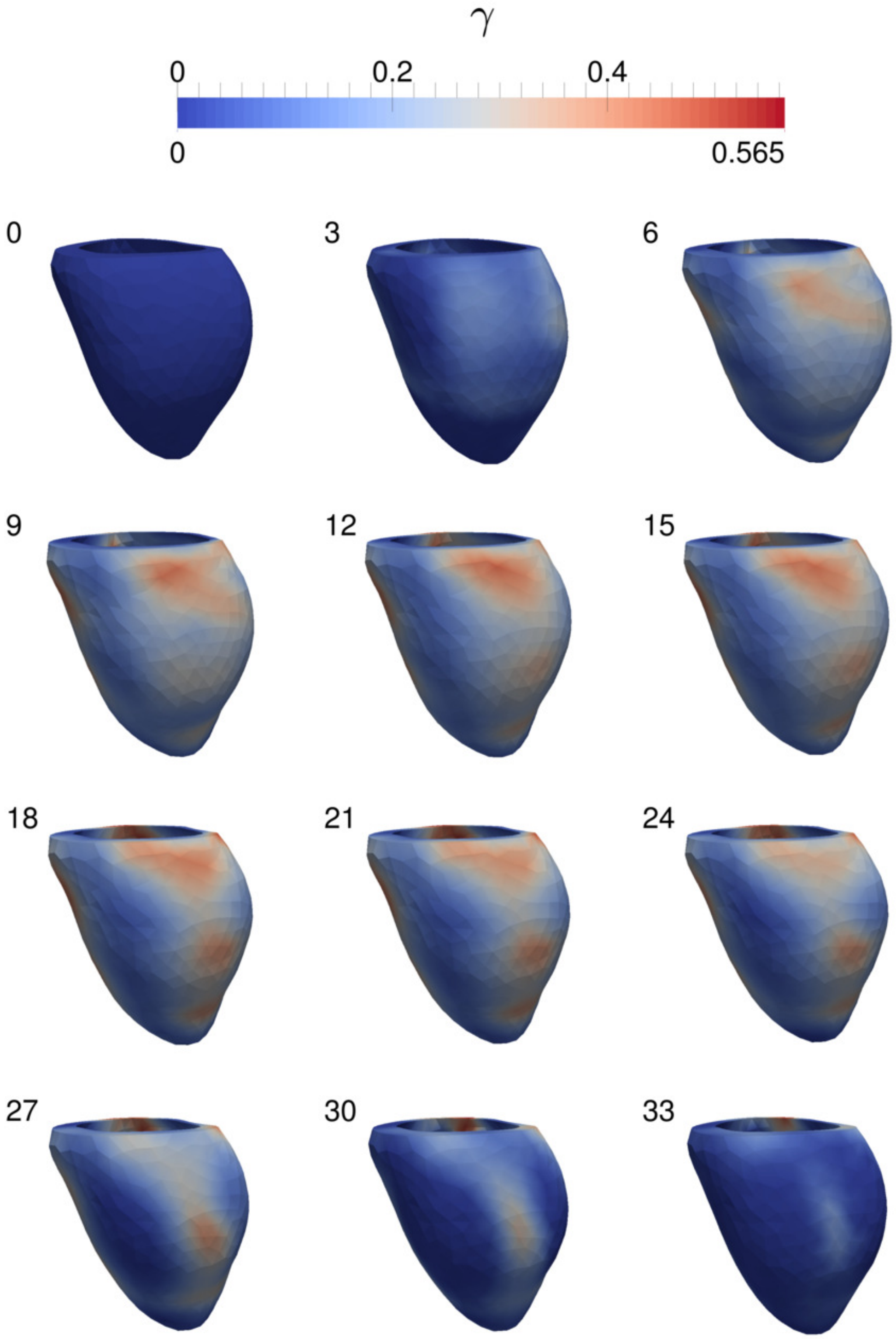
γ
0
0.2
0.4
0
0.565
0
3
6
9
12
15
18
21
24
27
30
33

Figure 2.8: Posterior view of the contraction field γ optimized to in-vivo data at P1 resolution. A snapshot is shown for every third in-vivo measurement point.

Discussion

In our study we have created a personalized model of whole cycle ventricular mechanics based on strain, volume and pressure measurements of a dyssynchronous left ventricle. The contraction parameter in our study was resolved at a high P1 level of resolution. Previous studies [41, 9] have considered contraction parameters that were resolved up to the regional level of AHA zones. By comparing our P1 results to those generated with a regional resolution we have shown that it is possible to greatly increase the fitting ability of a data assimilation method by increasing the parameter resolution. Indeed Table 2.2 shows that the fits $\bar{I}_{\text{vol}}$, $\bar{I}_{\text{strain}}$, and $\bar{I}_{\text{strain}}^{\text{relmax}}$ are an order of magnitude better for the P1 resolution as compared to the regional or scalar resolutions.

Errors in strain fitting were significant at the P1 resolution when compared to the sizes of the strain curves ($\bar{I}_{\text{strain}} = 0.17$). These errors can stem from a fundamental model-data mismatch, and or an inability of the data assimilation to fit the model to the data. In the case of a model-data mismatch the limitations of the model may play a role (see Section 2.4.1). Another cause of model-data mismatch is inaccuracy or noise in measurements, in which case the model can be used to improve the measurements. This is the case when models are used to regularize image based motion [33, 39].

The SQP optimization algorithm that we employed is a local search only, so that is possible that our fitting was suboptimal, possibly contributing to the mismatch in strain. Adding regularization has been shown to prevent such suboptimal results in fluid control problems [[18] page 123]. This partially motivated our use of regularization in the contraction optimization (2.17).

The discrepancies between our model based and measured strains are very small however when compared to the sizes of the largest strain curves of a given strain type, longitudinal, circumferential or radial. This can clearly be seen in Figure 2.6 and in the low value of the metric $\bar{I}_{\text{strain}}^{\text{relmax}}$. This shows that our method was able to accurately capture the larger amplitude features of the heterogeneity in contraction. Such features are less prone to distortion by noise then those with smaller strain values, and are therefore more relevant for potential medical use. However, the question of how much model resolution is actually needed to provide medically useful information remains an open one.

As a consequence of increased dimensionality in the optimization, estimating the contraction γ took just under 4 times longer with the P1 resolution than the scalar resolution. This was due to an increase in the number of forward and adjoint evaluations needed at the higher resolution. However the average run time of an adjoint gradient evaluation did not differ significantly in the P1 case. This near invariance of the gradient calculation cost to the number of optimization parameters is an advantage of the adjoint-gradient method. In the case of the regional resolution the average adjoint-gradient run-time was nearly double that of the other two cases. This was due to increased symbolic computation required by the software dolfin-adjoint to differentiate characteristic functions defined over each AHA segment. The total run-time for the scalar case was higher than for the regional case, despite the scalar case requiring fewer forward and adjoint evaluations. This was due to a greater number of Newton iterations required per forward solve in the scalar case.

In order to test the effects of mesh resolution on the contraction estimation we have considered alternative mesh resolutions in Appendix 2.7.3. The analysis shows that the tested increase and decrease in the resolution of the mesh did not significantly change the fit quality of the contraction estimation (Table 2.5). There were however slight differences in the spatial average of the contraction field between the three cases tested (Figure 2.11). This was most likely due to differences in the quality of the discrete approximation of the work balance equation (2.2).

In the current study the resolution of the computational mesh effected both the resolution of the contraction field and the resolution of the displacement-pressure variables in the FE model. The results of the mesh resolution tests suggest our contraction field may have been too highly resolved, and that it might be beneficial to select the resolution of the contraction variable independently of the mesh in future studies. This would require specifying a set of basis functions for γ, which could be designed to allow for a good fit of model to data while at the same time minimizing the number of degrees of freedom. Such a procedure has been previously implemented for parameter estimation in groundwater modelling [38].

In order to test the accuracy of the contraction estimation we have conducted synthetic data tests for which the true contraction field was known. The results of these tests show that our data assimilation is greatly effected by the sparsity of data. Indeed the approximation of γ was an order of magnitude better with strains that had all 6 components and were defined everywhere on the geometry, as compared to the regionally averaged strains limited to the tensor diagonal. This result did not hold at the apex where the maximum errors were the same for all three cases.

The regionally averaged strain representation is easier for a human to interpret and is widely used in medical research. However for the purposes of building accurate personalized models, more resolution of strain is highly advantageous. The synthetic tests also showed that our data assimilation is not greatly effected by noise in the echocardiographic measurements. This is most likely due to our use of regularization, which favoured smoother solutions that averaged out the effects of the noise.

In addition to noise in strain we can also expect inaccuracies in volume measurements from echocardiography. This is an issue for the estimation of the elastic parameter a, which we conducted purely from volume measurements. Experiments with gel phantoms have quantified this inaccuracy for assessments of a single image [3]. However for the estimation of the elastic parameter a relative differences in errors between images are more relevant. These have to the best of our knowledge not been studied, and so we have conducted estimations of a with volume curves perturbed by a range of errors (see Appendix 2.3.1). These experiments show that the estimated stiffness parameter is indeed sensitive to volume errors. The effect on the average of the contraction field is however quite minimal. An alternative to the current stiffness estimation procedure would be to allow for greater spatial resolution from strain measurements as per the contraction parameter. This might allow for a regularized stiffness field to average out the effects of noisy measurements.

The volume fit between model and data was close for the three points in atrial systole, but significant in early isovolumic contraction. Indeed the model underestimated the measured volumes, indicating an overestimation of ventricular stiffness at these points. This is a consequence of fitting the stiffness parameters to the atrial systolic points, and not to the points afterwards. If the effects of contraction could be isolated from the effects of elasticity it would be possible to include these points in the elastic parameter fitting and possibly obtain a better match of volumes.

In our study we personalized only a single elastic parameter a, which was done for the sake of simplicity. Previous studies have successfully estimated greater numbers of elastic parameters for the reduced Holzapfel law [1] and the fully orthortropic Holzapfel law [14]. Such procedures could be potentially combined with our contraction estimation in order to increase the level of model personalization. Another potential improvement of the elastic parameter estimation we employed is the inclusion of aggregated geometry measures; such as short axis and long axis diameters. Such measures have been shown to improve identifiability of elastic parameters in experiments with mouse ventricles [32].

Several data assimilation studies [29, 36] have included objective functionals consisting of strain and volume components with equal weighing given to both. We have shown that it may be possible to improve such data assimilation procedures by tuning the relative weight of strain and volume components. Indeed in the top right plot of Figure 2.3 there is a definite corner in the strain-volume fitting space consisting of 4 points beneath $\alpha = 0.95$. Choosing α among these points gives a fair trade-off between strain and volume matching whereas any choice outside this corner simply worsens the fit of strain or volume without much improving the other.

In Figure 2.3 we have shown how the parameters α and λ effect the fitting and smoothness metrics related to the contraction field γ. Additionally, we have tested the effects of variations in α and λ on the spatial average of the contraction field. These experiments are presented in Appendix 2.7.4. Figure 2.12 shows that varying α in the region $[0, 0.5]$ had little to no effect on the spatial average of γ, whereas increases in α outside of this region tended to increase the amount of contraction. This behaviour correlates with the value of $\bar{I}_{\text{strain}}$ in (Figure 2.3 top right). Similarly, increasing λ beyond 0.001 tended to increase the misfit in the data functional (Figure 2.3 bottom right), and also increase the average amount of contraction (Figure 2.12 right). We hypothesize that additional levels of misfit in strain introduced by increasing α beyond 0.5 and or λ beyond 0.001 lead to overestimating the amount of contraction in our patient's LV. However we lack knowledge of the true amount of muscle contraction in the patient which could be used to test the hypothesis. Further validation of the model and data assimilation are needed.

Limitations

The results obtained in this article were limited by issues pertaining to the choice of mathematical model, quality of clinical data, numerical stability, and the design of the data assimilation algorithm. Firstly, the boundary conditions of the ventricle wall motion model did not account for the effects of the right ventricular pressure on the septum, and the mechanical coupling to the neighboring structures: left atrium, right ventricle and pericardium.

The in-vivo circumferential and radial motion at the base was not incorporated into the model. Instead some motion was allowed by the basal spring, whose constant k needed to be chosen. In the future we would like to incorporate basal motion data from the images into our personalized model. This would allow us to avoid having to make a choice of k and hopefully allow for the reproduction of in-vivo basal motion in the personalized model.

During the atrial systole phase we assumed $\gamma = 0$. This allowed for the estimation of passive properties separate from contraction. This assumption is appropriate for a healthy ventricle but might be false in a diseased ventricle if muscle relaxation is sufficiently delayed.

Our mathematical model of wall motion neglected the effects of visco-elasticity, tissue compressibility [43], inertia, and myocardial sheet microstructure. Finally the reference geometry that we used for our calculations came from an echocardiographic image in which there was a non-zero level of blood pressure. The blood pressures we used in our patient specific model were off by the 2.8 kPa which we subtracted in order to have 0 pressure in the reference geometry. This pressure adjustment meant that the elastic stiffness of the ventricle was underestimated by our elastic parameter estimation, as the mathematical model operated at a lower pressure than measured in the patient's heart.

The accuracy of the optimized motion model is limited by uncertainties in the clinical strain and volume measurements, which are related to echocardiographic image quality, image sample rate, and speckle tracking algorithm accuracy. Pressure and volume measurements had to be synchronized, which might have lead to a potentially unphysiological loss of volume in the iso-volumic relaxation phase of the in-vivo PV loop (Figure 2.2).

Finally there were several algorithmic limitations. Firstly, the optimized γ fields we computed may or may not have been unique. For potential clinical applications this is a concern as the uniqueness of parameters relate to the reproducibility and consistency of data obtained from a personalized model. Furthermore, our procedures for choosing the functional weights α and λ were not optimal. In both the synthetic and clinical data case the weight values were chosen by parameter sweeps that kept a single parameter fixed, which did not account for possibly better α, λ combinations lying outside of the areas we tested. Finally the SQP optimization algorithm that we employed was a local search only, that is only one minimum of the objective is calculated. Better parameter fits may be possible with global optimization methods that explore multiple minima.

Conclusion and Future Outlook

By employing high resolution data assimilation we were able to capture the detailed motion of a dyssynchronous left ventricle in a computational model with an excellent fit of model observations to data. This demonstrates the power of the data assimilation method, which can also be applied to other models and or model parameters.

In the future the proposed method should be further improved and tested on cohorts of patients. This would allow for the study of simulated contraction patterns among groups of patients that could lead to further understanding of dyssynchrony.

Author Declaration

All of the clinical data for this study was collected with the approval of the Norwegian national ethics committee, REC, and in accordance to the Helsinki Declaration of 1975, as revised in 2000.

Computations were performed on the Abel supercomputing cluster at the University of Oslo via Notur projects nn9316k and nn9249k.

Appendix

Sensitivity of elastic a parameter to error in atrial systolic volume measurements

In order to test the sensitivity of our estimated a parameter to uncertainty in volume measurements we have carried out a series of estimations with various levels of volume perturbation. We generated clean volume data using the computational model using $a = 0.435$ kPa, the optimal value obtained from the clinical data. Perturbations in volume increases of sizes $\pm 5, 15, 25\%$ were added to this data, which were then used as target for optimization. The resulting a values and perturbations are shown in Table 2.3. The largest perturbations resulted in the a values 0.494 kPa and 0.384 kPa, representing circa $\pm\%13$ change from the original a value.

The resulting average value of γ is shown in Figure 2.9 for the extreme cases with $\alpha = 0.494$ and $\alpha = 0.384$. For reference we also include the average value of γ using $\alpha = 0.435$.

Sensitivity of estimated parameters to spring constant k.

The spring boundary condition that we used at the ventricular base has a significant effect on the simulated cavity volumes calculated by the model. This is due

Table 2.3: Sensitivity of the optimized material parameter a to errors in volume measurements. The first column gives the perturbation of the volume increase between measurement points 1-2 and 2-3, in percent. The next two columns give the size of these perturbations in mL with ΔV_2 and ΔV_3 referring to perturbations in the volumes of the second and third measurement points respectively. In the fourth column optimal a values are given. In all cases the volume fit $\bar{I}_{\text{vol}}$ was less than 4×10^{-6}.

perturbation (%)	ΔV_2 (ml)	ΔV_3 (ml)	a (kPa)
-25	-1.2	-1.06	0.494
-15	-0.717	-0.636	0.469
-5	-0.239	-0.212	0.446
0	0	0	0.435
5	0.239	0.212	0.424
15	0.717	0.636	0.404
25	1.2	1.06	0.384

to the cross-sectional area of the cavity being large at the ventricular base. Therefore we can expect the choice of k to have an effect on the optimal parameters calculated by our data assimilation.

In order to quantify this effect we have carried out a sensitivity analysis, starting with the effect of k on the optimized elastic parameter a. We repeated the elastic parameter fitting decribed in Section 2.3.1 and varied the k-value from 0.001 to 100.0. We also considered the case $k = \infty$, denoting a completely rigid boundary held by Dirichlet boundary conditions. The effect of the choice of k on the optimal value of a is shown in Table 2.4. The table shows that the optimal a varies from 0.365 kPa to 0.875 kPa depending upon how the k parameter is set.

We also tested the sensitivity of the contraction γ at P1 resolution to k by repeating the estimation of γ with the various k and a pairs obtained in the previous experiment. For each k, a pair we have plotted the spatial average of contraction $\bar{\gamma}$ at each measurement point in Figure 2.10. The results show up to a 20% variation in $\bar{\gamma}$ and very little variation for the choices of k greater than or equal to 1.0. For some of the values of $k < 1.0$ our homotopy Newton solver was unable to secure convergence during the optimization. Curves corresponding to these cases are drawn only to the point before the non-convergence occurred.

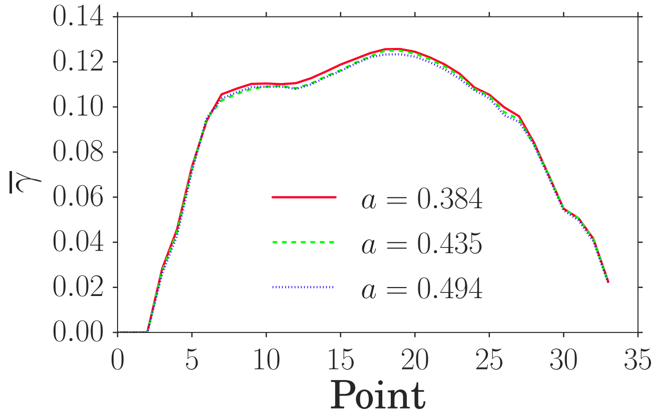

Figure 2.9: Sensitivity of the optimal average contraction $\bar{\gamma}$ to changes in the parameter a. The upper and lower a values are based on estimating a with volume perturbations of ±25% (Tabel 2.3). The middle value was obtained by estimating a from in-vivo volumes.

Table 2.4: Sensitivity of optimal a value to choice of spring constant k.

k	10^{-8}	10^{-7}	10^{-6}	10^{-5}	10^{-4}	10^{-3}	0.01	0.1	1	10	100	∞
a	0.875	0.875	0.875	0.875	0.873	0.873	0.849	0.684	0.435	0.375	0.366	0.365

Effect of mesh resolution on estimated contraction γ at P1 resolution

Ventricular meshes were generated by Gmsh [16] with three different resolutions controlled by the parameter 'Mesh.CharacteristicLengthFactor'. This parameter was given the values 1.0, 0.65 and 0.45 which resulted in meshes with 549, 1262 and 2261 vertices respectively. Using the three meshes we estimated contraction fields from the in-vivo data. The average value of γ is shown for these three cases in Figure 2.11. Fit quality is compared in Table 2.5.

Sensitivity of Contraction Size to choices of α and λ

Based on the trade-off curves in Figure 2.3 we chose the optimization weights $\alpha = 0.95$ and $\lambda = 0.01$ for the personalization of our wall motion model to the in-vivo data. In order to show the effect of these choices on the optimized contraction field γ we have varied the α and λ values and plotted the spatial averages of the

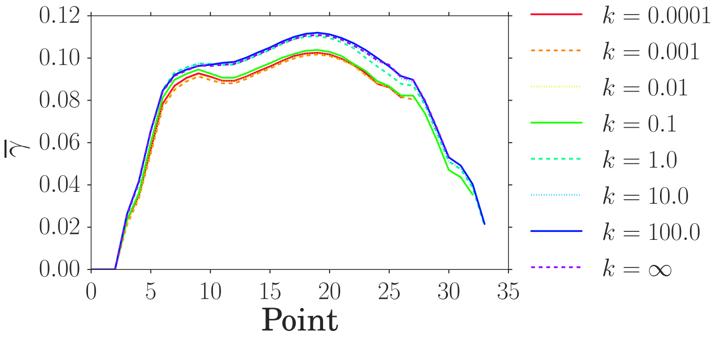

Figure 2.10: Sensitivity of the spatially averaged contraction $\bar{\gamma}$ to the choice of spring constant k.

Table 2.5: Relative misfit for different mesh resolutions

Number of elements	$\bar{I}_{\text{vol}}$	$\bar{I}_{\text{strain}}$	$\bar{I}_{\text{strain}}^{\text{relmax}}$
549	0.0033	0.17	0.029
1262	0.0037	0.17	0.029
2661	0.0043	0.18	0.031

resulting contraction fields. The results show that the amount of contraction tends to increase proportionally to both α and λ beyond the thresholds $\alpha = 0.5$ and $\lambda = 0.001$.

Estimation of noise in echo speckle tracking strain measurements

In order to increase the relevance of the synthetic tests we considered a set of regional strains that contained noise. This noise was modelled as an additive Gaussian process in order to imitate the accumulation of tracking errors in EchoPac's image based strain calculations. The mean and variance of a summand in the Gaussian process were estimated from our in-vivo strain data of a single patient. From this data the sample means and variances of the drift values were divided by the number of measurement points in order to approximate the noise in a single measurement. The mean and covariance of this single measurement point noise are given in Table 2.6.Theoretically, error free strain curves would have no drift given stable conditions in the heart. This motivates the use of the drift values in order to approximate the tracking error.

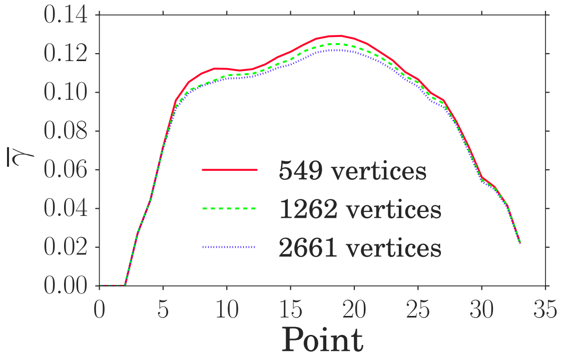

Figure 2.11: Spatial average of contraction $\overline{\gamma}$ for 3 different mesh resolutions.

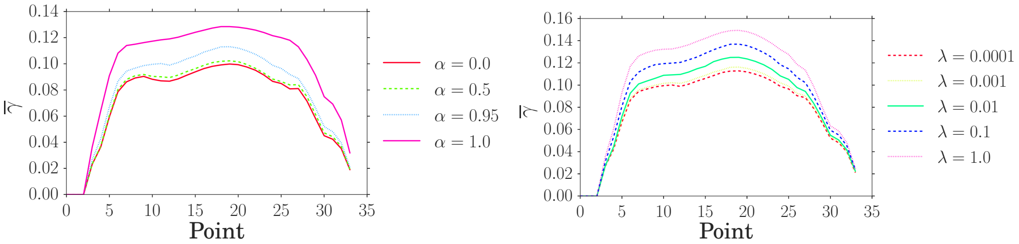

Figure 2.12: Sensitivity of the spatially averaged contraction $\overline{\gamma}$ to variations in optimization weights α and λ. Left: $\lambda = 0$ and α is varied. Right: $\alpha = 0.95$ and λ is varied.

Table 2.6: Mean and covariance of a Gaussian noise summand estimated from patient drift values in circumferential (C), radial (R) and longitudinal (L) directions.

	Covariance $\times 10^{-4}$			Mean
	C	R	L	
C	1.43	0.73	0.66	0.006
R	-	6.8	6.31	-0.013
L	-	-	7.26	0.01

Bibliography

[1] Liya Asner, Myrianthi Hadjicharalambous, Radomir Chabiniok, Devis Peresutti, Eva Sammut, James Wong, Gerald Carr-White, Philip Chowienczyk, Jack Lee, Andrew King, et al. Estimation of passive and active properties in the human heart using 3d tagged mri. *Biomechanics and modeling in mechanobiology*, pages 1–19, 2015.

[2] Kevin F Augenstein, Brett R Cowan, Ian J LeGrice, Poul MF Nielsen, and Alistair A Young. Method and apparatus for soft tissue material parameter estimation using tissue tagged magnetic resonance imaging. *Journal of biomechanical engineering*, 127(1):148–157, 2005.

[3] Matthias Aurich, Florian André, Marius Keller, Sebastian Greiner, Alexander Hess, Sebastian J Buss, Hugo A Katus, and Derliz Mereles. Assessment of left ventricular volumes with echocardiography and cardiac magnetic resonance imaging: real-life evaluation of standard versus new semiautomatic methods. *Journal of the American Society of Echocardiography*, 27(10):1017–1024, 2014.

[4] Gabriel Balaban, Martin S Alnæs, Joakim Sundnes, and Marie E Rognes. Adjoint multi-start-based estimation of cardiac hyperelastic material parameters using shear data. *Biomechanics and Modeling in Mechanobiology*, pages 1–13, 2016.

[5] S Balay, J Brown, K Buschelman, WD Gropp, D Kaushik, MG Knepley, L Curfman McInnes, BF Smith, and H Zhang. PETSc web page. http://www.mcs.anl.gov/petsc, 2015.

[6] JD Bayer, RC Blake, G Plank, and NA Trayanova. A novel rule-based algorithm for assigning myocardial fiber orientation to computational heart models. *Annals of biomedical engineering*, 40(10):2243–2254, 2012.

[7] Joris Bols, Joris Degroote, Bram Trachet, Benedict Verhegghe, Patrick Segers, and Jan Vierendeels. A computational method to assess the in vivo stresses and unloaded configuration of patient-specific blood vessels. *Journal of Computational and Applied Mathematics*, 246:10–17, 2013.

[8] Manuel D Cerqueira, Neil J Weissman, Vasken Dilsizian, Alice K Jacobs, Sanjiv Kaul, Warren K Laskey, Dudley J Pennell, John A Rumberger,

Thomas Ryan, Mario S Verani, et al. Standardized myocardial segmentation and nomenclature for tomographic imaging of the heart a statement for healthcare professionals from the cardiac imaging committee of the Council on Clinical Cardiology of the American Heart Association. *Circulation*, 105(4):539–542, 2002.

[9] Radomir Chabiniok, Philippe Moireau, P-F Lesault, Alain Rahmouni, J-F Deux, and Dominique Chapelle. Estimation of tissue contractility from cardiac cine-MRI using a biomechanical heart model. *Biomechanics and modeling in mechanobiology*, 11(5):609–630, 2012.

[10] H Delingette, F Billet, K C L Wong, M Sermesant, K Rhode, M Ginks, C A Rinaldi, R Razavi, and N Ayache. Personalization of cardiac motion and contractility from images using variational data assimilation. *Biomedical Engineering, IEEE Transactions on*, 59(1):20–24, January 2012.

[11] A Evangelista, P Nardinocchi, PE Puddu, L Teresi, C Torromeo, and V Varano. Torsion of the human left ventricle: experimental analysis and computational modeling. *Progress in biophysics and molecular biology*, 107(1):112–121, 2011.

[12] Patrick E Farrell, David A Ham, Simon W Funke, and Marie E Rognes. Automated derivation of the adjoint of high-level transient finite element programs. *SIAM Journal on Scientific Computing*, 35(4):C369–C393, 2013.

[13] Henrik Finsberg and Gabriel Balaban. High resolution data assimilation of cardiac mechanics. http://www.bitbucket.org/finsberg/cardiac_highres_dataassim, 2016.

[14] H Gao, WG Li, L Cai, C Berry, and XY Luo. Parameter estimation in a Holzapfel–Ogden law for healthy myocardium. *Journal of engineering mathematics*, 95(1):231–248, 2015.

[15] MW Gee, Ch Förster, and WA Wall. A computational strategy for prestressing patient-specific biomechanical problems under finite deformation. *International Journal for Numerical Methods in Biomedical Engineering*, 26(1):52–72, 2010.

[16] Christophe Geuzaine and Jean-François Remacle. Gmsh: A 3-D finite element mesh generator with built-in pre-and post-processing facilities. *Inter-*

national Journal for Numerical Methods in Engineering, 79(11):1309–1331, 2009.

[17] Sjur Gjerald, Johan Hake, Simone Pezzuto, Joakim Sundnes, and Samuel T Wall. Patient–specific parameter estimation for a transversely isotropic active strain model of left ventricular mechanics. In *Statistical Atlases and Computational Models of the Heart-Imaging and Modelling Challenges*, pages 93–104. Springer, 2015.

[18] Max D Gunzburger. *Perspectives in flow control and optimization*, volume 5. Siam, 2003.

[19] Myrianthi Hadjicharalambous, Radomir Chabiniok, Liya Asner, Eva Sammut, James Wong, Gerald Carr-White, Jack Lee, Reza Razavi, Nicolas Smith, and David Nordsletten. Analysis of passive cardiac constitutive laws for parameter estimation using 3D tagged MRI. *Biomechanics and modeling in mechanobiology*, 14(4):807–828, 2015.

[20] Gerhard a Holzapfel and Ray W Ogden. Constitutive modelling of passive myocardium: a structurally based framework for material characterization. *Philosophical transactions. Series A, Mathematical, physical, and engineering sciences*, 367(1902):3445–75, sep 2009.

[21] P Hood and C Taylor. Navier-stokes equations using mixed interpolation. *Finite element methods in flow problems*, pages 121–132, 1974.

[22] Oslo University Hospital. Acute feedback on left ventricular lead implantation location for cardiac resynchronization therapy (CCI impact). https://clinicaltrials.gov, 2016.

[23] Dieter Kraft et al. *A software package for sequential quadratic programming*. DFVLR Obersfaffeuhofen, Germany, 1988.

[24] Adarsh Krishnamurthy, Christopher T Villongco, Joyce Chuang, Lawrence R Frank, Vishal Nigam, Ernest Belezzuoli, Paul Stark, David E Krummen, Sanjiv Narayan, Jeffrey H Omens, Andrew D McCulloch, and Roy Cp Kerckhoffs. Patient-specific models of cardiac biomechanics. *Journal of computational physics*, 244:4–21, july 2013.

[25] Sander Land, Steven Niederer, Pablo Lamata, Nicolas P Smith, et al. Improving the stability of cardiac mechanical simulations. *Biomedical Engineering, IEEE Transactions on*, 62(3):939–947, 2015.

[26] Xiaoye S. Li and James W. Demmel. SuperLUDIST: A scalable distributed-memory sparse direct solver for unsymmetric linear systems. *ACM Trans. Mathematical Software*, 29(2):110–140, June 2003.

[27] Anders Logg, Kent-Andre Mardal, Garth N. Wells, et al. *Automated Solution of Differential Equations By the Finite Element Method.* Springer, 2011.

[28] S Marchesseau, H Delingette, M Sermesant, M Sorine, K Rhode, S G Duckett, C a Rinaldi, R Razavi, and N Ayache. Preliminary specificity study of the Bestel-Clément-Sorine electromechanical model of the heart using parameter calibration from medical images. *Journal of the mechanical behavior of biomedical materials*, 20:259–71, May 2013.

[29] Dimitri Mojsejenko, Jeremy R McGarvey, Shauna M Dorsey, Joseph H Gorman III, Jason A Burdick, James J Pilla, Robert C Gorman, and Jonathan F Wenk. Estimating passive mechanical properties in a myocardial infarction using MRI and finite element simulations. *Biomechanics and modeling in mechanobiology*, 14(3):633–647, 2014.

[30] Paola Nardinocchi and Luciano Teresi. On the active response of soft living tissues. *Journal of Elasticity*, 88(1):27–39, 2007.

[31] Dominik Neumann, Tommaso Mansi, Bogdan Georgescu, Ali Kamen, Elham Kayvanpour, Ali Amr, Farbod Sedaghat-Hamedani, Jan Haas, Hugo Katus, Benjamin Meder, et al. Robust image-based estimation of cardiac tissue parameters and their uncertainty from noisy data. In *Medical Image Computing and Computer-Assisted Intervention–MICCAI 2014*, pages 9–16. Springer, 2014.

[32] Øyvind Nordbø, Pablo Lamata, Sander Land, Steven Niederer, Jan M Aronsen, William E Louch, Ivar Sjaastad, Harald Martens, Arne B Gjuvsland, Kristin Tøndel, et al. A computational pipeline for quantification of mouse myocardial stiffness parameters. *Computers in biology and medicine*, 53:65–75, 2014.

[33] Xenophon Papademetris, Albert J Sinusas, Donald P Dione, R Todd Constable, and James S Duncan. Estimation of 3-d left ventricular deformation from medical images using biomechanical models. *IEEE transactions on medical imaging*, 21(7):786–800, 2002.

[34] S Pezzuto, D Ambrosi, and A Quarteroni. An orthotropic active–strain model for the myocardium mechanics and its numerical approximation. *European Journal of Mechanics-A/Solids*, 2014.

[35] Maxime Sermesant, Philippe Moireau, Oscar Camara, Jacques Sainte-Marie, Rado Andriantsimiavona, Robert Cimrman, Derek LG Hill, Dominique Chapelle, and Reza Razavi. Cardiac function estimation from MRI using a heart model and data assimilation: advances and difficulties. *Medical Image Analysis*, 10(4):642–656, 2006.

[36] Kay Sun, Nielen Stander, Choon-Sik Jhun, Zhihong Zhang, Takamaro Suzuki, Guan-Ying Wang, Maythem Saeed, Arthur W Wallace, Elaine E Tseng, Anthony J Baker, et al. A computationally efficient formal optimization of regional myocardial contractility in a sheep with left ventricular aneurysm. *Journal of biomechanical engineering*, 131(11):111001, 2009.

[37] Hari Sundar, Christos Davatzikos, and George Biros. Biomechanically-constrained 4D estimation of myocardial motion. In *Medical Image Computing and Computer-Assisted Intervention–MICCAI 2009*, pages 257–265. Springer, 2009.

[38] Frank T-C Tsai, Ne-Zheng Sun, and William W-G Yeh. Global-local optimization for parameter structure identification in three-dimensional groundwater modeling. *Water Resources Research*, 39(2), 2003.

[39] Viateur Tuyisenge, Laurent Sarry, Thomas Corpetti, Elisabeth Innorta-Coupez, Lemlih Ouchchane, and Lucie Cassagnes. Estimation of myocardial strain and contraction phase from cine mri using variational data assimilation. *IEEE transactions on medical imaging*, 35(2):442–455, 2016.

[40] Vicky Y Wang, H I Lam, Daniel B Ennis, Brett R Cowan, Alistair a Young, and Martyn P Nash. Modelling passive diastolic mechanics with quantitative MRI of cardiac structure and function. *Medical image analysis*, 13(5):773–84, October 2009.

[41] Ken CL Wong, Maxime Sermesant, Kawal Rhode, Matthew Ginks, C Aldo Rinaldi, Reza Razavi, Hervé Delingette, and Nicholas Ayache. Velocity-based cardiac contractility personalization from images using derivative-free optimization. *Journal of the mechanical behavior of biomedical materials*, 43:35–52, 2015.

[42] Jiahe Xi, Pablo Lamata, Jack Lee, Philippe Moireau, Dominique Chapelle, and Nic Smith. Myocardial transversely isotropic material parameter estimation from in-silico measurements based on a reduced-order unscented Kalman filter. *Journal of the mechanical behavior of biomedical materials*, 4(7):1090–1102, 2011.

[43] FC Yin, CC Chan, and Robert M Judd. Compressibility of perfused passive myocardium. *American Journal of Physiology-Heart and Circulatory Physiology*, 271(5):H1864–H1870, 1996.

Paper 2

Estimating cardiac contraction through high resolution data assimilation of a personalized mechanical model

Estimating cardiac contraction through high resolution data assimilation of a personalized mechanical model

Henrik Finsberg[1,2,4], Gabriel Balaban[6], Stian Ross[3,4], Trine Håland[3,4], Hans Henrik Odland[3,4], Joakim Sundnes[1,2,4], and Samuel Wall[1,3,5]

1. Simula Research Laboratory, Lysaker, Norway
2. Department of Informatics, University of Oslo, Oslo, Norway
3. Faculty of Medicine, University of Oslo, Oslo, Norway
4. Center for Cardiological Innovation, Oslo, Norway
5. Department of Mathematical Science and Technology, NMBU, Ås, Norway
6. Department of Imaging Sciences and Bioengineering, KCL, London, England

Abstract

Cardiac computational models, individually personalized, can provide clinicians with useful diagnostic information and aid in treatment planning. A major bottleneck in this process can be determining model parameters to fit created models to individual patient data. However, adjoint-based data assimilation techniques can now rapidly estimate high dimensional parameter sets. This method is used on a cohort of heart failure patients, capturing cardiac mechanical information and comparing it with a healthy control group. Excellent fit ($R^2 \geq 0.95$) to systolic strains is obtained, and analysis shows a significant difference in estimated contractility between the two groups.

Introduction

Patient-specific cardiac modeling has emerged as a potential tool for clinical diagnosis as well as treatment optimization[20]. By linking patient measurements to physical processes through a mathematical framework, models can provide us with additional insight into cardiac function or dysfunction at the level of the individual. However, the complexity of the heart makes this difficult, and this is recognized as a key challenge in modern bioengineering [12].

One difficulty is the effort to personalize models and simulations to individual patients. While a wealth of clinical data exists to parameterize such 'patient-specific' models, methods to assimilate this data into simulations can involve extensive computation time, often putting them outside the scope of clinical utility. However, new methods are emerging to improve the flow of clinical measurements into powerful data driven simulations. Automated geometry segmentation [17] and improved optimization techniques [6], can improve the speed at which patient-specific models can be built and parameterized. In particular, recent advancements in adjoint-based data assimilation techniques [2] offer an efficient way to assimilate ventricular mechanical information using highly spatially resolved parameters.

Here we use an adjoint based assimilation method with a mechanical model in order to construct simulations that accurately reflect clinical motion data, both for healthy controls and patients suffering from left bundle branch block (LBBB). The use of a highly spatially resolved contraction parameter, enabled through adjoint-methods, provides excellent data fit to measured strains and volumes, and fit models provide estimates of cardiac contraction. Such biomarkers may prove useful to clinicians for diagnoses of problems with cardiac function, and to better plan therapies.

Materials and methods

Data acquisition

Clinical measurements of cardiac function for seven LBBB patients were obtained from the Impact study [11]. Data was also acquired for seven healthy volunteers. 4D echocardiographic images of the left ventricle (LV), for both the LBBB patients and healthy subjects, were captured using a GE Vingmed E9 device, and analysis carried out with the software package EchoPac. For each subject, depending on frame rate and cardiac cycle time, the analysis provided between 15 and 50 LV volumes, geometric segmentations of the LV endocardium and epicardium, and cardiac strain calculated via speckle tracking. The strain were defined according to the 17 segment AHA-zone representation [5], in the longitudinal, radial and circumferential direction, giving a total of 51 strain measurements per time point, with the reference time point for strain analysis being the first frame after onset of QRS.

The LBBB patients had LV pressure measurements taken during implantation of a cardiac resynchronization therapy (CRT) device, and valvular events were used to synchronize the pressure to the echo data. In the healthy control group, where invasive pressure measurements were absent, the pressure waveform from one of the LBBB patients was used and scaled to reported values of the end-diastolic and end-systolic left ventricular pressure [Table 30-1 in [13]].

Automated geometry and microstructure creation

For each patient, a 3D tetrahedral mesh of the LV was constructed from triangulated segmented surfaces of the endo- and epicardium corresponding to the frame at the beginning of atrial systole, Figure 3.1. A cut was made at the ventricular base of the segmentation, so that the mesh cavity volume and the ultrasound measured volume differed by less than 1 ml. Mesh cells were marked into the 17 AHA regions through the regionally delineated strain data, and the myocardial fiber orientation, denoted by $\mathbf{f}_0$, were assigned using the algorithm from Bayer et al [4], with the endo- and epicardial helix fiber angles set to $\alpha_{\text{endo}} = 60$ and $\alpha_{\text{epi}} = -60$, respectively.

Mechanical Model

We represent the heart as a hyperelastic continuum body, where the coordinates in the reference ($\mathbf{X}$) and the current ($\mathbf{x}$) configuration are related via the displacement field $\mathbf{u} = \mathbf{x} - \mathbf{X}$. Furthermore, we utilize the deformation gradient, the determinant of the deformation gradient and, the right Cauchy-Green deformation tensor given by $\mathbf{F} = \mathbf{I} + \nabla\mathbf{u}$, $J = \det\mathbf{F}$ and $\mathbf{C} = \mathbf{F}^T\mathbf{F}$, respectively. To model the passive behavior of the myocardium, the transversely isotropic strain energy function proposed in [10] is adopted:

$$\mathscr{W}(I_1, I_{4\mathbf{f}_0}) = \frac{a}{2b}\left(\exp\{b(I_1 - 3)\} - 1\right) + \frac{a_f}{2b_f}\left(\exp\left\{b_f(I_{4\mathbf{f}_0} - 1)_+^2\right\} - 1\right). \quad (3.1)$$

Here $I_1 = \operatorname{tr}\mathbf{C}$ and $I_{4\mathbf{f}_0} = \mathbf{f}_0 \cdot (\mathbf{C}\mathbf{f}_0)$ are invariants of $\mathbf{C}$, $(\cdot)_+ = \max\{\cdot, 0\}$, and a, a_f, b, b_f are material stiffness parameters defining the elastic properties of the myocardium. We follow a common approach and assume that the myocardium is incompressible. Incompressibility is incorporated in the model by using a two-field variational approach, where we introduce a Lagrange multiplier p which represents the hydrostatic pressure, and the term $p(J-1)$ is added to the strain-energy.

To model the active response we apply the approach of active strain [1], which is based on decomposing the deformation gradient into active and passive contributions, $\mathbf{F} = \mathbf{F}_e\mathbf{F}_a$. We choose $\mathbf{F}_a = (1-\gamma)\mathbf{f}_0 \otimes \mathbf{f}_0 + \frac{1}{\sqrt{1-\gamma}}(\mathbf{I} - \mathbf{f}_0 \otimes \mathbf{f}_0)$, where γ is a parameter that represents the relative active shortening along the fibers. For reference, we have also performed tests with the commonly used active stress formulation, where the stress tensor is additively decomposed into active and passive stress $\sigma = \sigma_p + \sigma_a$. Here σ_p is the elastic material response, and $\sigma_a = T_a\mathbf{f} \otimes \mathbf{f}$ with $\mathbf{f} = \mathbf{F}\mathbf{f}_0$ and T_a a scalar variable representing active fiber tension.

For both approaches, the resulting displacement field $\mathbf{u}$ and hydrostatic pressure p are determined by using the principle of stationary potential energy [9], which is based on minimizing the total energy $\Pi(\mathbf{u}, p)$, which includes internal energy derived from (3.1) and external energy. The external energy includes contributions from the measured cavity pressure p_{LV}, and a linear spring term at the basal boundary, with spring constant k = 10.0 kPa. The equilibrium solution is found by solving for the minimum potential energy, $\delta\Pi(\mathbf{u}, p) = 0$.

Data Assimilation

In order to constrain the model to each patient's clinical measurements, we consider a PDE-constrained optimization problem where the objective functional is given by the misfit between simulated and measured strain and volume along with a first order Tikhonov regularization of the model parameters.

$$\begin{aligned} \underset{m}{\text{minimize}} \quad & \alpha\left(\frac{V^i - \tilde{V}^i}{V^i}\right)^2 + (1-\alpha)\sum_{j=1}^{17}\sum_{k\in\{c,r,l\}}\left(\varepsilon_{kj}^i - \tilde{\varepsilon}_{kj}^i\right)^2 + \lambda\|\nabla m^i\|^2 \\ \text{subject to} \quad & \delta\Pi(\mathbf{u}, p) = 0. \end{aligned} \quad (3.2)$$

Here V and ε_{kj} are the measured volume and regional Lagrangian strain in segment j in direction k respectively, and $\tilde{V}^i = -\frac{1}{3}\int_{\partial\Omega_{\text{endo}}}(\mathbf{X}+\mathbf{u})\cdot J\mathbf{F}^{-T}\mathbf{N}\mathrm{d}S$, and $\varepsilon_{kj} = \frac{1}{|\Omega_j|}\int_{\Omega_j}\mathbf{e}_k^T\nabla\mathbf{u}\,\mathbf{e}_k\mathrm{d}x$. The parameters α and λ control the weights on the different terms, and the sum in the second term is taken over the seventeen AHA segments, and the three different strain components (Section 3.2.1).

The data assimilation procedure is divided into two phases; a passive and an active phase. For the passive phase we iteratively estimate the unloaded configuration and the linear isotropic parameter, a in (3.1), using an algorithm similar to the one described in [16], and we set $\alpha = 1.0$, with $\lambda = 0$ and $\gamma = 0$, minimizing only the misfit with the measured volumes. The remaining material parameters are fixed according to [Table 1 row 3 of [10]]. For the active phase we fix the material parameter optimized in the passive phase, choose the control variable m to be γ or T_a for the active strain and active stress model respectively, and set $\alpha = 0.95$ and $\lambda = 0.01$. This choice of α and λ was based on the analysis done in [2]. A summary of our optimization pipeline is provided to the right in Figure 3.1.

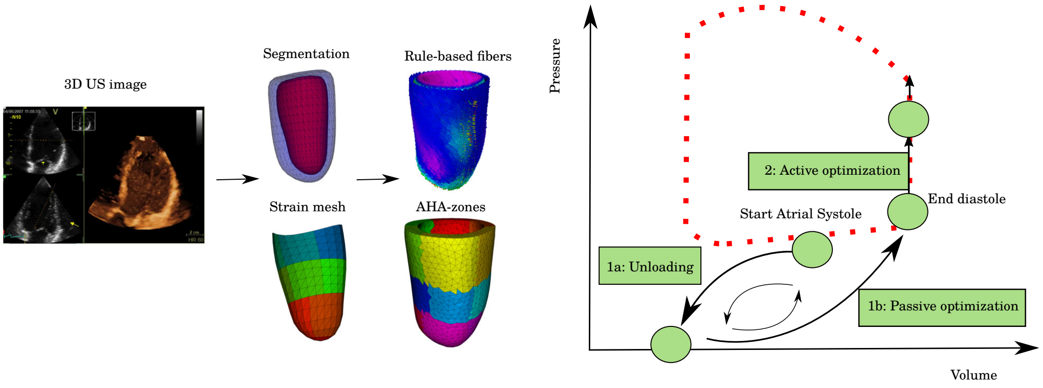

Figure 3.1: Left: Automated anatomical modeling pipeline to produce AHA marked simulation meshes with applied fiber orientations from 3D echocardiographic segmentations. Right: Optimization pipeline. 1. Unloaded geometry and the linear isotropic material parameter a in (3.1) are estimated iteratively. The unloaded geometry is estimated based on the backward displacement method (1a) [16] and a is estimated by minimizing the difference between simulated and measured volumes (1b). 2. The unloaded geometry and the material properties are fixed, and the amount of contraction (γ for active strain and T_a for active stress) is estimated by minimizing the mismatch between simulated and measured strain and volume. The active optimization continues to the next measurement point until all measurement points in the cycle are covered.

Implementation details

We employ a Galerkin finite element method with Taylor-Hood tetrahedral elements, that is $(\mathbf{u}, p) \in \mathbb{P}_2 \times \mathbb{P}_1$, with $\mathbb{P}_n$ being the space of piecewise polynomials of degree n. The solver is implemented in the finite element framework FEniCS [15], and uses a Newton trust region algorithm [3] to solve nonlinear systems. The minimization of the model-data misfit functional (3.2) is accomplished by a sequential quadratic programming algorithm (SQP) [14], where the functional gradient is computed by solving an automatically derived adjoint equation [7]. In these minimizations an upper bound of 0.5 and 500 kPa is set for the active strain (γ) and active stress (T_a) control variable respectively, which both are modeled as functions in $\mathbb{P}_1$, yielding one parameter per nodal point in the mesh.

Contraction analysis

Although direct physical interpretation of the active strain parameter γ is difficult, it may be seen as the relative shortening of an isolated and unloaded muscle cell. A high value of γ is therefore an indication of higher contractile force in the myocardium, independent of load. We propose that the spatially averaged γ over the entire LV, denoted by $\overline{\gamma}$, can be used as an index of global contractility. Similarly, the active stress parameter T_a is related to force development at level of the sarcomeres[8], and the spatially averaged T_a, denoted $\overline{T_a}$ can be used as an index of contractility. In addition to the contractility information contained in $\overline{\gamma}$ and $\overline{T_a}$, the overall elastic state of the optimized patient models can be used to give estimates of LV elastance. The left ventricular end-systolic elastance E_{ES}, the response of end systolic volume to increased load, is considered to be one of the major determinants for cardiac systolic function, and was in [18] proposed as a global index of ventricular contractility. It is possible to estimate the end systolic elastance directly if the end systolic pressure is known or estimated, by perturbing the loading conditions on the optimized model at end systole while fixing the remaining quatities, and calculating the slope in the resulting ES pressure-volume curve. More precisely, if $p_{\text{lv}}^{\text{ES}}$ is the end-systolic ventricular pressure, with cavity volume V^{ES}, we change the pressure to $p_{\text{lv}}^{\text{ES+}\Delta} = p_{\text{lv}}^{\text{ES}} + \Delta p_{\text{lv}}$, resulting in a change in volume, $V^{\text{ES+}\Delta} = V^{\text{ES}} + \Delta V$. The estimate of end-systolic elastance can then be calculated by

$$\tilde{E}_{\text{ES}} = \frac{\Delta p_{\text{lv}}}{\Delta V}. \tag{3.3}$$

Results and discussion

Matching of strain and volume

We show the results from two representative simulations in Figure 3.2, one from the LBBB group and one from the healthy control group. Snapshots from the calculated unloaded and end-systolic configurations are depicted. For the unloaded geometry, we also show the image-based geometry at beginning of atrial systole, and for the end-systolic configuration we show the longitudinal strain using both the active stress and active strain approach. We also show the agreement with the corresponding PV-loops.

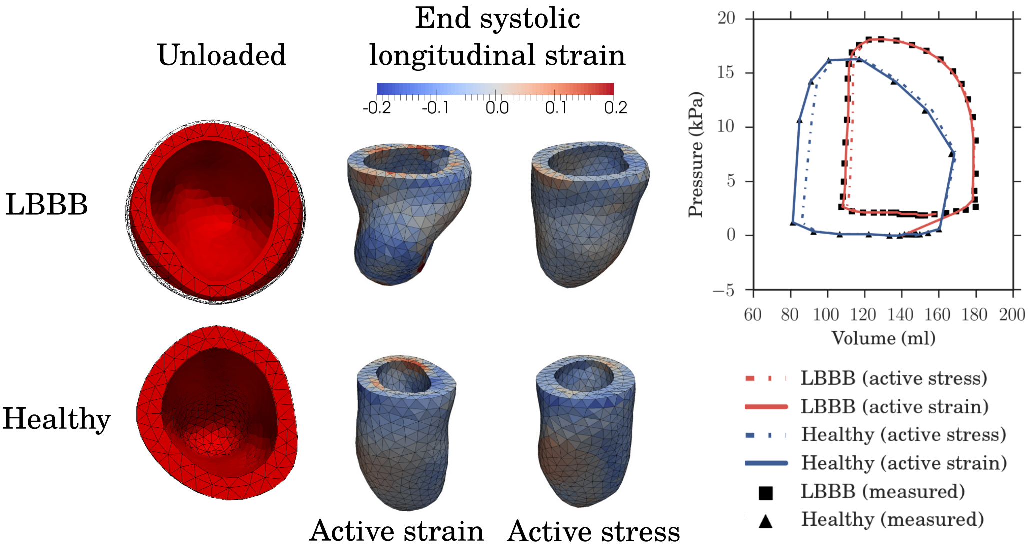

Figure 3.2: Left: Snap shots of the unloaded geometry in red, and the corresponding image based geometry taken at beginning of atrial systole in black wire-frame. Middle: Snap shot of end systolic configurations using the active strain and active stress approach. Color-map shows the end-systolic longitudinal strain. Right: Simulated and measured pressure-volume loops for these hearts using the active strain and active stress approach.

The total analysis of the 14 patients involved optimizing 432 volume measurements and 20 853 strain measurements. The average time for one forward and gradient evaluation was 8.3 and 8.9 seconds respectively when running on a cluster using four cores, with an average number of control parameters being 985.

In order to visualize the overall match of simulated to measured data, we show linear regression plots in Figure 3.3. These results are all based on the active strain formulation. For the strain, we separately consider the diastolic and systolic points, as different types of data were used to constrain the model in these two phases, namely volume in the diastolic phase and strain in the systolic phase. An excellent overall fit was obtained for the optimized volume ($R^2 = 1.00$) and systolic strains ($R^2 = 0.95$). Diastolic strains, not used in the optimization, were less well matched ($R^2 = 0.31$).

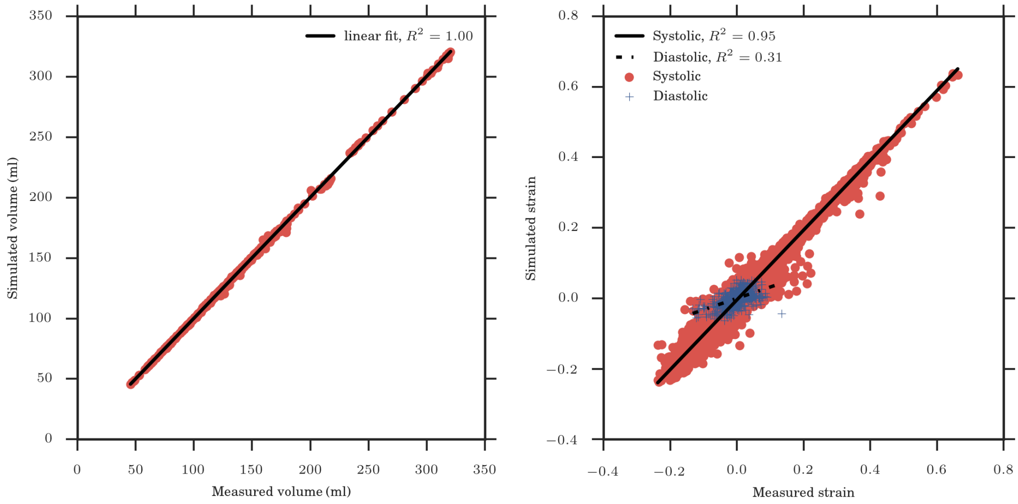

Figure 3.3: Scatter plot of simulated (y-axis) and measured (x-axis) strain and volume using the active strain approach. Left: Scatter plot of simulated versus measured volumes and the best linear least-squares fit of these points, (slope = 1.00). Right: Scatter plot of simulated versus measured strain for all segments and all directions, separated into the diastole, were only the volume was optimized and systole, where both the strain and volume were optimized. For diastole, the slope of the best linear fit was 0.31, while the best linear fit for the systolic points had a slope of 0.95.

Estimation of global contractility and elastance

Global contraction time courses, $\overline{\gamma}$ and $\overline{T}_a$, for each patient were synchronized to the valvular events to normalize for differing cycle lengths. The average and standard deviation of these normalized traces for the LBBB vs the healthy controls are shown in left of Figure 3.4. The healthy patients had a much higher level of contraction through the cardiac cycle, and the peak values were compared using one-way ANOVA, yielding a $P-$value less than 0.001 for both the active strain and the active stress approach.

The values of calculated $\tilde{E}_{\text{ES}}$ for the healthy and LBBB patients are shown to the right in Figure 3.4. The calculated elastances of the LBBB group were significantly lower than for the healthy group, with the comparison between the groups using one-way ANOVA giving a $P-$value of 0.009 and 0.003 for the active strain and active stress respectively.

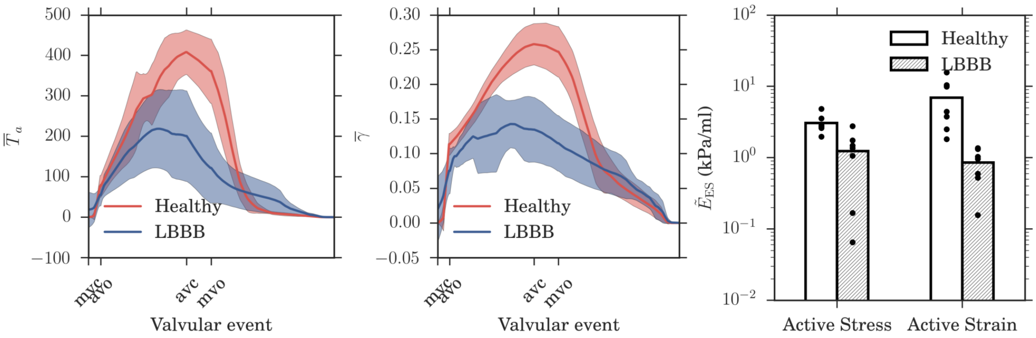

Figure 3.4: Extracted biomarkers related to cardiac contractility. Left: Mean value of T_a for the two groups synchronized with respect to valvular events (mvc: mitral valve closure, avo: aortic valve opening, avc: aortic valve closure, mvo: mitral valve opening). Shaded region shows ± one standard deviation. Middle: Mean value of γ for the two groups synchronized with respect to the same valvular events. Right: Estimated values of $\tilde{E}_{\text{ES}}$, given by (3.3) using the active stress and the active strain approach. The mean value is depicted for each group as a bar, and individual points are also displayed.

Discussion

In this study we applied an adjoint-based data assimilation technique to constrain patient data to a cardiac mechanics model. LV pressure was used as a boundary condition, and an unloading algorithm was used to find a reference geometry and a material parameter based on diastolic P-V measurements. Active contraction was then captured by assimilation of measured systolic LV regional strains by the means of a spatially varying contraction parameter. We tested this methodology on a group of seven healthy control patients and seven patients diagnosed with LBBB. The results gave an excellent fit between the measured and simulated volume and systolic strain ($R^2 \geq 1.00$ and $R^2 \geq 0.95$, respectively) for more than 21,000 observation points. Meanwhile diastolic strains, due to the quality of the strain measurements during late diastole, were not included in the optimization and had a resulting poor fit. However, allowing for spatial heterogeneity in the material parameters and/or optimizing more parameters from the material model, could allow for better fit values also in this part of the cycle and will be further investigated. Of course, questions regarding uniqueness of such solutions in general will need to be carefully addressed in future studies.

Our simulations show that estimating the unloaded configuration may be important to capture the correct material parameters, as we optimized to a consistently softer material when the unloading algorithm was used. Meanwhile, this seemed to have less of an impact in systole, as the the overall estimated ventricular elastance was unchanged.

These calibrated models allow for estimating aspects of cardiac contractility, such as the traditional measure of end-systolic elastance, by perturbations of the model at the end systolic configuration. The healthy control group had significantly higher estimated end-systolic elastance than the LBBB group, although limitations exist with these calculations due to using a synthetic pressure curve with the healthy group. However, the values calculated by using direct pressure readings for the LBBB group (3 - 10 mmHg) are slightly higher but correspond very well with the range provided for a heart failure cohort of (0.5 - 4.9 mm Hg) [19]. Clinically, end systolic elastance is measured based on data obtained using multiple beats subjected to different loading conditions. This change in loading conditions also gives rise to changes in the active tension as a function of myocardial strain, an effect that is not modelled directly here. Therefore, although we can calculate a discriminating marker of stiffness between the two cohorts, future work evaluating this method over a number of beats with different loading conditions is needed to assess its relation to clinical end-systolic elastance.

In addition to the end-systolic elastance estimates, our simulations also were used to compare the average value of γ and T_a, which may also be interpreted as indices of contractility, between the two groups through the cardiac cycle. Again, the healthy controls showed a significantly higher peak values of active strain and stress, compared to the LBBB group and both analysis methods showed comparable trends.

Conclusions

Adjoint-based data assimilation is a powerful technique for estimating high dimensional parameters in order to incorporate large amounts of information into a model. Although limitations in our patient data and assumptions remain, we have demonstrated how such techniques can be applied to problems in mechanics for use in extracting potential biomarkers related to cardiac contractility. Future work will be used to adjust and improve such models and work towards their validation and clinical utility.

Acknowledgments

This study was funded by Research Council of Norway: Center for Biomedical Computing at Simula Research Laboratory and Center for Cardiological Innovation at Oslo University Hospital. Computations were performed on the Abel supercomputing cluster at the University of Oslo via a Notur project.

Bibliography

[1] D Ambrosi and S Pezzuto. Active stress vs. active strain in mechanobiology: constitutive issues. *Journal of Elasticity*, 107(2):199–212, 2012.

[2] Gabriel Balaban, Henrik Finsberg, Hans Henrik Odland, Marie Rognes, Stian Ross, Joakim Sundnes, and Samuel Wall. High resolution data assimilation of cardiac mechanics applied to a dyssynchronous ventricle. *International Journal for Numerical Methods in Biomedical Engineering*, 2017.

[3] S Balay, J Brown, K Buschelman, WD Gropp, D Kaushik, MG Knepley, L Curfman McInnes, BF Smith, and H Zhang. PETSc web page. http://www.mcs.anl.gov/petsc, 2015.

[4] JD Bayer, RC Blake, G Plank, and NA Trayanova. A novel rule-based algorithm for assigning myocardial fiber orientation to computational heart models. *Annals of biomedical engineering*, 40(10):2243–2254, 2012.

[5] Manuel D Cerqueira, Neil J Weissman, Vasken Dilsizian, Alice K Jacobs, Sanjiv Kaul, Warren K Laskey, Dudley J Pennell, John A Rumberger, Thomas Ryan, Mario S Verani, et al. Standardized myocardial segmentation and nomenclature for tomographic imaging of the heart a statement for healthcare professionals from the cardiac imaging committee of the council on clinical cardiology of the american heart association. *Circulation*, 105(4):539–542, 2002.

[6] Radomir Chabiniok, Philippe Moireau, P-F Lesault, Alain Rahmouni, J-F Deux, and Dominique Chapelle. Estimation of tissue contractility from cardiac cine-MRI using a biomechanical heart model. *Biomechanics and modeling in mechanobiology*, 11(5):609–630, 2012.

[7] Patrick E Farrell, David A Ham, Simon W Funke, and Marie E Rognes. Automated derivation of the adjoint of high-level transient finite element programs. *SIAM Journal on Scientific Computing*, 35(4):C369–C393, 2013.

[8] Serdar Göktepe, Andreas Menzel, and Ellen Kuhl. The generalized hill model: A kinematic approach towards active muscle contraction. *Journal of the Mechanics and Physics of Solids*, 72:20–39, 2014.

[9] Gerhard A Holzapfel. *Nonlinear solid mechanics*, volume 24. Wiley Chichester, 2000.

[10] Gerhard A Holzapfel and Ray W Ogden. Constitutive modelling of passive myocardium: a structurally based framework for material characterization. *Philosophical Transactions of the Royal Society of London A: Mathematical, Physical and Engineering Sciences*, 367(1902):3445–3475, 2009.

[11] Oslo University Hospital. Acute feedback on left ventricular lead implantation location for cardiac resynchronization therapy (CCI impact). https://clinicaltrials.gov, 2016.

[12] Peter Hunter, Peter V Coveney, Bernard de Bono, Vanessa Diaz, John Fenner, Alejandro F Frangi, Peter Harris, Rod Hose, Peter Kohl, Pat Lawford, et al. A vision and strategy for the virtual physiological human in 2010 and beyond. *Philosophical Transactions of the Royal Society of London A: Mathematical, Physical and Engineering Sciences*, 368(1920):2595–2614, 2010.

[13] Mary E Klingensmith et al. *The Washington manual of surgery*. Lippincott Williams & Wilkins, 2008.

[14] Dieter Kraft et al. *A software package for sequential quadratic programming*. DFVLR Obersfaffeuhofen, Germany, 1988.

[15] Anders Logg, Kent-Andre Mardal, and Garth Wells. *Automated solution of differential equations by the finite element method: The FEniCS book*, volume 84. Springer Science & Business Media, 2012.

[16] Amir Nikou, Shauna M Dorsey, Jeremy R McGarvey, Joseph H Gorman III, Jason A Burdick, James J Pilla, Robert C Gorman, and Jonathan F Wenk. Effects of using the unloaded configuration in predicting the in vivo diastolic properties of the heart. *Computer methods in biomechanics and biomedical engineering*, 19(16):1714–1720, 2016.

[17] Stein Inge Rabben. Technical principles of transthoracic three-dimensional echocardiography. In *Textbook of Real-Time Three Dimensional Echocardiography*, pages 9–24. Springer, 2010.

[18] Kiichi Sagawa, Hiroyuki Suga, Artin A Shoukas, and Kenneth M Bakalar. End-systolic pressure/volume ratio: a new index of ventricular contractility. *The American journal of cardiology*, 40(5):748–753, 1977.

[19] Hideaki Senzaki, Chen-Huan Chen, and David A Kass. Single-beat estimation of end-systolic pressure-volume relation in humans a new method with the potential for noninvasive application. *Circulation*, 94(10):2497–2506, 1996.

[20] Marco Viceconti and Peter Hunter. The virtual physiological human: Ten years after. *Annual Review of Biomedical Engineering*, 18(1), 2016.

Paper 3

Efficient estimation of personalized biventricular mechanical function employing gradient-based optimization

Paper 4

Assessment of regional myocardial work from a patient-specific cardiac mechanics model